CONTROLLABLE VAPOR MICROBUBBLES FOR USE IN BIOPARTICLE ACTUATION

by

Rebecca Braff Maxwell

B.S. Cornell University (1996)
D.I.C. Imperial College London (1997)
S.M. Massachusetts Institute of Technology (1999)

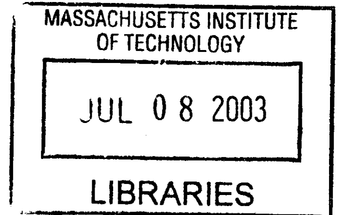
MASSACHUSETTS INSTITUTE OF TECHNOLOGY

JUL 08 2003

LIBRARIES

Submitted to the Department of Mechanical Engineering
in partial fulfillment of the requirements for the degree of

DOCTOR OF PHILOSOPHY IN MECHANICAL ENGINEERING
at the
MASSACHUSETTS INSTITUTE OF TECHNOLOGY
June 2003

BARKER

© Massachusetts Institute of Technology 2003. All rights reserved.

Author...
Department of Mechanical Engineering
April 28, 2003

Certified by...
Martin A. Schmidt
Professor of Electrical Engineering
Thesis Supervisor

Certified by...
Mehmet Toner
Professor of Biomedical Engineering, Mass. Gen. Hospital and Harvard Medical School
Thesis Supervisor

Certified by...
Martha Gray
Edward Hood Taplan Professor of Electrical Engineering
Thesis Supervisor

Certified by ....
Bora Mikic
Professor of Mechanical Engineering
Chairman of Thesis Committee

Accepted by...
Ain Sonin
Chairman, Committee on Graduate Students

CONTROLLABLE VAPOR MICROBUBBLES FOR USE IN BIOPARTICLE ACTUATION

by

Rebecca Braff Maxwell

Submitted to the Department of Mechanical Engineering
on April 28, 2003, in partial fulfillment of the
requirements for the degree of
Doctor of Philosophy in Mechanical Engineering

ABSTRACT

In this thesis, we present guidelines for using thermally formed microbubbles as a means of fluidic actuation. The use of microbubbles is attractive due to the simple fabrication and operation of such devices, however, prior work in this area was hindered by several issues inherent to vapor bubble formation that severely limited the reliability of bubble-based devices. It has been shown in this thesis that it is possible to control the location at which bubbles form and the size of the bubbles, as well as to achieve repeatable and reduced bubble formation temperature, and to create bubbles that collapse completely in less than 10 seconds.

The achievement of controllable microbubbles makes possible many microfluidic applications, one of which we will demonstrate in this work. We have built a device that is capable of capturing, holding, and selectively releasing single bioparticles using microbubble actuation. This bioparticle actuator could be scaled into an array for the analysis of a large population of individual cells.

Thesis Supervisor: Martin A. Schmidt
Title: Professor of Electrical Engineering

Thesis Supervisor: Mehmet Toner
Title: Professor of Biomedical Engineering, Massachusetts General Hospital and Harvard Medical School

Thesis Supervisor: Martha Gray
Title: Edward Hood Taplan Professor of Electrical Engineering

Chairman of Committee: Bora Mikic
Title: Professor of Mechanical Engineering

ACKNOWLEDGEMENTS

This work was sponsored in part by the National Science Foundation, and the Alliance for Cellular Signaling. I would like to thank my advisors, Marty Schmidt, Martha Gray, and Mehmet Toner for all of their support and guidance throughout this thesis. Working on this project has been a wonderful experience, and I thank them for giving me this exciting opportunity. Each of them brought different perspectives and areas of expertise to the group and it was truly a privilege to work with them. I'd also like to thank Bora Mikic for being the chair of the committee and giving me so much advice throughout the project. He always made time to meet with me when I needed help, and was a pleasure to work with.

Thanks to everyone in the Schmidt group- present and past. I'd particularly like to thank Xue'en Yang for all of her advice and assistance with my thermal modeling and MATLAB, and Antimony Gerhardt for doing some of the testing when she was a UROP student and carrying on with the work now that she is a grad student. Christine Tsau and Ole Neilson also helped with all kinds of things in the lab, and out. I would not have been able to get my Labview test setup working so quickly without all the help I received from Lodewyk Steyn, and I'm very grateful for all of his electronic expertise. I'd also like to thank Samara Firebaugh and Joel Voldman for their guidance while they were still students, when I was beginning this project. I'm also grateful to Anne Wasserman and Pat Varley for all of their administrative assistance during my time at MIT- they certainly helped make life a lot easier. I'd also like to thank Debb Hodges-Pabon for having such a great personality and adding so much life to the MTL.

Thanks also goes to the staff of the Microsystems Technology Laboratory. I received so much help in the lab from Dennis Ward, Kurt Broderick, Joe Walsh, Bob Bicchieri, Bernard Alamariu, Dan Adams, Vicky Diadiuk, and Gwen Donahue. I'd also like to thank Arturo Ayon and Tom Takacs for their help with STS etching. I would like to thank the people at Surface Technology Systems who did the quartz etching on my final test samples.

I'd especially like to thank my friends and family for all of their love and support outside of the lab. Afternoon tea with Laura, and evenings of eating chocolates and hanging out with Amy helped me make it through without losing my mind entirely. My parents and brother have given me love and encouragement from the beginning, and I want to thank them for everything that they have done for me.

I must also acknowledge my puppy, Schafer, who made great contributions to the writing of this thesis. She is certainly a canine genius.

Lastly, I would like to thank Brian for being wonderful and believing in me through it all, even when I was nearly impossible to live with. I couldn't have done this without you.

TABLE OF CONTENTS

1. INTRODUCTION **13**

1.1 BACKGROUND AND SIGNIFICANCE 13

1.1.1 The Microfabrication-Based Dynamic Array Cytometer *14*

1.1.2 Microfluidic Actuation *15*

1.1.3 Cell Manipulation MEMS Devices *18*

1.2 OBJECTIVES 21

1.3 OVERVIEW OF DEVICE FOR MICROBUBBLE ACTUATION 21

1.4 THESIS ORGANIZATION 22

2 THEORY AND MODELING **24**

2.1 BUBBLE NUCLEATION 24

2.1.1 Homogeneous Nucleation *24*

2.1.2 Heterogeneous Nucleation *26*

2.2 THERMAL MODELING 27

2.2.1 Finite Element Model *28*

2.2.2 Analytical Model *30*

2.2.3 Finite Difference Models *34*

2.3 BUBBLE COLLAPSE 41

2.3.1 Phase Change Collapse *41*

2.3.2 Diffusion Collapse *43*

3 DESIGN **46**

3.1 RESISTIVE HEATERS 46

3.2 BIOPARTICLE ACTUATOR 50

3.3 FLOW SYSTEM 52

4 FABRICATION **54**

4.1 QUARTZ PROCESS 54

4.2 SILICON PROCESS 57

4.3 DEVICE ASSEMBLY 58

5 EXPERIMENTAL METHODS **60**

5.1 SAMPLE PREPARATION FOR RESISTOR TESTING 60

5.1.1 Calibration *60*

5.1.2 Water Preparation *62*

5.2 FIRST GENERATION TESTING 62

5.3 SECOND GENERATION TESTING METHOD 65

5.3.1 Test Apparatus *65*

5.3.2 Repeatability of Resistor Heating *67*

5.3.3 Bubble Formation Temperature *67*

5.3.4 Energy Dependence of Bubble Size *69*

5.3.5 Bubble Dynamics *70*

5.3.6 Cycling *71*

5.4 FULL DEVICE TESTING 71

6 RESULTS **72**

6.1 GENERAL EFFECT OF CAVITIES ON BUBBLE FORMATION (USING THE FIRST GENERATION TESTING METHOD) 72
6.2 SECOND GENERATION RESISTOR TESTING 75
6.2.1 Repeatability of Resistor Heating 75
6.2.2 Bubble Formation Location 76
6.2.3 Bubble Formation Temperature 77
6.2.4 Bubble Collapse Time 79
6.2.5 Energy Dependence of Bubble Size 80
6.2.6 Bubble Dynamics 82
6.2.7 Cycling 90
6.3 COMPARISON OF FIRST GENERATION AND SECOND GENERATION RESULTS 93
6.4 COMPLETE DEVICE 96

7 DISCUSSION AND CONCLUSIONS 98

7.1 OVERVIEW 98
7.2 DISCUSSION OF FIRST GENERATION RESULTS 98
7.3 DISCUSSION OF SECOND GENERATION RESULTS 99
7.3.1 Bubble Formation Location 99
7.3.2 Bubble Formation Temperature 102
7.3.3 Bubble Dynamics 104
7.3.4 Dependence of Bubble Diameter on Energy 105
7.3.5 Bubble Collapse 106
7.3.6 Cycling 107
7.4 FUTURE WORK 108
7.4.1 Controllable Bubble Formation 108
7.4.2 Microbubble Bioparticle Actuator 109
7.5 CONCLUDING REMARKS 110

8 APPENDIX 111

8.1 APPENDIX A: QUARTZ PROCESS 111
8.2 APPENDIX B: SILICON PROCESS 113
8.3 APPENDIX C: DEVICE ASSEMBLY PROCESS 116
8.4 APPENDIX D: MATLAB CODE FOR FINITE DIFFERENCE MODEL- LINE HEATER 117
8.5 APPENDIX E: MATLAB CODE FOR FINITE DIFFERENCE MODEL- FOLDED HEATER 121

9 BIBLIOGRAPHY 129

FIGURES

Figure 1-1 μDAC system diagram (courtesy of Joel Voldman) 15
Figure 1-2 Illustration of the Hitachi cell capture plate 20
Figure 1-3 Schematic of the operation of the device is shown. 22
Figure 2-1 Thermodynamic pressure-volume diagram[60]. 25
Figure 2-2 Schematic of finite element model. 28
Figure 2-3 Results of finite element simulation of resistive line heater 29
Figure 2-4 Schematic and boundary conditions for thermal model of resistor. 30
Figure 2-5 Thermal circuit model of heater, water, and quartz system. 31
Figure 2-6 Plot of average heater temperature as a function of time. 34
Figure 2-7 Comparison of steady state temperature of heater 34
Figure 2-8 Two resistor geometries modeled. 35
Figure 2-9 Sample control volume for finite difference model. 36
Figure 2-10 Meshed finite difference model of line heater. 37
Figure 2-11 Finite difference model temperature distribution results. 38
Figure 2-12 Schematic and boundary conditions for folded resistor model. 39
Figure 2-13 Results of finite difference simulation for the folded resistor. 40
Figure 3-1 Resistive heater with cavity etched into substrate. r_c is the cavity radius. 47
Figure 3-2 Illustration of the effect of hydrophobic surface treatments. 47
Figure 3-3 Illustration of surface treatments for the resistive heaters. 48
Figure 3-4 Resistive heater geometries. 48
Figure 3-5 On the left is a folded resistor 49
Figure 3-6 Schematic of components and dimensions of the microbubble cell actuator. 50
Figure 3-7 Operation of the microbubble cell actuator. 51
Figure 3-8 Schematic of flow chamber. 52
Figure 3-9 Dimensions of flow chamber. 53
Figure 4-1 Fabrication process for quartz heater layer. 55
Figure 4-2 SEMs of 10μm wide trenches on quartz wafers etched by STS. 56
Figure 4-3 Micrograph of completed resistive heater with cavity. 56
Figure 4-4 Silicon bioparticle manipulation layer fabrication process. 57
Figure 4-5 SEM of capture well and bubble jet channel on silicon layer. 58
Figure 5-1 Apparatus used to calibrate resistors. 60
Figure 5-2 Plot of temperature versus normalized resistance used to calibrate resistors. 62
Figure 5-3 A typical I-V curve generating in the testing of a line heater 63
Figure 5-4 The heater temperature curve generated using the I-V curve 64
Figure 5-5 Schematic of test apparatus for second generation testing. 66
Figure 5-6 The three resistor configurations tested. 67
Figure 5-7 Heating curve for a folded resistor tested using the LABVIEW program. 69
Figure 6-1 A CYTOP-coated platinum line heater with a cavity. 72
Figure 6-2 Resistor temperatures at bubble formation 73
Figure 6-3 Repeatability of resistor temperature at bubble formation. 74
Figure 6-4 Bubble collapse time as a function of maximum bubble size 75
Figure 6-5 Plot of average heater temperature versus time for a 4 volt, 50ms pulse. 76
Figure 6-6 Folded heater with etched cavity. 77
Figure 6-7 Apparent bubble formation temperatures for silanized folded resistors. 78
Figure 6-8 Apparent bubble formation temperatures for silanized folded resistors. 79

Figure 6-9 Plot of bubble collapse time versus initial bubble diameter 80
Figure 6-10 Plot of bubble diameter versus total energy applied to the heater................. 81
Figure 6-11 Plot of heater temperature versus time for a 40ms voltage pulse.................. 82
Figure 6-12 Plot of heater temperature versus time for an 80ms voltage pulse................ 83
Figure 6-13 Above is a plot of heater temperature versus time 84
Figure 6-14 Above is a plot of heater temperature versus time 85
Figure 6-15 Above is a plot of heater temperature versus time 86
Figure 6-16 Above is a plot of heater temperature versus time 87
Figure 6-17 Above is a plot of heater temperature versus time. 88
Figure 6-18 Captured video frames from the t=2000ms voltage pulse............................ 90
Figure 6-19 Plots of the heater temperature versus time 91
Figure 6-20 Plots of the heater temperature versus time 92
Figure 6-21 The plot on the left compares the apparent bubble formation....................... 94
Figure 6-22 The plot on the left compares the apparent bubble formation....................... 94
Figure 6-23 The plot on the left compares the apparent bubble formation 95
Figure 6-24 Plot of apparent bubble formation temperature corrected 96
Figure 6-25 Sequential photos of device operation during bead capture.......................... 97
Figure 7-1 Corrected apparent bubble formation temperature data 101

TABLES

Table 2-1 Thermodynamic superheat limit of water 26
Table 2-2 Heater temperature distribution results from finite difference model. 40
Table 3-1 Resistor geometries used in testing. 50
Table 5-1 Resistor characteristics for bubble formation temperature testing. 68
Table 5-2 Testing parameters for bubble diameter/collapse time testing 70
Table 5-3 Test parameters for bubble dynamics testing. 71
Table 6-1 Average apparent bubble formation temperature 77
Table 6-2 Results of bubble size/energy testing 81
Table 6-3 Apparent bubble formation temperature data 93
Table 7-1 Comparison of apparent bubble formation temperatures. 102

1. INTRODUCTION

Microfluidics is becoming increasingly important to the success of a wide variety of micromachined devices, particularly those with biological applications. With the reduced dimensions that are now easy to achieve, many researchers are attempting to build devices that can put a whole laboratory on a chip, manipulate cells, or deliver precise volumes of drugs. Even in the light of all the technological advances that have occurred over the past decade, many obstacles remain that hinder the production of a robust and simple microfluidic device. One area that is in need of improvement is microfluidic actuators, valves, and pumps.

There is a great deal of potential in using thermally formed microbubbles as a means of fluidic actuation, due to the simple fabrication and operation of such devices. Prior work in this area was hindered by several issues inherent to vapor bubble formation that severely limited the reliability of bubble-based devices. The work in this thesis demonstrates strategies to overcome those challenges such that bubbles form at a specified location, at repeatable temperatures. The bubble formation event can be detected automatically and the bubble can collapse completely in less than 10 seconds, making re-use possible.

The achievement of controllable microbubbles makes possible many microfluidic applications, one of which we will demonstrate in this work. We have built a device that is capable of capturing, holding, and selectively releasing single bioparticles using microbubble actuation. This bioparticle actuator could be scaled into an array for the analysis of a large population of individual cells.

1.1 Background and Significance

Microelectromechanical systems (MEMS) have great potential in the biomedical field [1]. Microscale devices can be used for clinical applications such as drug or blood testing, and also for basic biological research into cells and DNA sequencing. While MEMS devices can take advantage of small sample sizes and high throughput that are not possible on the macroscale, there are still significant obstacles that must be overcome to make MEMS devices feasible for most biomedical applications. One of the critical issues

for biological MEMS is the movement and control of fluids and particles in fluids on the microscale.

1.1.1 The Microfabrication-Based Dynamic Array Cytometer

This thesis work was completed to provide an enabling cell manipulation technology for a project whose long-term goal is to create a dynamic cell analysis system. As discussed above, the existing cell analysis technologies are capable of either high throughput sorting based on a single instantaneous measurement, or the observation of cells over time without subsequent sorting. A technology does not exist that is capable of monitoring fluorescent data from a large population of individual cells over time and then sorting the cells into an arbitrary number of fractions. We propose to build such a system using microfabrication.

The "µDAC" (microfabrication-based dynamic array cytometer) will combine the dynamic measurements of cells with fast sorting to make new cell analysis possible [2]. As shown in Figure 1-1, the system will consist of four parts: 1) a microfabricated chip (cell-array chip) that will capture and hold many cells (~10,000) in an array; 2) a fluidic system to introduce the cells and reagents to the chip, and to collect released cells 3) an optical system to fluorescently interrogate the cell array and record single-cell data; and 4) a control system to selectively release those cells that display a given behavior or signal pattern. With this device, the cell population may also be sorted into any number of fractions.

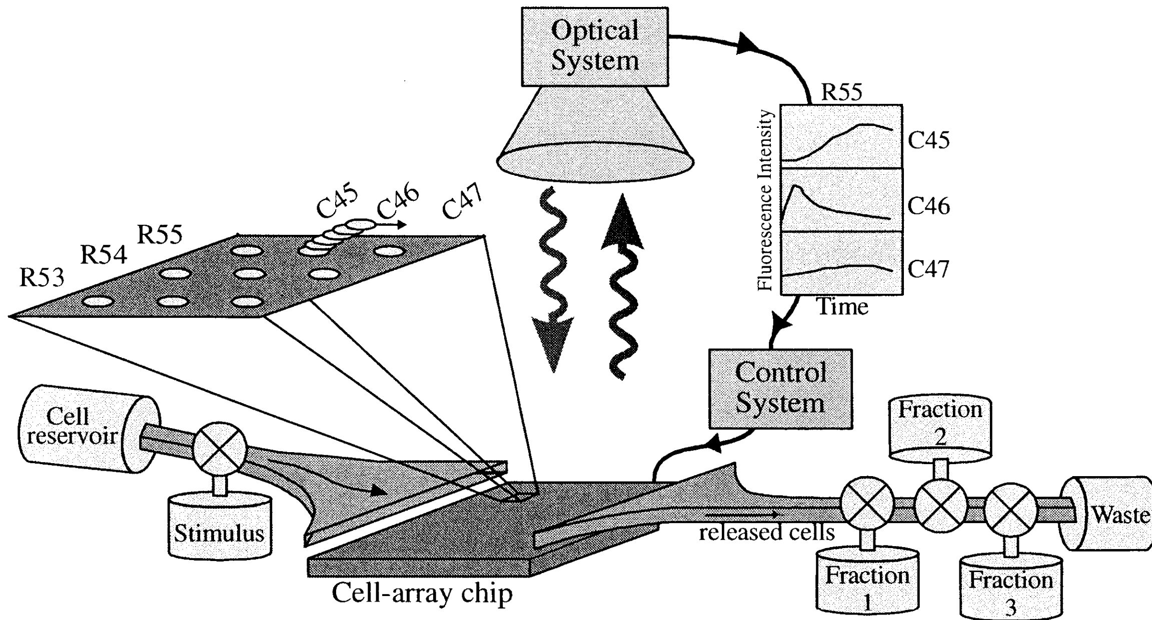

Figure 1-1 μDAC system diagram (courtesy of Joel Voldman)

The μDAC will make it possible to perform dynamic cell assays that were previously not feasible with existing technologies. Although much is known about cellular behavior from the currently available cell probes, the benefit of dynamic measurements could be enormous. Cells certainly differentiate themselves with their instantaneous responses to various stimuli, but they most likely differ further in their speed of reaction and recovery. This sort of data is not currently possible for large cell populations, and they cannot be sorted for further study based on their responses. The μDAC will open up the possibility of a vast quantity of new studies of cellular dynamics.

1.1.2 Microfluidic Actuation

There are several methods of microfluidic actuation that are currently in use [3-5]. Many actuation schemes involve the deflection of a silicon membrane in order to displace fluid. In thermopneumatic pumping [6, 7], gas in a sealed chamber bounded by a membrane is heated so that the thermal expansion of the gas deflects the membrane and pushes fluid. This method can generate a fairly large pressure, with a response time on the order of 100 milliseconds. Membranes can also be deflected electrostatically [8, 9] to move fluids. The response time is quite fast for this method (~0.1msec) but the pressure generated is fairly small and the geometric constraints are limiting. Membranes may

also be deflected to move fluids by using piezoelectric materials [10]. The fabrication of piezoelectrics onto membranes can be quite complicated and it is difficult to get a thick enough piezoelectric film to have sufficient membrane deflection. Another mode of actuation uses bimetalic structures and takes advantage of the thermal expansion mismatch between two different metals [11]. These devices have response times on the order of 100 milliseconds but generally have limited displacements (~10μm). Electromagnetic actuators work by moving a magnetic mass suspended by a spring beam with a magnetic field generated by an external solenoid coil [12, 13]. They are capable of large displacements (~1mm) and have a fast response time, but do not generate a lot of pressure and are complicated to fabricate.

Another novel approach to actuation which does not depend on the deflection of a membrane is the use of stimuli-responsive hydrogels [14]. These hydrogels expand or contract reversibly in response to an environmental change, such as a change in pH of a solution. Another non-membrane-driven approach had been demonstrated that uses acoustic waves to eject liquid from a well [15]. In this approach, a piezoelectric material is excited by a high frequency signal, and the resulting acoustic wave causes a drop of fluid to be ejected. Electrolyte solutions may be moved through the application of electric fields to generate electro-osmotic flow [16]. Additionally, electrochemical reactions can be used to displace a membrane through the electrolysis of an aqueous electrolyte solution [17]. While all of these techniques have advantages, many of them suffer from complicated fabrication processes, and scaling difficulties due to elaborate electronics.

An alternative actuation strategy that has potentially good scaling properties is the use of thermally formed microbubbles. Microbubble powered devices have the advantage that they can run using relatively uncomplicated electronics, resulting in simple yet robust systems. Their simplicity contrasts sharply with many of the electromechanical devices described above. Microbubble powered device fundamentals depend on microscale mechanisms, as opposed to the many microsystems that are miniature versions of macroscale devices.

Several microfabricated devices have been proposed that employ microbubbles as actuators (or droplet ejectors), valves, and pumps [6, 18-26]. The earliest use of bubble

formation to create a jet of fluid was in the inkjet printer industry [27-30]. By using a thin-film heater to form a vapor bubble, thermal inkjet pens fire drops of ink out of chambers due to the volume expansion created by the bubble. The explosive vaporization used in the inkjet printing industry has already been proven as an effective, reliable fluid actuation mechanism. A similar approach has been used to eject precise volumes of a solution containing DNA onto a glass surface, thereby creating a DNA microarray for biological screening [31]. Recently, a microinjector was fabricated which uses two thermally formed vapor bubbles to eject a drop of fluid for inkjet printing applications [32, 33]. By using two bubbles that coalesce as they grow, additional fluid beyond the desired droplet is prevented from escaping the nozzle.

Evans and coworkers used vapor bubbles as valves and pumps in their micromixer [22] and in their 'bubble spring and channel valve' [23]. Microbubbles were used to stop flow through a chamber, acting as valves. Bubbles were also used as a means of volume expansion to push fluid through a channel. Bubbles are formed between a fixed and moveable wall, and as the bubble grows, the wall is displaced, opening the valve. To close the valve the bubble must be removed. Since the bubbles would not dissipate when the heater is turned off, an escape path was created for the bubble, drawing it away and closing the valve. However, the group reports that the valve may only be opened once because of difficulties removing the initial bubble from the confinement region. This group later used electrochemically-generated bubbles instead of vapor bubbles in a device [34], however, the residual bubbles remained an issue even with this technique. Their experience illustrates some of the problems with the use of microbubbles; namely that bubbles may not dissipate when the heat is turned off, and that devices are unable to properly manipulate the bubbles to place them in desired locations.

Residual gas bubbles were also a problem for another microfluidic pump using periodic vapor bubble generation in order to move fluid [18]. The vapor bubble is generated in a channel filled with a water solution. The shape of the channel is tapered so that the bubble is drawn outwards, pushing fluid as it moves. When the heater is turned off, the bubble collapses, but a residual gas bubble is left behind. The authors believe the residual bubble to be filled with dissolved gas from the water, or electrolytically

generated. In the course of operation of the device, several residual gas bubbles build up, decreasing the pumping efficiency.

Thermally formed bubbles have also been used as an agitation mechanism to improve microfluidic mixing [35]. By creating vapor bubbles in isopropyl alcohol, the bubbles act to both help pump the fluid and enhance mixing. A gas bubble filter was employed at the output of the device in order to remove any residual gas bubbles left in the fluid.

Vapor bubbles have also been used for optical switching [21]. Hewlett Packard used channels of fluid through which light could be transmitted. In order to deflect light transmission, thermal bubbles were formed in the channels to act as switches.

Vapor bubbles have also been used as a means of mechanical actuation. Lin and coworkers used microfabricated polysilicon resistive heaters to boil Fluorinert liquid and form a vapor bubble underneath a microfabricated paddle [24, 36]. The vapor microbubble was found to be stable and the size was controllable within a range of currents. In this way the paddle could be moved up and down depending on the current applied to the heater.

These examples illustrate the potential of bubble actuation, while there are still several remaining challenges to address. For microbubbles to be a useful tool for MEMS devices, it is necessary to be able to form bubbles in predetermined locations while minimizing the power necessary to do so, and to be able to do this in a controllable way. An equally important issue, with which many groups are struggling, is that when the heater used to form a bubble is turned off, the bubble must fully dissipate. Bubble collapse can be difficult to achieve because dissolved gas comes out of solution and creates a stable gas (not vapor) bubble. Residual bubbles can severely impede (or even prevent) proper performance of a microbubble-powered device.

1.1.3 Cell Manipulation MEMS Devices

There are primarily three methods available for the observation of biological cells. Using microscopy, a researcher is able to observe a small population of cells over time. Sorting the cells based upon their reactions, however, can be difficult and is not feasible for a large cell population. Flow cytometers, on the other hand, enable the measurement of fluorescent intensity for a large population of single cells, and are able to sort the

population based on the measurements [37, 38]. Unfortunately, only one instantaneous measurement can be made per cell. It is not possible to observe an individual cell over time. Laser-scanning cytometry utilizes cells positioned on a slide, so that the cell population can be scanned, and the individual cells can be observed over time [39]. Although dynamic measurements of individual cells are possible with this technique, subsequent sorting of the cell population based upon the measurements is not feasible.

Many MEMS devices have been produced in an effort to improve upon these existing cell manipulation and analysis technologies. In the areas of biology and medicine, micromachined devices have been made for use in drug-delivery, DNA analysis, diagnostics, and detection of cell properties [1, 40-42]. In the area of cell sorting, a microfabricated fluorescence-activated cell sorter has been produced [43]. This device uses electro-osmotic flow to sort single cells into one of two directions based upon a fluorescence measurement. The device has the same limitation of a flow cytometer in that it is unable to take more than a single instantaneous measurement of each cell. Another miniaturized flow cytometer was fabricated which uses external fluidic switching to sort cells based on their fluorescent response [44]. While this device has the same benefits and limitations of a flow cytometer, it is also significantly slower due to the off-chip fluidic switching. Another miniaturized flow cytometer has been made which uses an impedance measurement instead of fluorescence to analyze cells [45]. The impedance measurement makes it possible to differentiate cells based on their size, or to count the number of cells that flow past the detector. The device is good for cell population studies, but a sorting technique has not yet been implemented to go along with the detector.

The method developed in this thesis to capture, hold, and release cells using hydraulic forces draws upon previous work in cell manipulation. For example, in the early 1990's, Hitachi used pressure differentials to hold cells [46]. They microfabricated hydraulic capture chambers that were used to capture plant cells for use in cell fusion experiments. Pressure differentials were applied so that single cells were drawn down to plug an array of holes (Figure 1-2). Cells could not be individually released from the array, however, because the pressure differential was applied over the whole array, not to individual holes. A similar cell capture chip was fabricated using electroplated nickel for

use in a scanning optical cell measurement system [47]. In this device, single cells are trapped in individual apertures using a bulk pressure gradient. After taking measurements, the cells can all be released with a reverse pressure gradient, but cannot be individually sorted.

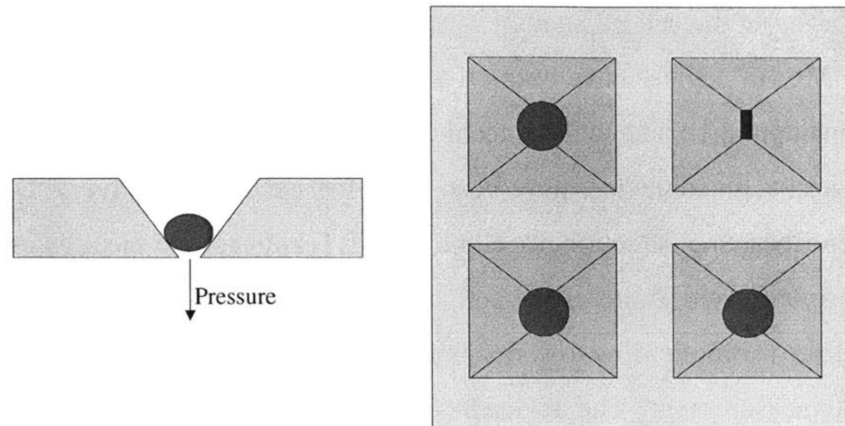

Figure 1-2 Illustration of the Hitachi cell capture plate

Arrays of wells etched into silicon have been used by Bousse et al. to passively capture cells by gravitational settling [48-51]. Multiple cells were allowed to settle into each of an array of wells where they were held against flow due to the hydrodynamics resulting from the geometry of the wells. Changes in the pH of the medium surrounding the cells were monitored by sensors in the bottom of the wells, but the wells lacked a cell-release mechanism, and multiple cells were trapped in each well. Another microfluidic device fabricated to monitor on-chip cellular behavior is comprised of a series of channels with sites to which cells can bind [52]. These cell-docking sites develop a layer of cells, which can be subsequently monitored as reagents are flown through the channels. While this device is able to monitor cell behavior over time, it lacks the capability to easily observe individual cells, and it is unable to sort the cells based upon their responses to the reagents.

Another method of cell capture is the use of dielectrophoresis (DEP). DEP refers to the action of neutral particles in non-uniform electric fields. Neutral polarizable particles experience a force in non-uniform electric fields that propels them toward the electric field maxima or minima, depending on whether the particle is more or less

polarizable than the medium it is in. By arranging the electrodes properly, an electric field may be produced to stably trap dielectric particles. Researchers have successfully trapped many different cell types using DEP, including mammalian cells, yeast cells, plant cells, and polymeric particles [53-58]. Dynamic cell assays, and subsequent sorting based on those results have been successfully achieved in a small-scale DEP electrode array by our research group [2]. More work must be completed, however, to determine whether the electric field imposes any harmful effects on cell function.

1.2 Objectives

In order to build the μDAC, it is first necessary to create a cell-array chip that is capable of capturing, holding, and selectively releasing cells. This thesis describes the use of microbubble actuation to accomplish this.

There are two primary areas of focus for this thesis. First, through experimentation, design, and modeling we plan to gain a better understanding of the bubble formation process on the microscale. Using this information we will find ways in which we can control bubble formation location and temperature, as well as bubble collapse. Specifically we will create heaters that are capable of having bubbles form in the same location every time, at a repeatable temperature, and without excessive superheat. Then through experimental protocol we will require that bubbles dissipate rapidly once the heat is no longer applied.

The second goal of this thesis is to use the controllable microbubble technology in a device that is capable of capturing, holding, and releasing a single bioparticle. The plans for this device will be discussed in the following section.

1.3 Overview of Device for Microbubble Actuation

Our goal is to create a device capable of capturing and releasing bioparticles in a controlled fashion, and more specifically to have the potential of scaling it up into a large-scale array. Figure 1-3 shows our design of the microbubble-powered bioparticle actuator.

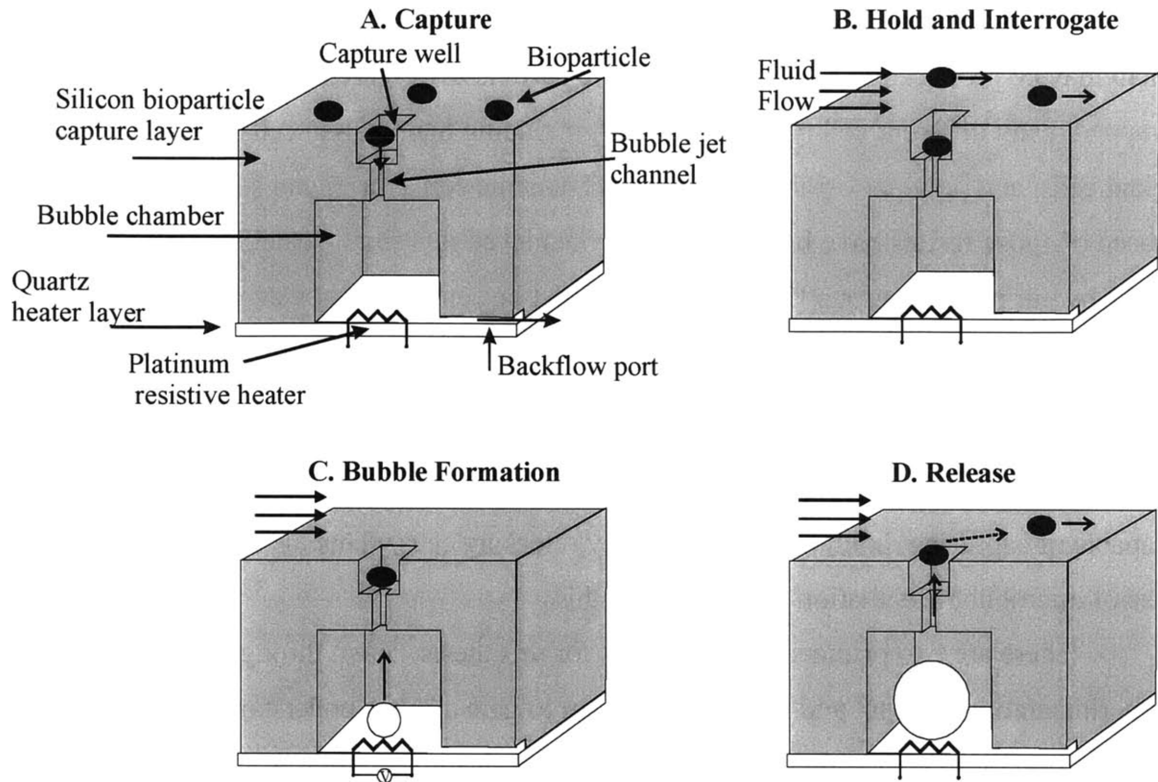

Figure 1-3 Schematic of the operation of the device is shown. When a back pressure is applied, a bioparticle may be drawn into a capture well (A). The capture well can be sized to accommodate only one particle. Then, when a bulk flow is applied over the top of the device, all the uncaptured particles are swept away (B). In order to release the particle, a voltage is applied to the resistive heater in the bubble chamber and a bubble forms (C). As a result, the volume expansion in the bubble chamber pushes out a jet of fluid that ejects the bioparticle from the capture well where it may be entrained in the flow and carried away (D).

When a back pressure is applied, a bioparticle may be drawn into a capture well. (A) The well can be sized to accommodate only one particle. Then, when a bulk flow is applied over the top of the device, all the uncaptured particles are swept away. (B) In order to release the particle, a voltage is applied to the heater in the chamber below and a bubble forms. (C) The volume expansion in the chamber pushes out a jet of fluid that ejects the bioparticle from the well where it may be entrained in the flow and carried out of the chamber. (D)

1.4 Thesis Organization

The organization of this thesis is as follows. Chapter 2 covers the theory behind bubble nucleation, and modeling used to predict the temperature distributions around the heater. Chapter 3 describes the design of the heaters, actuator, and flow system. In

Chapter 4 the fabrication processes to build the devices is described in detail. Chapter 5 covers the experimental protocols for both the heater testing and the testing of the bioparticle actuator, and the results are presented in Chapter 6. The discussion of the results and suggestions for future work are discussed in the final chapter of the thesis.

2 THEORY AND MODELING

This chapter will discuss the theory behind microbubble formation on a heater. First, the two regimes of bubble nucleation will be addressed, followed by a simplified heat transfer model. Numerical models will also be presented which help predict the temperature distribution in the field around the heater, as well as over the surface of the heater.

2.1 Bubble Nucleation

Pool boiling takes place when a heater surface is submerged in a pool of liquid. As the heater surface temperature increases and exceeds the saturation temperature of the liquid by an adequate amount, vapor bubbles nucleate on the heater. The layer of fluid directly next to the heater is superheated, and bubbles grow rapidly in this region until they become sufficiently large and depart upwards by a buoyancy force. While rising, the bubbles either collapse or continue growing depending on the temperature of the bulk fluid [59].

There are two modes of bubble nucleation: homogeneous and heterogeneous. Homogeneous nucleation occurs in a pure liquid, whereas heterogeneous nucleation occurs on a heated surface.

2.1.1 Homogeneous Nucleation

In a pure liquid containing no foreign objects, bubbles are nucleated by high-energy molecular groups. According to kinetic theory, pure liquids have local fluctuations in density, or vapor clusters. These are groups of highly energized molecules that have energies significantly higher than the average energy of molecules in the liquid. These molecules are called activated molecules and their excess energy is called the energy of activation. The nucleation process occurs by a stepwise collision process that is reversible, whereby molecules may increase or decrease their energy. When a cluster of activated molecules reaches a critical size, then bubble nucleation can occur [60].

In order to determine at what temperature water will begin to boil in the homogeneous nucleation regime, it is useful to know the thermodynamic superheat limit of water. Figure 2-1 shows the thermodynamic pressure-volume diagram.

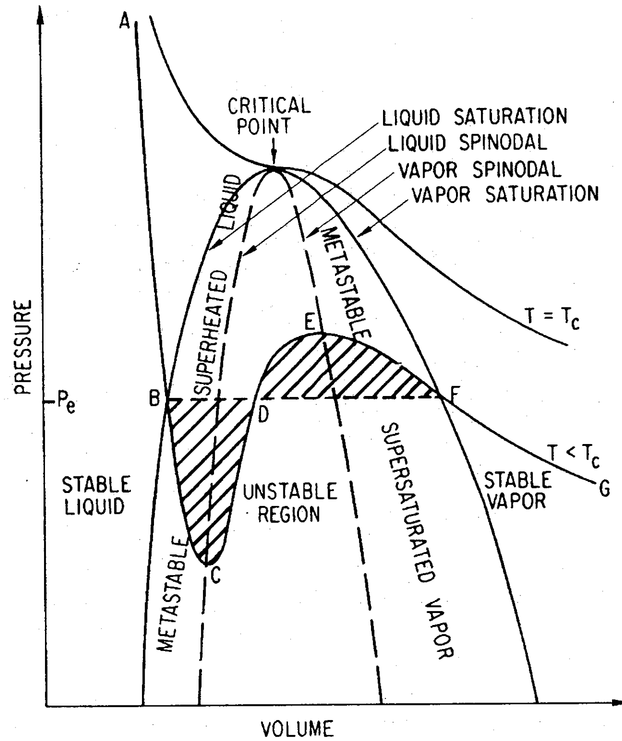

Figure 2-1 Thermodynamic pressure-volume diagram[60].

In this diagram, we can see a region of stable liquid to the far left, stable vapor to the far right, metastable regions, and an unstable region in the center of the dashed curve. The dashed line is called the spinodal, and to the left of the critical point represents the upper limit to the existence of a superheated liquid. Along this line, Equation (2-1) holds true, and within the spinodal, Equation (2-2) applies.

$$\left(\frac{\partial P}{\partial v}\right)_T = 0 \qquad (2\text{-}1)$$

$$\left(\frac{\partial P}{\partial v}\right)_T > 0 \qquad (2\text{-}2)$$

The van der Waals and Berthelot equations of state may be used to calculate the superheat limit of water, following the analysis in van Stralen and Cole [60].

$$\left(P+\frac{a}{T^n v^2}\right)(v-b)=RT \tag{2-3}$$

Where v is the specific volume, R is the gas constant, and a and b are constants. n=0 for the van der Waals equation, n=1 for the Berthelot equation, and n=0.5 for the modified Berthelot equation. a and b may be computed using Equation (2-3), given the fact that at the critical point, Equations (2-4) and (2-5) are true.

$$\left(\frac{\partial P}{\partial v}\right)_{T_{cr}}=0 \tag{2-4}$$

$$\left(\frac{\partial^2 P}{\partial v^2}\right)_{T_{cr}}=0 \tag{2-5}$$

Using the above equations, the thermodynamic superheat limit of water may be computed. The results are shown in Table 2-1.

Equation of State	**T/T_{cr} (T_{cr}=647°K)**	**Superheat Limit (°C)**
Van der Waals	0.844	273
Modified Berthelot	0.893	305
Berthelot	0.919	322

Table 2-1 Thermodynamic superheat limit of water calculated with 3 equations of state.

These values represent the temperature above which homogeneous nucleation must begin.

A kinetic limit of superheat may also be computed using the kinetic theory of the activated molecular clusters. The kinetic limit of superheat for water is about 300°C [60].

2.1.2 Heterogeneous Nucleation

When liquid is heated in the presence of a solid surface, heterogeneous nucleation usually occurs. In this regime, bubbles typically nucleate in cavities (surface defects) on

the heated surface. The degree of superheat necessary to nucleate a bubble in a cavity is inversely dependent on the cavity radius, as shown in Equation (2-6).

$$T_w - T_{sat} = \frac{2\sigma T_{sat}}{h_{lv}\rho_v r_c} \qquad (2\text{-}6)$$

Where T_w is the surface temperature, T_{sat} is the saturation temperature (100°C for water), σ is the surface tension, h_{fg} is the latent heat of vaporization, ρ_v is the vapor density, and r_c is the cavity radius. For example, the surface temperature necessary to nucleate bubbles in water with a surface that has a 1μm cavity radius is about 133°C. For a 0.1μm cavity radius the temperature to nucleate a bubble is about 432°C, well above the highest thermodynamic water superheat limit of 322°C.

Accordingly, for surfaces with cavity sizes well below 1μm, it is likely that homogeneous nucleation will occur since the liquid will reach the superheat limit before a bubble nucleates in a cavity. Micromachined surfaces tend to have very smooth surfaces. For instance, the platinum resistors are only 10μm wide, and 0.1μm thick, so it is unlikely that cavities will exist on the surface which are large enough for heterogeneous nucleation to occur. By etching cavities into the resistor substrate we can create sites for heterogeneous bubble nucleation, drastically reducing the superheat necessary to nucleate a bubble. This will be discussed further in later chapters, but the main advantages of placing a cavity in a heater are that a predictable site for bubble nucleation is created, and the heat required to do this is reduced.

2.2 Thermal Modeling

In order to better understand and control the bubble nucleation process on micromachined heaters, it is useful to model and predict the temperature distribution along and around the heater. The following sections will describe analytical and numerical models used to predict heat transfer in and around the resistive heaters.

2.2.1 Finite Element Model

Finite element models were created using CFD-ACE for three purposes. First, we wanted to explore the transient heat conduction around the heater. This was deemed necessary because if the heater was to be used in a cell-sorting device, we needed to confirm that the heat would not penetrate to the cells for the time that the heater was in use. The second purpose of the finite element modeling was to compare the heating resistors with and without etched cavities. It was necessary to confirm that a resistor with an etched cavity filled with air would heat up as fast as an unetched resistor in the vicinity of the cavity. Having a nucleation site that was significantly cooler than the rest of the heater would not have been an effective design, so this model was used to investigate the issue before the devices were fabricated.

The schematic of the geometry used in the finite element model is shown in Figure 2-2. The model is a cross section of a heater with a cavity etched into the substrate, and an adiabatic line of symmetry is placed through the center.

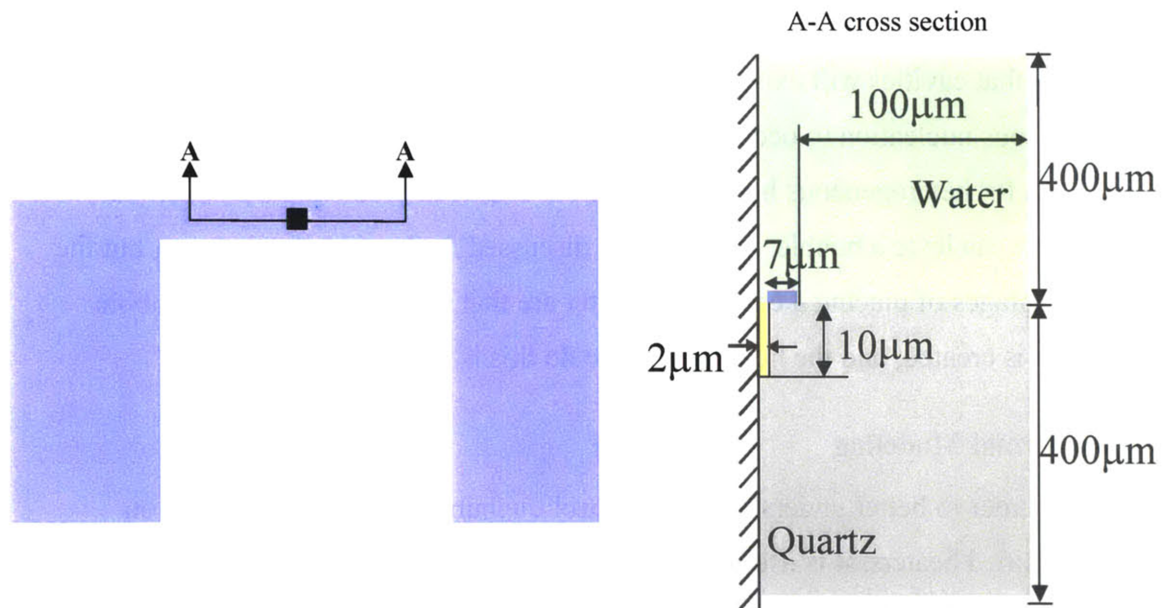

Figure 2-2 Schematic of finite element model. On the left is a diagram of a line heater. On the right is a cross-sectional slice through the heater, demonstrating the cavity geometry.

For the model, a constant heat generation was applied to the heater, and the boundary conditions were as follows. The center line was adiabatic, and the other three external boundaries were held at room temperature (300K). A transient thermal model

was run for a time of 50 milliseconds. The result of the simulation is shown in Figure 2-3.

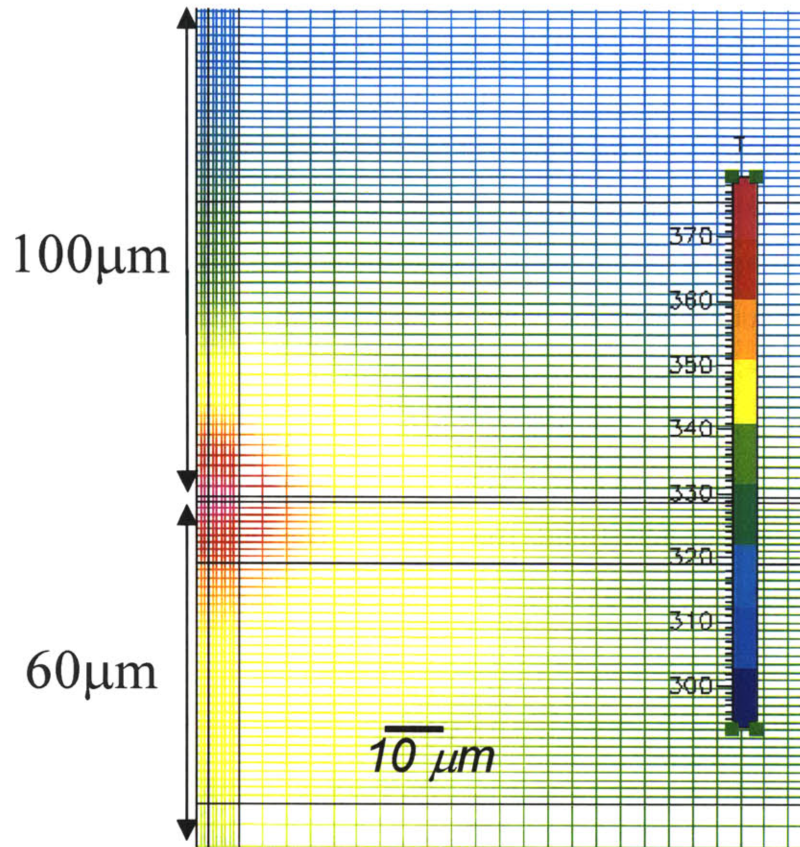

Figure 2-3 Results of finite element simulation of resistive line heater bounded by water and quartz. The view shown here is identical to the cross-section shown in Figure 2-2.

From the results of this model we were able to learn two things. First, for the 50 millisecond time step used, the heat only propagated up into the water 100μm. This was used as verification that cells trapped 450μm above the heater would not be subjected to any temperature variations due to the normal use of the heater that would be kept on less than 50 milliseconds. The second thing that we learned from the model was that the temperature in the center of a heater with a cavity, did not vary significantly from the center of a heater without a cavity under identical heating conditions. This was an encouraging result since it meant that having a cavity would not adversely affect the heating of a resistor, and was not surprising given the microscale dimensions involved.

2.2.2 *Analytical Model*

It is desirable to be able to predict the temperature of the resistive heater when a given electrical voltage is applied to it to verify the experimental measurements. We have a resistive heater on a quartz substrate with water on top of it, as shown in Figure 2-4. A one dimensional, lumped thermal model is used. We will assume that the heater area is the rectangular area, $A = (L_1)(L_2)$ with the heat uniformly generated in this area, instead of just using the area of the line heater alone since the elements of the heater are spaced by an amount equal to the width of the line heater. The thickness of the quartz wafer is L_q=450μm and an approximation for the length scale of the water is the width of the line heater: L_w=16μm. This assumption is made as a rough estimate that the heat will propagate approximately one heater width into the water. The actual thickness of the water layer is approximately 1mm. The dimensions and layout of the resistors will be discussed further in Chapter 3.

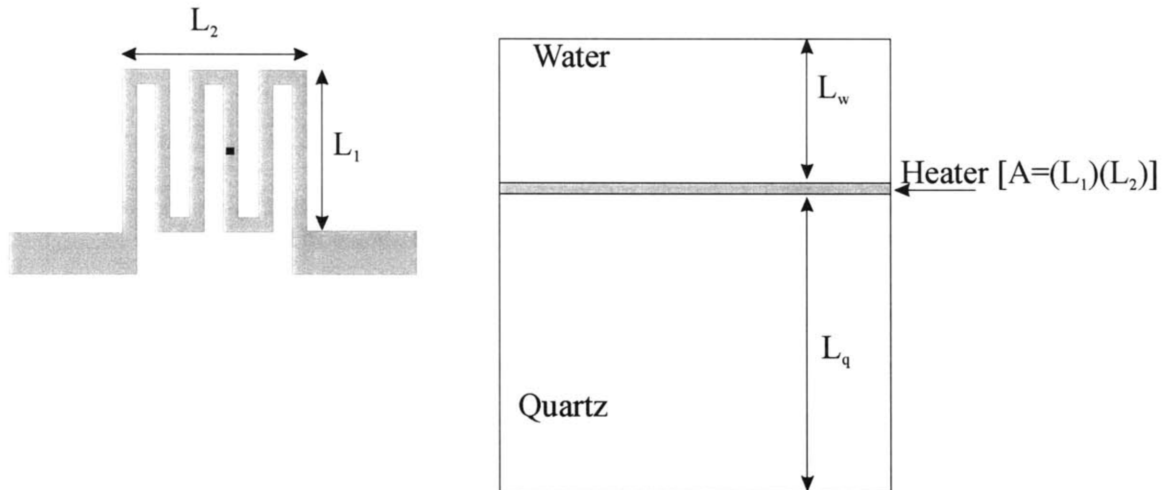

Figure 2-4 Schematic and boundary conditions for thermal model of resistor. On the left is the folded heater being modeled. The area used in the heater model is the total area spanned by the heater, A=(L1)(L2). On the right is a cross-sectional slice in order to show the water above the heater and the quartz substrate.

It is assumed that the ambient temperature is maintained at the top of the water layer, as well as at the bottom of the quartz substrate. The resistor is heated by applying a constant voltage pulse across it, generating ohmic heating, or power generation equal to I^2R for the

entire volume of the resistor. This system can be modeled using the thermal circuit shown in Figure 2-5.

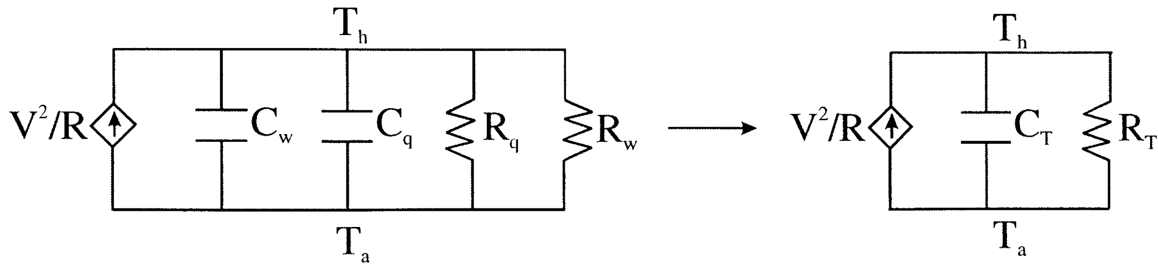

Figure 2-5 Thermal circuit model of heater, water, and quartz system.

The parameters are defined as follows:
V = constant voltage applied to heater (v)
R = Resistance of heater (Ω)
T_h = Temperature of heater (K)
T_a = Temperature of ambient (K)
C_w = Thermal capacitance of the water (J/K)
C_q = Thermal capacitance of the quartz (J/K)
C_T = Total thermal capacitance (J/K)
R_w = Thermal resistance of the water (K/W)
R_q = Thermal resistance of the quartz (K/W)
R_T = Total thermal resistance (K/W)
R_o = the resistance of the heater at room temperature (Ω)
α_R = the temperature coefficient of resistance = 0.0023 K^{-1}
K_w = Thermal conductivity of water = 0.611 W/mK
K_q = Thermal conductivity of quartz = 10.4 W/mK
c_w = Heat capacity of water (at T=300K) = 4178 J/kgK
c_q = Heat capacity of quartz = 745 J/kgK
ρ_w = Density of water (at T=300K) = 996 kg/m^3
ρ_q = Density of quartz = 2650 kg/m^3

The total thermal capacitance is calculated as follows, since the two capacitances are in parallel:

$$C_T = C_q + C_w \tag{2-7}$$

Each thermal capacitance is calculated as follows:

$$C_w = \rho_w A L_w c_w$$
$$Cq = \rho_q A L_q c_q \qquad \textbf{(2-8)}$$

The total thermal resistance is calculated as follows, since the two resistances are in parallel:

$$R_T = \frac{R_w R_q}{R_w + R_q} \qquad \textbf{(2-9)}$$

Each thermal resistance is calculated as follows:

$$R_w = \frac{L_w}{K_w A}$$
$$R_q = \frac{L_q}{K_q A} \qquad \textbf{(2-10)}$$

The resistance of the heater varies with temperature as follows:

$$R = R_o(1+\alpha_R T_h) \qquad \textbf{(2-11)}$$

The equation of this system is:

$$C_T \frac{dT_h}{dt} = -\frac{T_h}{R_T} + \frac{V^2}{R_o(1+\alpha_R T_h)} \qquad \textbf{(2-12)}$$

Assuming a small change in resistance we can linearize the model by expanding the denominator:

$$\frac{V^2}{R_o(1+\alpha_R T_h)} \approx \frac{V^2}{R_o}(1-\alpha_R T_h) \qquad \textbf{(2-13)}$$

Now the equation becomes:

$$\frac{dT_h}{dt} = -\frac{1}{C_T R_T}(1 + \frac{\alpha_R R_T V^2}{R_o})T_h + \frac{V^2}{C_T R_o} \quad \textbf{(2-14)}$$

From this we find that the time constant of the system is:

$$\tau = \frac{C_T R_T}{(1 + \frac{\alpha_R R_T V^2}{R_o})} \quad \textbf{(2-15)}$$

And the steady state temperature rise of the heater is:

$$\Delta T_{hss} = \frac{R_T V^2}{R_o + \alpha_R R_T V^2} \quad \textbf{(2-16)}$$

This model was validated experimentally, using a resistor with the geometry shown in Figure 2-4. Voltage pulses of varying magnitudes were applied to the heater, and the resulting average heater temperature was measured. The resulting plot is shown in Figure 2-6. (The details of the test set-up will be described in Chapter 5.)

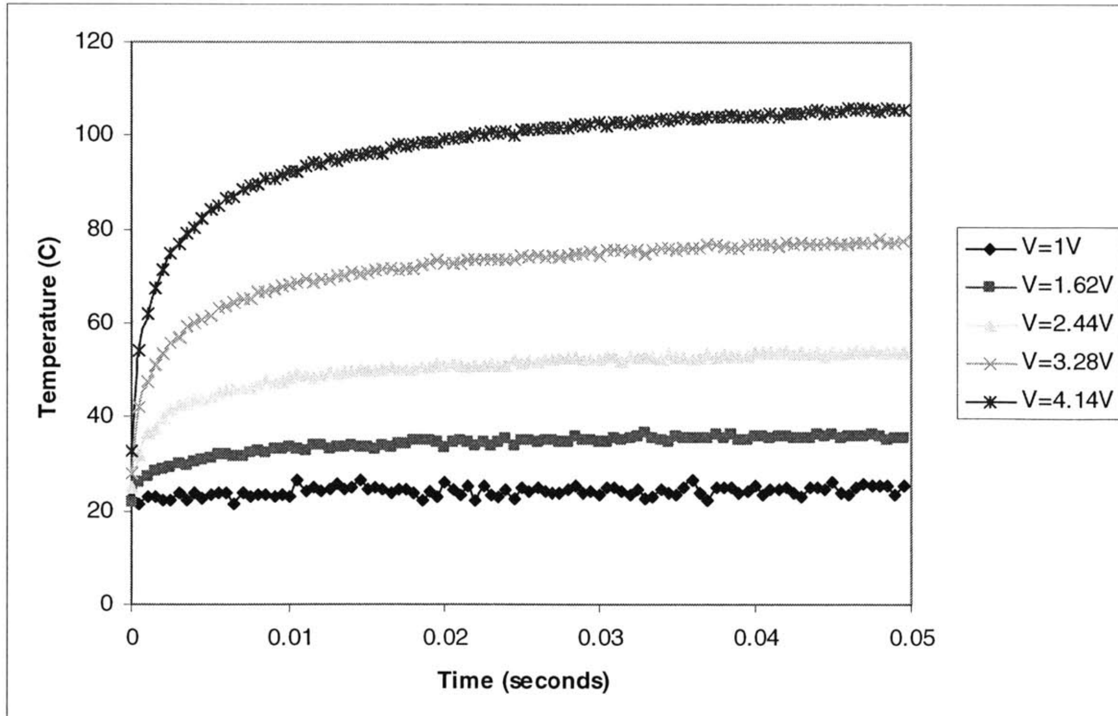

Figure 2-6 Plot of average heater temperature as a function of time for 50 millisecond voltage pulses of varying magnitude.

From these results, we were able to take the steady state temperature of the heater at each voltage level and compare it to the results from the model using Equation 2-16. This comparison is shown in Figure 2-7.

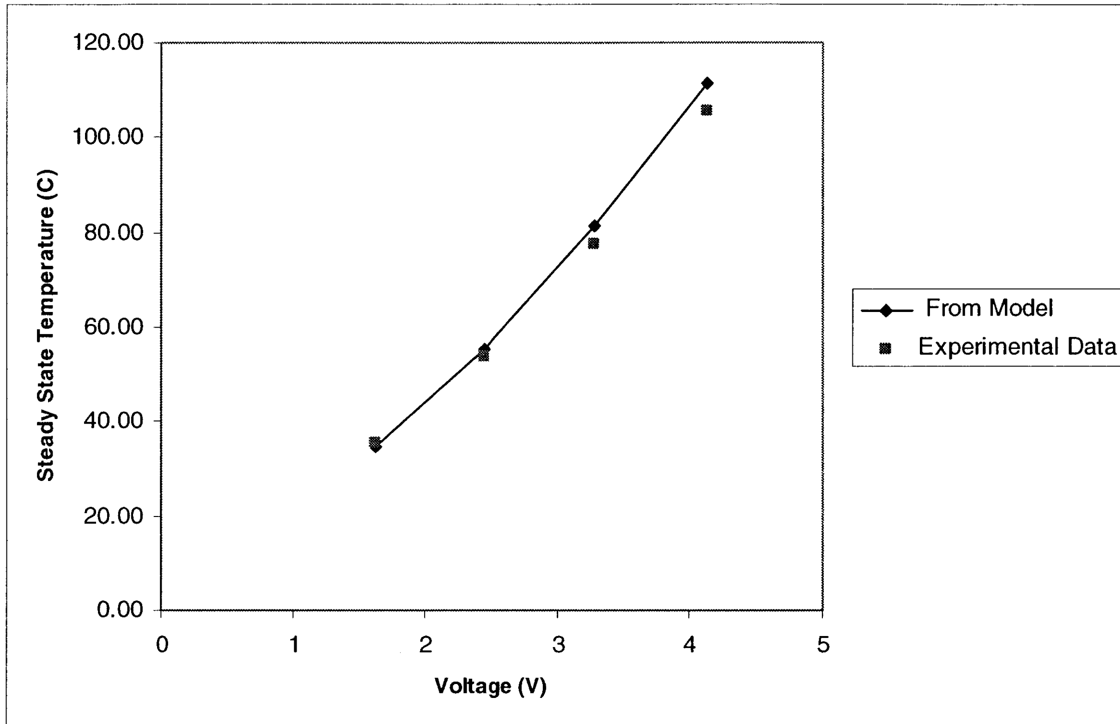

Figure 2-7 Comparison of steady state temperature of heater obtained from data and from the lumped thermal model. This data is taken from the results of heater testing in Figure 2-6.

From this comparison of the model to the experimental data, we can conclude that the lumped thermal model is adequate to predict the steady state temperature of the heater. Using equation 2-15, we can calculate the time constant of the system for V=3.28 Volts as τ=13.3 milliseconds. From Figure 2-7, we can see that this approximates the experimental data, but is a bit slower.

2.2.3 Finite Difference Models

Steady state two-dimensional thermal finite difference models were created in MATLAB in order to predict the temperature distribution along the heater for the two resistor geometries tested. The first generation heater geometry was a straight line heater, while the second generation heater was a folded line resistor (Figure 2-8). By knowing

the temperature distribution along each heater, we can estimate the bubble formation temperature for a particular location on the heater, since only the average heater temperature can be experimentally measured.

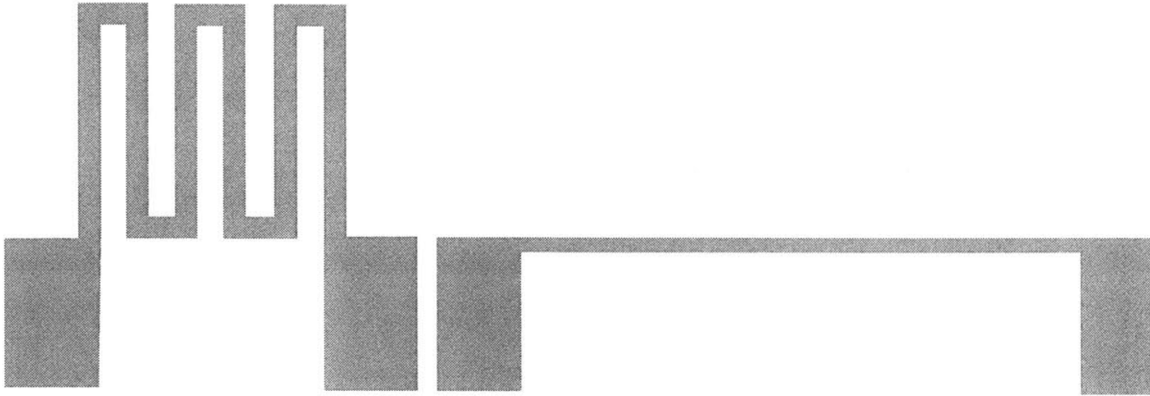

Figure 2-8 Two resistor geometries modeled. On the left is the folded resistor, and on the right is the line resistor.

The finite difference model was constructed by breaking each geometry into many smaller control volumes, and then using conservation of energy on each piece. A sample control volume is shown in Figure 2-9.

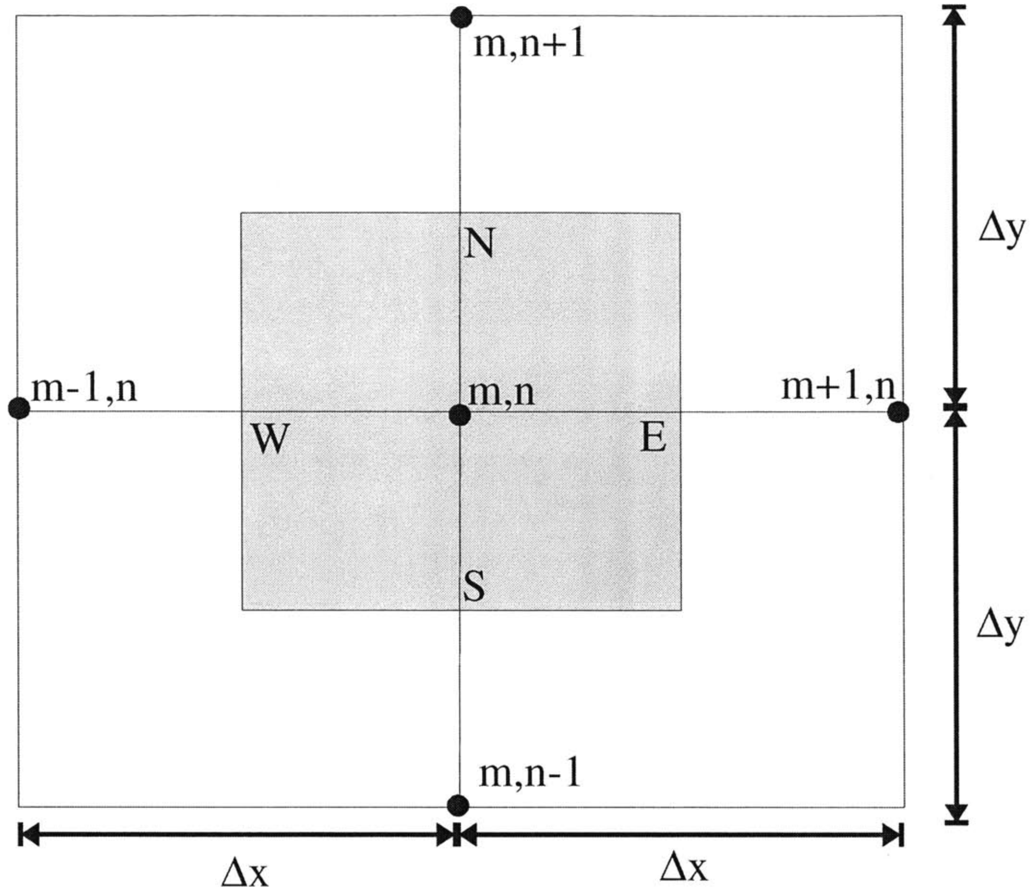

Figure 2-9 Sample control volume for finite difference model.

The energy balance on this volume can be written as:

$$0 = \dot{Q}_x\Big|_W + \dot{Q}_x\Big|_S - \dot{Q}_x\Big|_E - \dot{Q}_x\Big|_N + \Delta\dot{Q}_V \tag{2-17}$$

Each term in this equation is calculated as follows:

$$\dot{Q}_x\Big|_W = -k\frac{\partial T}{\partial x}\Big|_W \Delta y \cdot 1 = -k\,\frac{T_{m,n} - T_{m-1,n}}{\Delta x}\Delta y \tag{2-18}$$

$$\dot{Q}_x\Big|_E = -k\frac{\partial T}{\partial x}\Big|_E \Delta y \cdot 1 = -k\,\frac{T_{m+1,n} - T_{m,n}}{\Delta x}\Delta y \tag{2-19}$$

$$\dot{Q}_x\Big|_S = -k\frac{\partial T}{\partial y}\Big|_S \Delta x \cdot 1 = -k\,\frac{T_{m,n} - T_{m,n-1}}{\Delta y}\Delta x \tag{2-20}$$

$$\dot{Q}_x\Big|_N = -k\frac{\partial T}{\partial y}\Big|_N \Delta x \cdot 1 = -k\frac{T_{m,n+1} - T_{m,n}}{\Delta y}\Delta x \quad \textbf{(2-21)}$$

$$\Delta\dot{Q}_V = \dot{Q}_V'''\Delta x \Delta y \cdot 1 \quad \textbf{(2-22)}$$

For the line resistor, the meshed schematic with boundary conditions is shown in Figure 2-10. Each square is 5μmx5μm, and an adiabatic line of symmetry is used in the center of the heater. The resistor is 200μm long and 10μm wide. The distance from the heater to the ambient temperature boundary condition is 20μm and was determined by estimating the penetration depth of the heat into the quartz for a 50 millisecond time as shown below (the relevant experimental data uses time less than or equal to 50ms):

$$L \approx \sqrt{\tau\alpha} = 16\mu m \quad \textbf{(2-23)}$$

Where L is the penetration depth, τ is the time of 50msec, and α is the thermal diffusivity of the quartz of 5.27×10^{-6} m^2/sec. For the purpose of the model, L=20μm was chosen as a conservative estimate.

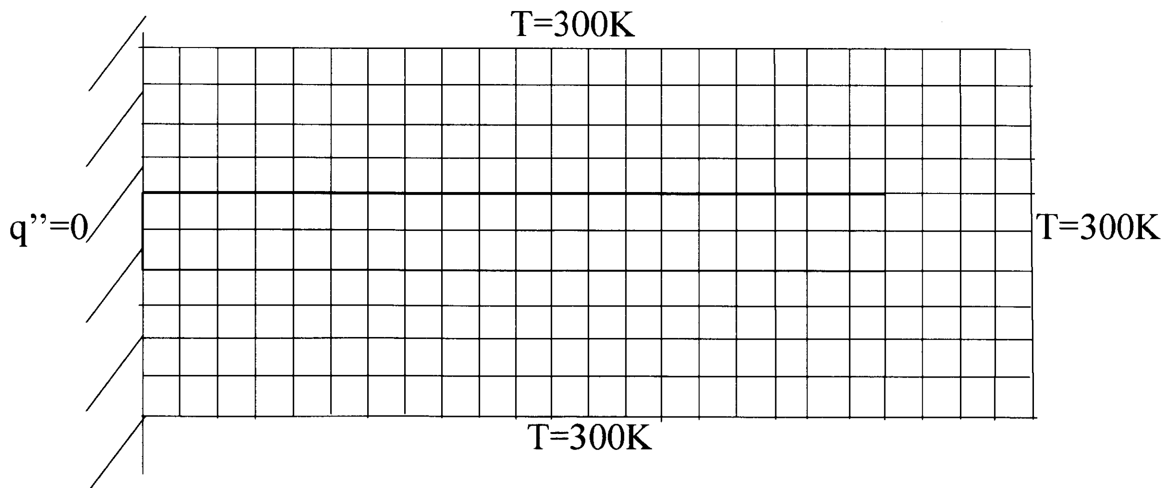

Figure 2-10 Meshed finite difference model of line heater.

The results of this simulation are shown in Figure 2-11. It is important to note that while the model is able to predict the temperature distribution along the heater, it

neglects conduction in the third dimension and thus cannot accurately predict the actual magnitude of the temperature. The MATLAB code for this model is in Appendix D.

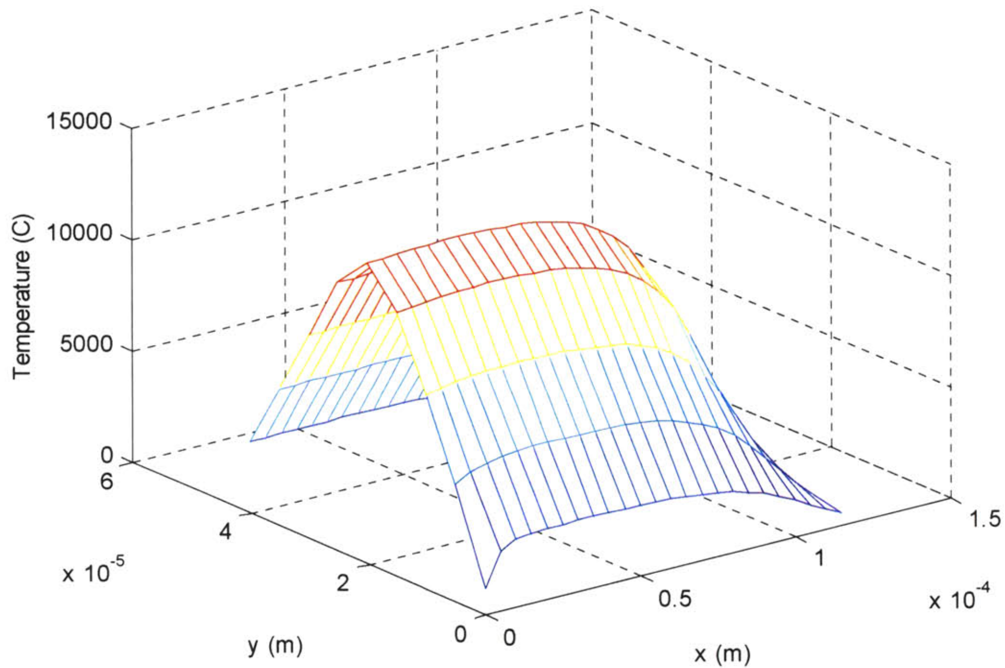

Figure 2-11 Finite difference model temperature distribution results.

The schematic of the folded resistor model with boundary conditions is shown in Figure 2-12. Once again, we use an adiabatic line of symmetry through the center of the heater. As with the model above, the squares are 5μmx5μm, and the penetration depth is L=20μm. The resistor, when unfolded, is 650μm long and 10μm wide. The MATLAB code for this model is in Appendix E.

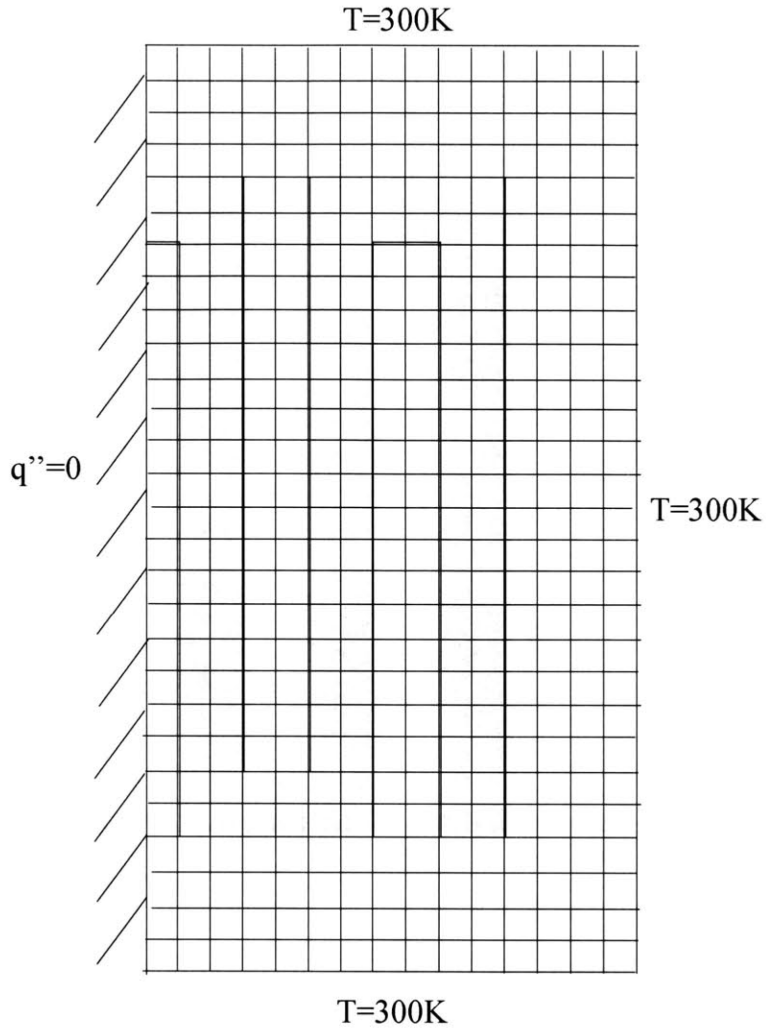

Figure 2-12 Schematic and boundary conditions for folded resistor model.

The results of the finite difference simulation are shown in Figure 2-13. It is important to note that there is significantly more temperature variation along the length of the folded heater than along the straight heater.

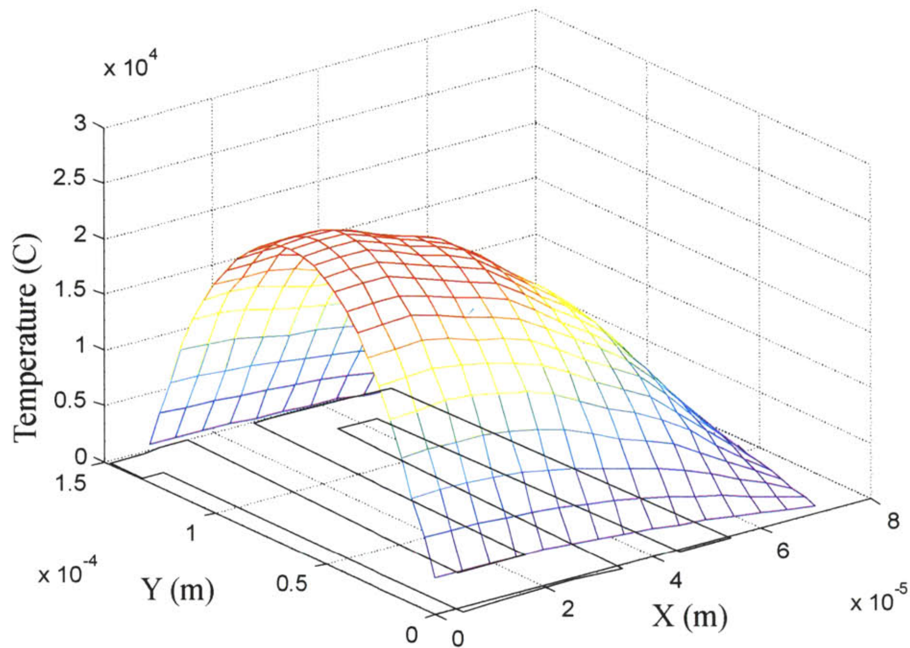

Figure 2-13 Results of finite difference simulation for the folded resistor.

In order to make the simulation results more applicable to the experimental data, the simulations were used to calculate the temperature at various points on the heaters as functions of the average heater temperature. This was chosen because the average heater temperature is the only quantity that may be experimentally measured. These results are shown in Table 2-2.

Heater Geometry	Position	Percentage Difference from Average Temperature
Straight	Center	+7.9%
Straight	50μm from Edge	+7.7%
Straight	Right Edge	-47.6%
Folded	Center	+44%
Folded	Top Edge	-12%
Folded	Bottom Edge	-17%
Folded	Right Edge	-15%

Table 2-2 Heater temperature distribution results from finite difference model.

For the straight heaters, because bubbles usually form in the center 100μm of the heater, we can see that the temperature distribution is quite uniform, and near the average heater temperature. Conversely, for the folded heater, we can see that it is important to know where the bubble forms since the temperature distribution is much less uniform. Thus, inferring the temperature of bubble formation will require consideration of the position of bubble formation.

2.3 Bubble Collapse

In the previous chapter, we saw that complete bubble collapse is crucial to the operation of a bubble-powered device, however, many groups have had difficulty accomplishing this. At equilibrium, a small amount of air is dissolved in water, and the solubility of air in water decreases as the temperature of the liquid increases. Accordingly, when water is boiled, some of the dissolved air comes out of solution and diffuses into the vapor bubble. Because the bubble is no longer filled completely with vapor, the bubble collapse could be limited by both heat transfer/phase change and gas diffusion. In the following sections we will explore both of these bubble collapse mechanisms, and perform order of magnitude estimations of bubble collapse time in the limiting cases of a vapor bubble or an air bubble.

2.3.1 Phase Change Collapse

In this section, we will calculate the time it will take for a 40μm diameter bubble, filed entirely with water vapor, to condense completely into the surrounding water. In order to solve for this time, we will use the relations derived by Mikic and Rohsenow[61].

The parameters are defined as follows:
T_b = bulk fluid temperature = 300K
T_{sat} = saturation temperature = 373K
T_w = wall temperature = 411K
α_{water} = thermal diffusivity of water (evaluated at 373K) = $1.69 \times 10^{-7} m^2/s$
r_{max} = maximum bubble radius = 20μm
t_w = waiting time (time before bubble forms)
h_{fg} = latent heat of vaporization of water = $2.26 \times 10^6 J/kg$

c_l = specific heat of water (evaluated at T=373K) = 4212J/kgK
Ja = Jakob Number
ρ_l = density of liquid water (evaluated at T=373K) = 958kg/m^3
ρ_v = density of vapor (evaluated at T=373K) = 0.5977kg/m^3
t_{max} = time at which bubble has reached maximum size
t_{full} = total bubble growth and collapse time

The expression for the bubble radius as a function of time that was derived in the paper can be used to calculate bubble growth time and collapse time. The differential equation for the bubble radius as a function of time is given as:

$$\frac{dr}{dt} = \frac{k\sqrt{3}}{\rho_v h_{fg}}\left(\frac{T_w - T_{sat}}{\sqrt{\pi\alpha t}} - \frac{T_w - T_b}{\sqrt{\pi\alpha(t + t_w)}}\right) \quad \textbf{(2-24)}$$

We can now set dr/dt=0 to solve for t_{max}, the time it takes for the bubble to reach its maximum size.

$$t_{\max} = \frac{(T_w - T_{sat})^2 t_w}{(T_w - T_b)^2 - (T_w - T_{sat})^2} \quad \textbf{(2-25)}$$

The expression for the bubble radius as a function of time is:

$$r = \frac{2}{\pi}\sqrt{3}Ja\sqrt{\pi\alpha t}\left(1 - \frac{T_w - T_b}{T_w - T_{sat}}\left[\sqrt{1 + \frac{t_w}{t}} - \sqrt{\frac{t_w}{t}}\right]\right) \quad \textbf{(2-26)}$$

The Jakob number may be computed as follows:

$$Ja = \frac{(T_w - T_{sat})c_l\rho_l}{h_{fg}\rho_v} = 113.48 \quad \textbf{(2-27)}$$

We can use iteration in order to find the proper combination of t_w and t_{max} to achieve r_{max}=20μm, using Equations (2-25) and (2-26). In this way we find that $t_w=1.54\text{x}10^{-6}$s and $t_{max}=2\text{x}10^{-7}$. Now we can solve for the total bubble growth and collapse time, t_{full}, by setting r=0 in Equation (2-26), and use this to find the bubble collapse time, $t_{collapse}$.

$$t_{full} = 9.1x10^{-7}\,s \rightarrow t_{collapse} = t_{full} - t_{\max} = 7.1x10^{-7}\,s \quad \textbf{(2-28)}$$

In summary, we have been able to estimate the collapse time of a 40μm diameter bubble filled entirely with vapor as being 0.7μs, which can serve as the lower limit for bubble collapse. However, it is important to note that because the heater is on for 50

milliseconds in practice, that the collapse time must begin after the heater is turned off. Hence, from the point of bubble formation, the time it takes for the bubble to collapse is on the order of 50 milliseconds, since the cooling time is similar to the heating time.

2.3.2 *Diffusion Collapse*

For the case when the bubble is filled completely with air, we will calculate the amount of time it would take for a 40μm diameter bubble to diffuse completely into the surrounding water. For this calculation, we will assume an infinite amount of water surrounding the bubble with no air far from the bubble.

The parameters are defined as follows:
$\dot{m}$ = mass transfer rate of air from bubble to water
h_m = mass transfer coefficient
A = surface area of spherical bubble = πD^2
Δc = concentration difference of air between right outside the bubble and at infinity
ρ_g = density of air at 1 atm of pressure and T=300K = 1.177kg/m^3
C_{He} = Henry constant for air in water = 74000
He_{air} = Henry number for air in water
$x_{air,u}$ = mole fraction of air in water just outside bubble
$x_{air,s}$ = mole fraction of air just inside bubble = 1 (assume pure air in bubble)
r_o = initial bubble radius = 20μm = $D_o/2$
D_{12} = diffusion coefficient of air into water
Sc = Schmidt number for air in water at T=300K = 323
μ = dynamic viscosity of water at T=300K = 8.67x10^{-4}kg/ms
ρw = density of water at T=300K = 996kg/m^3

The mass transfer relation can be written as:

$$\dot{m} = h_m A \Delta c = h_m \pi D^2 \Delta c \tag{2-29}$$

The mass transfer may be modeled as quasistatic, which is analogous to heat conduction. Using this analogy between heat transfer and mass transfer, the Nusselt Number for conduction from a sphere may be written as follows for this mass transfer case[62]:

$$\frac{h_m D}{D_{12}} = 2 \tag{2-30}$$

Substituting this into Equation (2-29):

$$\dot{m} = 2\pi D D_{12}\Delta c = 4\pi r D_{12}\Delta c \tag{2-31}$$

Using conservation of mass we can find another relation for $\dot{m}$ and equate it to Equation (2-31):

$$\dot{m} = -\frac{d}{dt}\left(\frac{4}{3}\pi r^3 \rho_g\right) = -\rho_g 4\pi r^2 \frac{dr}{dt} = 4\pi r D_{12}\Delta c \tag{2-32}$$

Separating the variables and integrating, we get:

$$-\int_{r_o}^{r} r dr = \int_0^t \frac{D_{12}\Delta c}{\rho_g} dt \rightarrow \frac{1}{2}\left(r_o^2 - r^2\right) = \frac{D_{12}\Delta c}{\rho_g} t \tag{2-33}$$

For complete bubble collapse, the radius of the bubble must equal zero, giving us the time for bubble collapse:

$$t = \frac{r_o^2 \rho_g}{2D_{12}\Delta c} \tag{2-34}$$

In order to solve for this time, we must first determine D_{12}. We do this using the definition of the Schmidt Number:

$$Sc = \frac{\mu}{\rho_w D_{12}} \tag{2-35}$$

Substituting for the known variables we find $D_{12}=2.69\text{x}10^{-9}\text{m}^2/\text{s}$. To solve for Δc, we can use the assumption that c=0 (no air dissolved in the water) infinitely far from the bubble. To find the concentration of air in the water just outside the bubble, we can use the definition of the Henry Number.

$$He = \frac{x_{air,s}}{x_{air,u}} \rightarrow x_{air,u} = \frac{1}{74000} = 1.35x10^{-5} \tag{2-36}$$

Using this, we can solve for Δc:

$$\Delta c = x_{air,u}\rho_g - 0 = 1.59x10^{-5} \tag{2-37}$$

Using the known quantities, we can now solve for the bubble collapse time for a bubble filled with pure air as $t = 5504$ seconds, or about 92 minutes. This value can serve as the upper bound on bubble collapse time for a 40μm diameter bubble. For both bubble collapse regimes, the collapse time is proportional to the square of the bubble radius.

3 DESIGN

The design problems addressed in this thesis are twofold. First, resistive heaters were designed in such a way as to make the microbubble formation process more controllable. Second, these heaters were used in a device that was designed to capture, hold, and release bioparticles for a cell analysis system.

3.1 Resistive Heaters

In order to accomplish controllable bubble formation, it was necessary to design resistive heaters with geometries and surface properties conducive to bubble formation. The goals were to have bubbles form in a predetermined location at reduced temperatures (relative to unpatterned heaters), and then to collapse completely after the heater was turned off. The design of the resistive heaters addresses the first two goals, of bubble formation location and temperature. The bubble collapse is determined by water preparation, and will be addressed in a later chapter.

For heterogeneous bubble nucleation, a bubble is nucleated in a small surface defect, or cavity. Larger cavities result in a lower superheat for bubble formation, as a large cavity is able to trap more gas and vapor to act as the nucleation seed. This principle was used in the design of the resistive heaters. Because micromachined surfaces are very smooth, they lack surface defects that are adequately sized to nucleate bubbles at low superheat. Micromachining was used to etch cavities into the quartz substrate in order to form nucleation sites for bubble formation. In this way, bubbles would be far more likely to form in the cavities than they would be to form elsewhere on the heater, and bubble formation location could be controlled. Additionally, a lower surface temperature would be required to nucleate the bubble in a cavity, so bubble formation temperature would be lower, and more repeatable since the same nucleation site would be used each time. A schematic of a resistive heater with a cavity etched into the substrate is shown in Figure 3-1.

Figure 3-1 Resistive heater with cavity etched into substrate. r_c is the cavity radius.

Because quartz and platinum are hydrophilic, it was unclear how effective the cavities would be at trapping gas. Two hydrophobic surface treatments were tested, and were found to make the bubble nucleation sites more effective, allowing them to trap more gas (Figure 3-2).

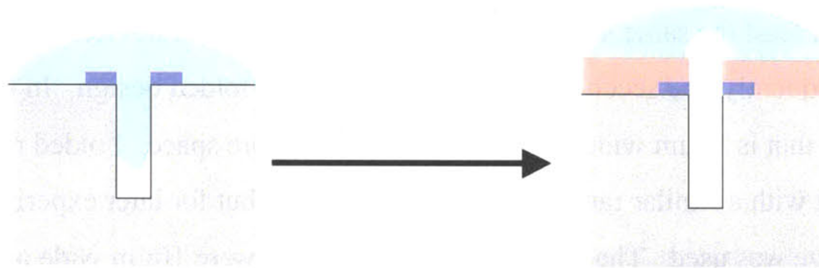

Figure 3-2 Illustration of the effect of hydrophobic surface treatments. On the left is a resistor cavity with no surface treatment, on the right is a resistor cavity with a hydrophobic surface coating. The hydrophobic surface results in more gas trapped in the cavity when water is on the top surface.

The two surface treatments used are significantly different. One way of rendering a surface hydrophobic is to silanize it[63]. This process, which will be described in the next chapter, deposits a monolayer of hydrophobic molecules that covalently bond to the wafer surface. This treatment does not measurable change the contact resistance to the wafer surface, nor does it act as a thermal insulator. The second treatment used was CYTOP^{TM}, a spin-coated polymer. This material is deposited in a layer 1-2μm thick. Hence, it acts as both a thermal and electrical dielectric, raising the temperature that the heater must reach to form a bubble, and complicating electrical contact. However, this coating can also be used to bond quartz to silicon, and was thus beneficial in the

fabrication of the complete bioparticle actuator. The surface treatments are depicted in Figure 3-3.

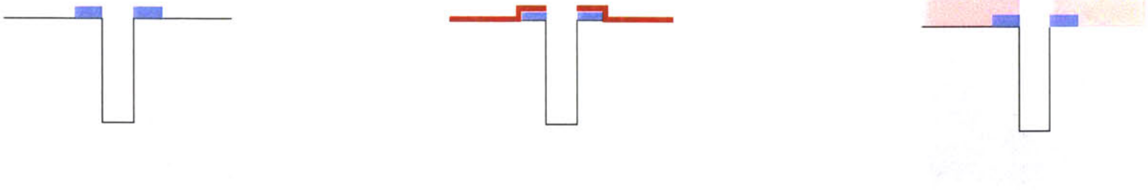

Figure 3-3 Illustration of surface treatments for the resistive heaters. On the left is an untreated surface, in the center is a silanized surface, and on the right is a CYTOP^{TM}-coated surface.

The resistive heaters are fabricated using thin-film platinum with a thin titanium adhesion layer on a quartz substrate. (The fabrication process will be described in the following chapter) As described in the previous chapter, two geometries were used for the heaters (Figure 3-4). The first generation heater was a straight line heater, and a variety of them were fabricated ranging from 200μm-1000μm in length and 10μm-20μm in width. It was later determined that these resistors were too long, requiring bubble chambers of at least the same length. This limited the number of devices that could fit on a chip. Consequently, the second generation heaters use a folded design. In this way, a 650μm heater that is 10μm wide can fit into a 100μm square space. Folded resistors were designed with a similar range of widths and lengths, but for later experiments, only one resistor size was used. The dimensions of this design were 10μm wide and 650μm long, however, due to the fabrication process, the actual resistor width was 16μm.

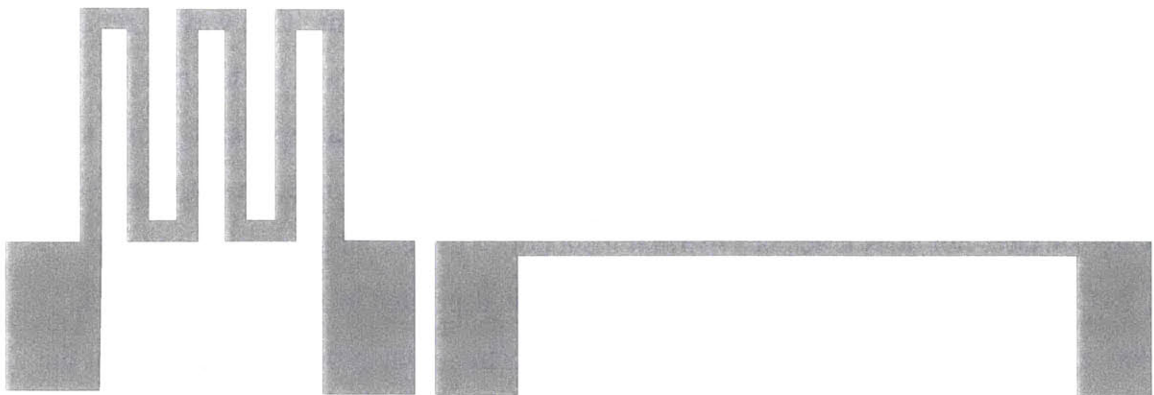

Figure 3-4 Resistive heater geometries. The first generation line heater is on the right, and the second generation folded heater is on the right.

For the first generation resistor, a single cavity was positioned in the center of the heater. The cavities were 5μm square and ranged in depth from 5μm-15μm. For the second generation heaters, single cavities of the same dimensions were placed in one of two possible regions on the heater. These cavities were placed in either the center of the heated field, or else on the edge of the heated field (Figure 3-5). From our modeling results we know that there is a great deal of temperature variation between these two areas, so the cavities were placed this way in order to explore this effect.

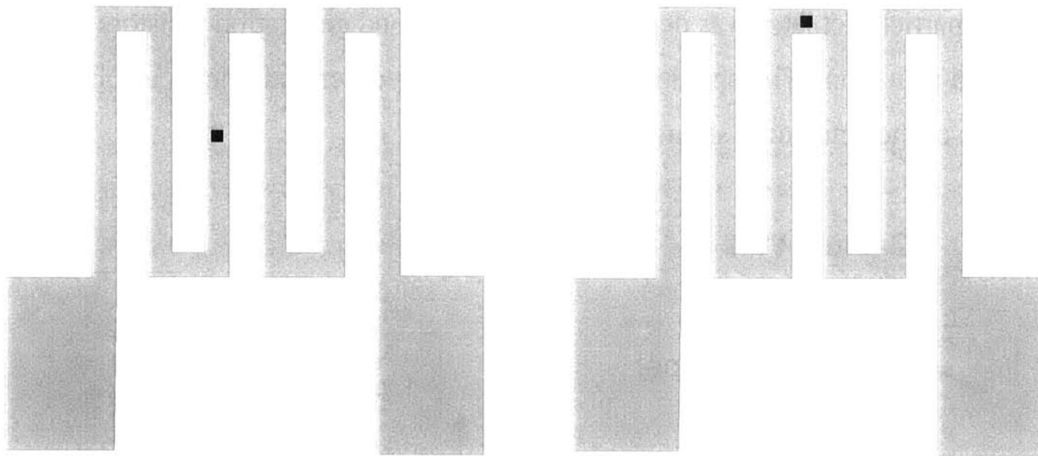

Figure 3-5 On the left is a folded resistor with a cavity in the central region of the heater. On the right is a resistor with the cavity on the edge of the heated field.

Table 3-1 lists all of the resistor geometries tested.

Resistor Shape	Width	Length	Cavity	Coating
line	10μm	200μm	none	none
line	10μm	200μm	none	silanization
line	10μm	200μm	none	CYTOP™
line	10μm	200-1000μm	6μm wide, 20μm deep	none
line	10μm	200-1000μm	6μm wide, 20μm deep	silanization
line	10μm	200-1000μm	6μm wide, 20μm deep	CYTOP™
folded	13μm	650μm	none	none
folded	13μm	650μm	none	silanization
folded	13μm	650μm	5μm wide, 5μm deep, edge	silanization

folded	13μm	650μm	5μm wide, 5μm deep, center	silanization
folded	13μm	650μm	5μm wide, 15μm deep, edge	silanization
folded	13μm	650μm	5μm wide, 15μm deep, center	silanization
folded	16μm	1270μm	6μm wide, 4μm deep, center	silanization

Table 3-1 Resistor geometries used in testing.

3.2 Bioparticle Actuator

The bioparticle actuator was designed using the second generation resistors for bubble-powered actuation. The operation of the device was described briefly in Chapter 1. A schematic of the actuator is shown in Figure 3-6.

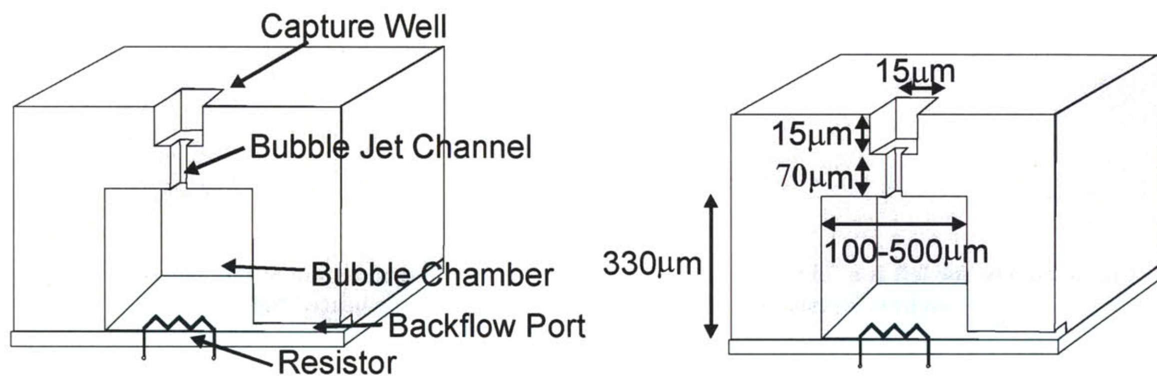

Figure 3-6 Schematic of components and dimensions of the microbubble cell actuator.

The capture wells were designed to capable of holding no more than one bioparticle. The particles used in testing at approximately 10μm in diameter, so the wells were sized at 15μm square. The depth was also chosen to be 15μm since the hydrodynamics would result in the particle remaining trapped, even with a bulk flow over the top of the wafer [64]. The bubble jet channel was designed to be 5μm square so that it would not be possible for the tested particles to be drawn into the bubble chamber below. The bubble chambers were designed to be large enough to fit the folded resistors completely. Because of manual alignment of the silicon chip to the quartz chip, it was necessary to have a generous tolerance in the bubble chamber size. Hence, the chambers ranged from 100μm-500μm square, depending on the size of the resistive heaters which

ranged from 50μm to 300μm square. The backflow ports were designed to have an order of magnitude higher fluidic resistance than the bubble jet channels. For this reason, when a bubble is formed, the majority of fluid is ejected up through the bubble jet channel and not out through the backflow port. All of the backflow ports are connected to the same outlet, so that a back pressure may be applied to the whole chip at once, and eliminating the need for a multitude of fluidic connections on the chip.

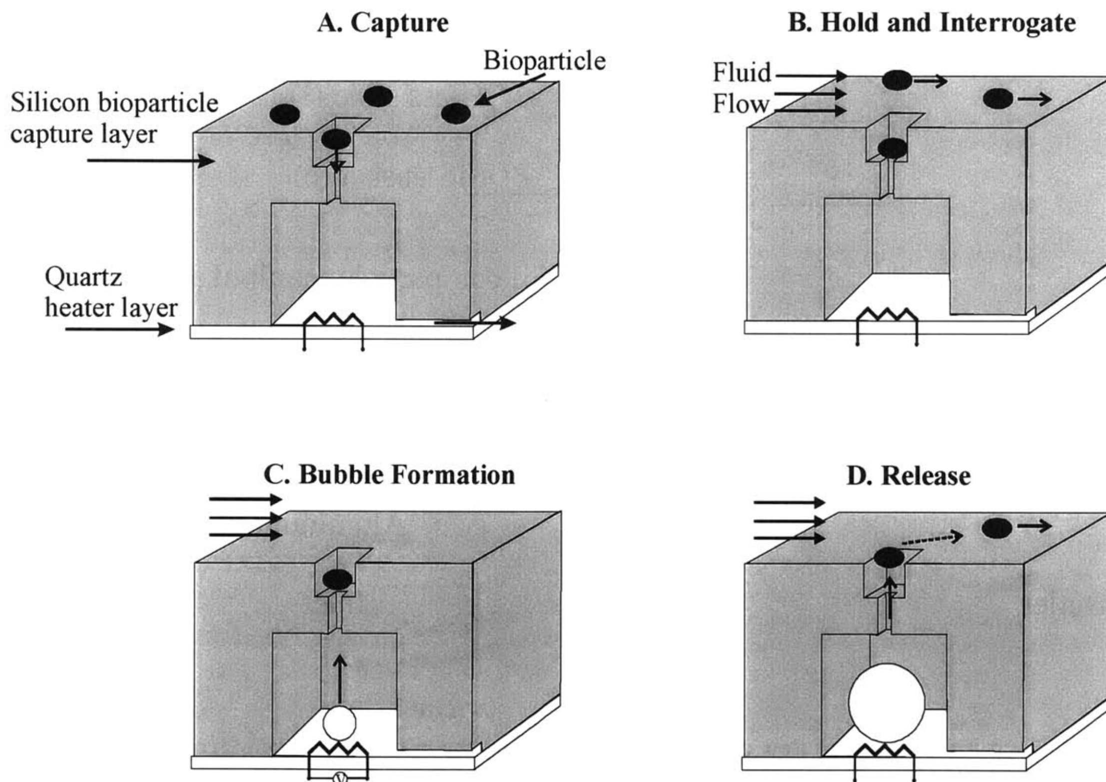

Figure 3-7 Operation of the microbubble cell actuator.

Figure 3-7 depicts the prototype device that provides a well into which a bioparticle (e.g., a cell) is trapped using a pressure gradient. The particle can then be selectively released by localized microbubble actuation wherein a heater creates a bubble in the bubble chamber (situated immediately below the particle well). The expanding bubble expels a jet of fluid that carries the bioparticle out of the well.

3.3 Flow System

In order to use the microbubble actuator, it is necessary to have a flow chamber to provide fluidic connections, introduce the bioparticles, and maintain the bulk flow. The schematic of the flow chamber is shown in Figure 3-8 and the dimensions are shown in Figure 3-9.

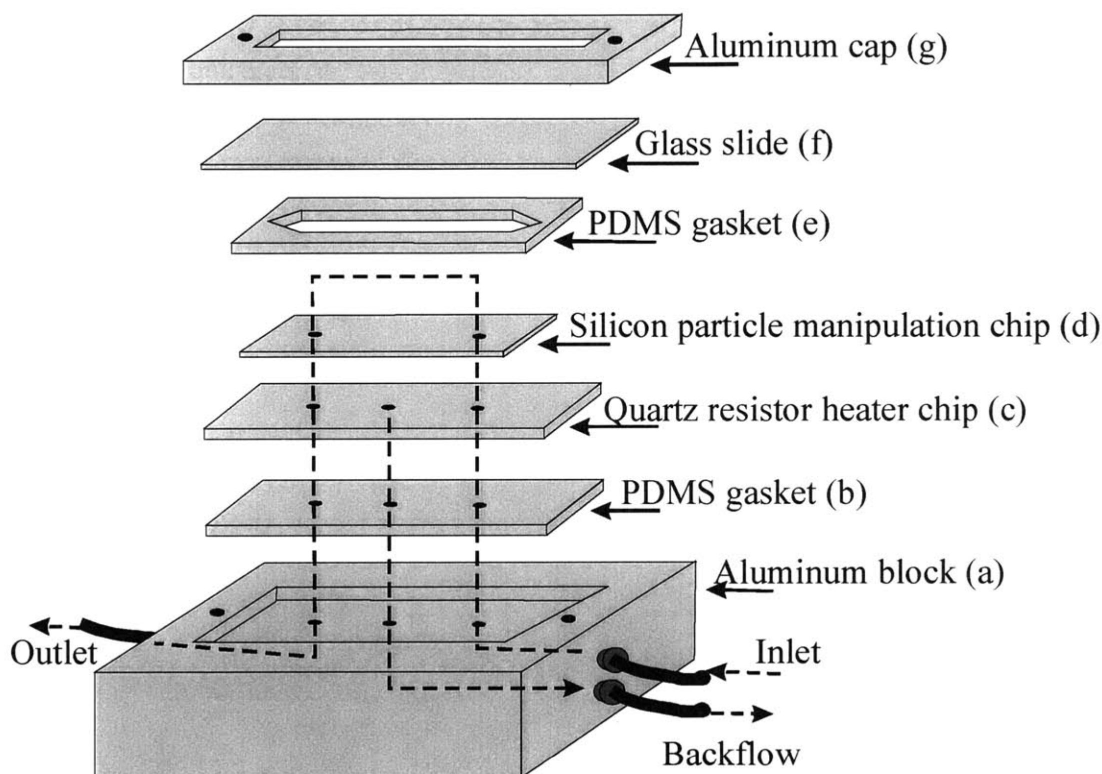

Figure 3-8 Schematic of flow chamber used in testing the microbubble bioparticle actuator.

A syringe pump (KD Scientific KDS200, New Hope, PA) is used to flow fluid and/or bioparticles over the top of the chip and out through the outlet. In addition to the inlet and outlet for the fluid across the top of the chip, there is an additional port that is used to provide a pressure drop to draw particles into the capture wells. An aluminum block (a) is machined with inlets and an outlet, and a depression in which the chip can sit. A PDMS (polydimethyl siloxane, Sylgard 184, Dow Corning) gasket (b) rests in the depression. On top of this gasket sits the quartz resistor chip (c), with drilled holes for the inlet, outlet, and backflow, and is bonded to the silicon chip (d), which has holes drilled for the inlet and outlet flow. Another PDMS gasket (e) is placed on top, which is covered by a glass slide (f). The top aluminum cap (g) is screwed down into the

aluminum base to create a fluidic seal. Using this flow chamber, the bulk flow over the device, as well as the particle capture, may be realized.

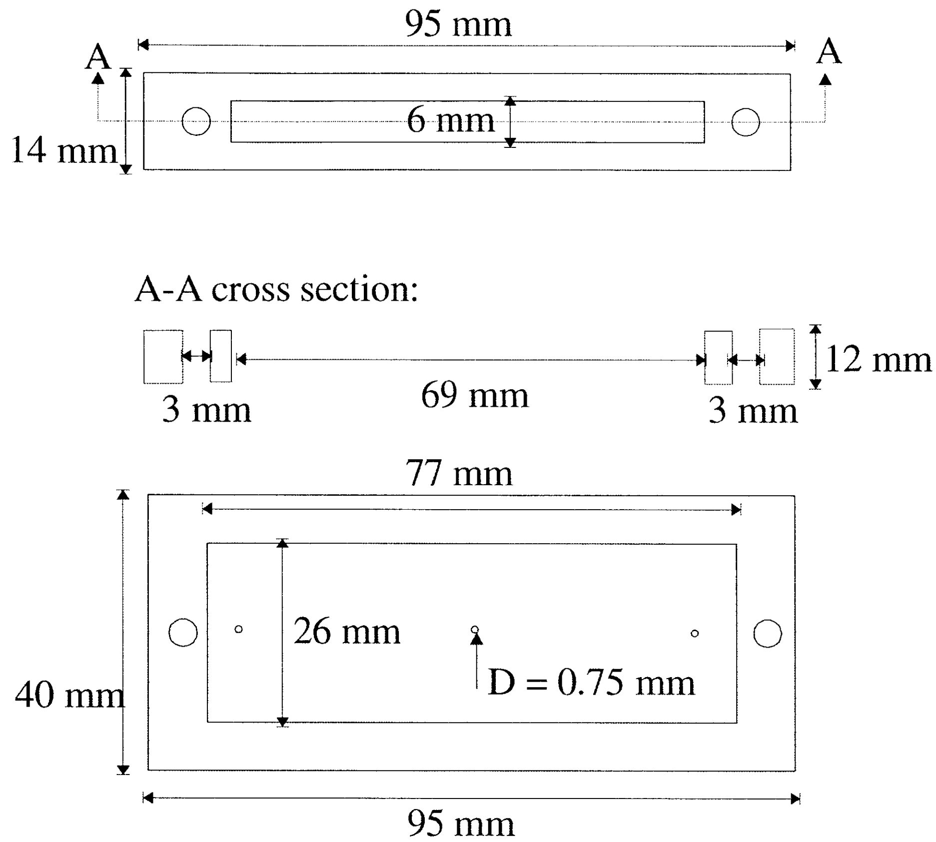

Figure 3-9 Dimensions of flow chamber.

4 FABRICATION

Microfabrication is necessary in order to produce the resistive heaters with cavities, as well as the full microbubble actuator. The heaters are built on quartz wafers, and serve as the bottom layer of the actuator. The top layer of the actuator is fabricated from silicon, and the two layers are bonded in the final step to form the full device. This chapter describes the processes used to fabricate all of the components, as well as the complete bioparticle actuator.

4.1 Quartz Process

The bottom layer of the device contains the microetched cavity and the heater layer for controlled bubble formation. The process flow for this layer is shown in Figure 4-1. A 4 inch diameter quartz wafer is coated with a 1μm polysilicon layer by low pressure chemical vapor deposition (LPCVD). The microcavities are then patterned using standard photolithography (OCG834 photoresist spin-coated at 2500rpm), and then the pattern is etched into the polysilicon using a plasma etch. Next the quartz is etched, using the polysilicon as a hard mask, with a CHF_3 plasma for 75-130 minutes depending on the desired depth. After this the polysilicon mask is stripped in SF_6 plasma, and the resistors are patterned with photoresist for a lift-off process. A 100Å adhesion layer of titanium followed by 1000Å of platinum is deposited by an electron beam tool, then any metal on top of photoresist is lifted off when soaked in acetone. The final step is to anneal the wafers at 600°C in nitrogen for one hour. The anneal ensures that the temperature/resistance characteristic of the platinum remains constant for the range of temperatures (100-300°C) reached in testing. The detailed process flow is in Appendix A.

Some of the quartz resistor wafers were coated with either CYTOP™ (Sigma-Aldrich, Milwaukee, WI)[65] or silanized to render the surfaces hydrophobic. The method for CYTOP™ deposition is to prebake a quartz resistor wafer on a hotplate at 90°C for 30 minutes, then spin on the CYTOP™ at 2000rpm for 30 seconds (1μm thickness), then postbake on a hotplate at 90°C for 30 minutes[66]. CYTOP™ is a spin-coated cyclized perfluoro polymer and the exact chemical properties are described in the paper referenced above.

To silanize a wafer it is put in a vacuum jar with a dish containing a few drops of a silanizing compound (tridecafluoro-1,1,2,2-tetrahydrooctyl-1-trichlorosilane, United Chemical Technologies, Bristol, PA) and then pumped down to the mTorr level for two hours[63]. When a wafer is silanized, a monolayer of silane molecules bond to the wafer surface covalently, rendering the surface hydrophobic.

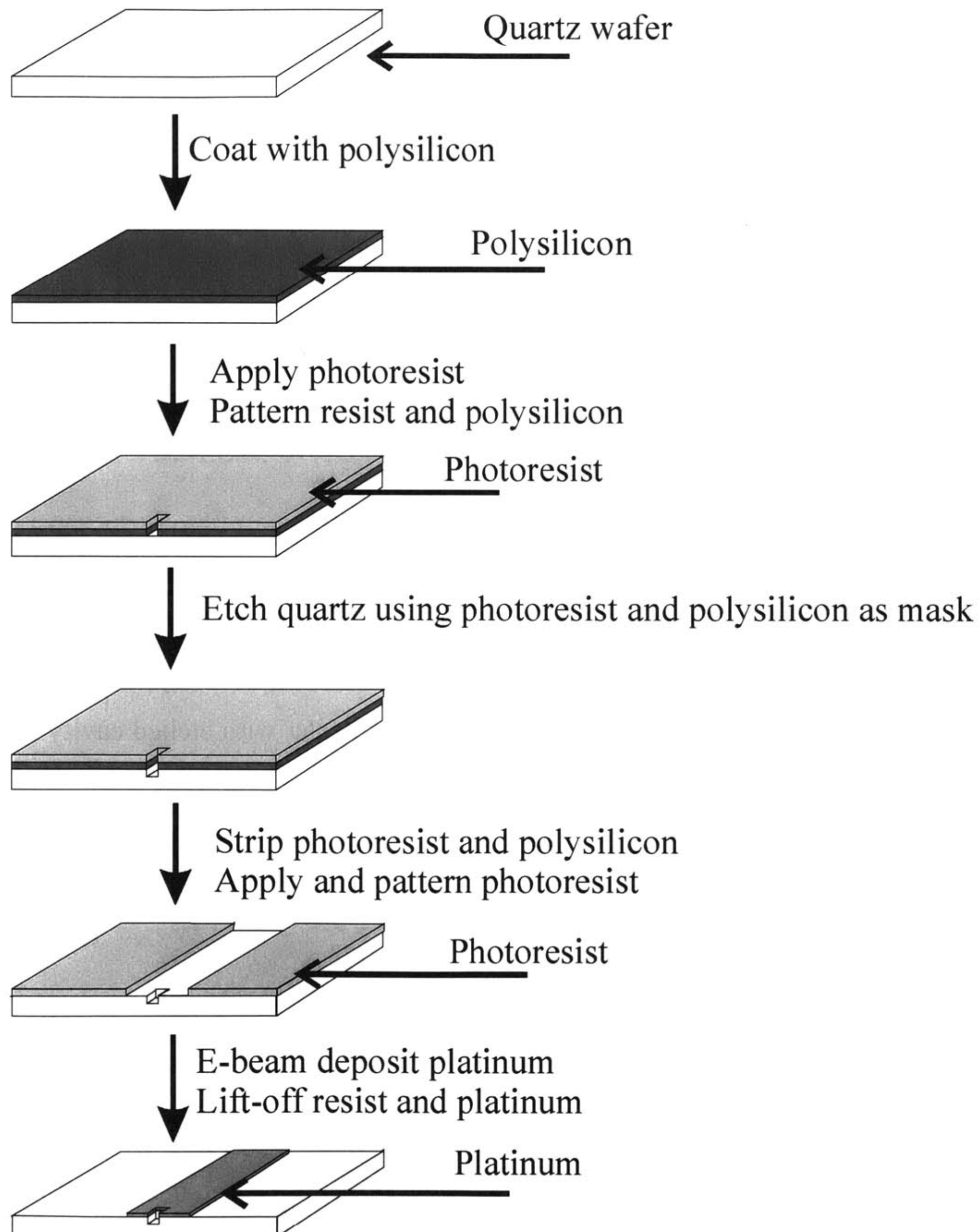

Figure 4-1 Fabrication process for quartz heater layer.

For the second generation resistive heaters, the cavities were etched on 6 inch diameter quartz wafers by a different process. The wafers were etched by Surface Technology Systems (STS) using a proprietary process in order to achieve good uniformity and depth. Cavities with a 5μm square opening were etched either 5μm or 15μm deep. The shallow cavities had a uniformity of 0.5μm across the wafer and the deep cavities had 0.7μm uniformity. Scanning electron micrographs (SEMs) of 10μm wide trenches etched by STS are shown in Figure 4-2. These wafers were used for the second generation resistor testing.

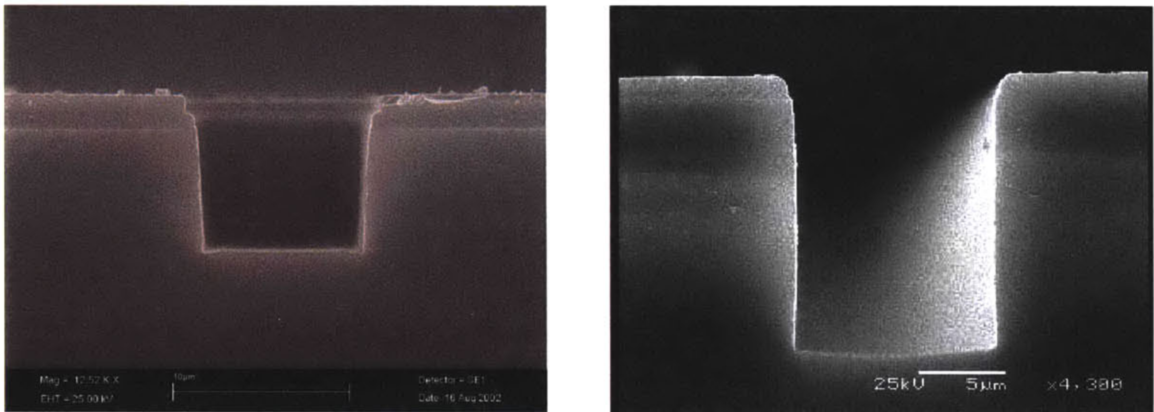

Figure 4-2 SEMs of 10μm wide trenches on quartz wafers etched by STS. On the left is the 5μm deep feature and on the right is the 15μm deep feature.

A micrograph of a completed second generation heater with etched cavity is shown in Figure 4-3.

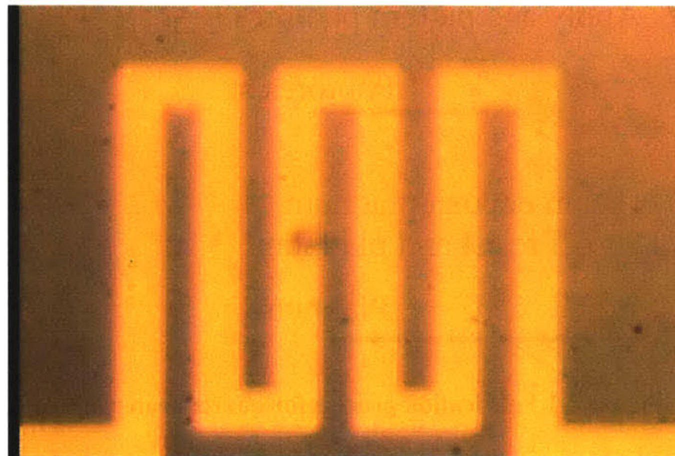

Figure 4-3 Micrograph of completed resistive heater with cavity.

4.2 Silicon Process

The bioparticle manipulation layer of the device is fabricated on a 4 inch diameter, 400μm thick, double-side-polished silicon wafer. The fabrication process for this layer is shown in Figure 4-4.

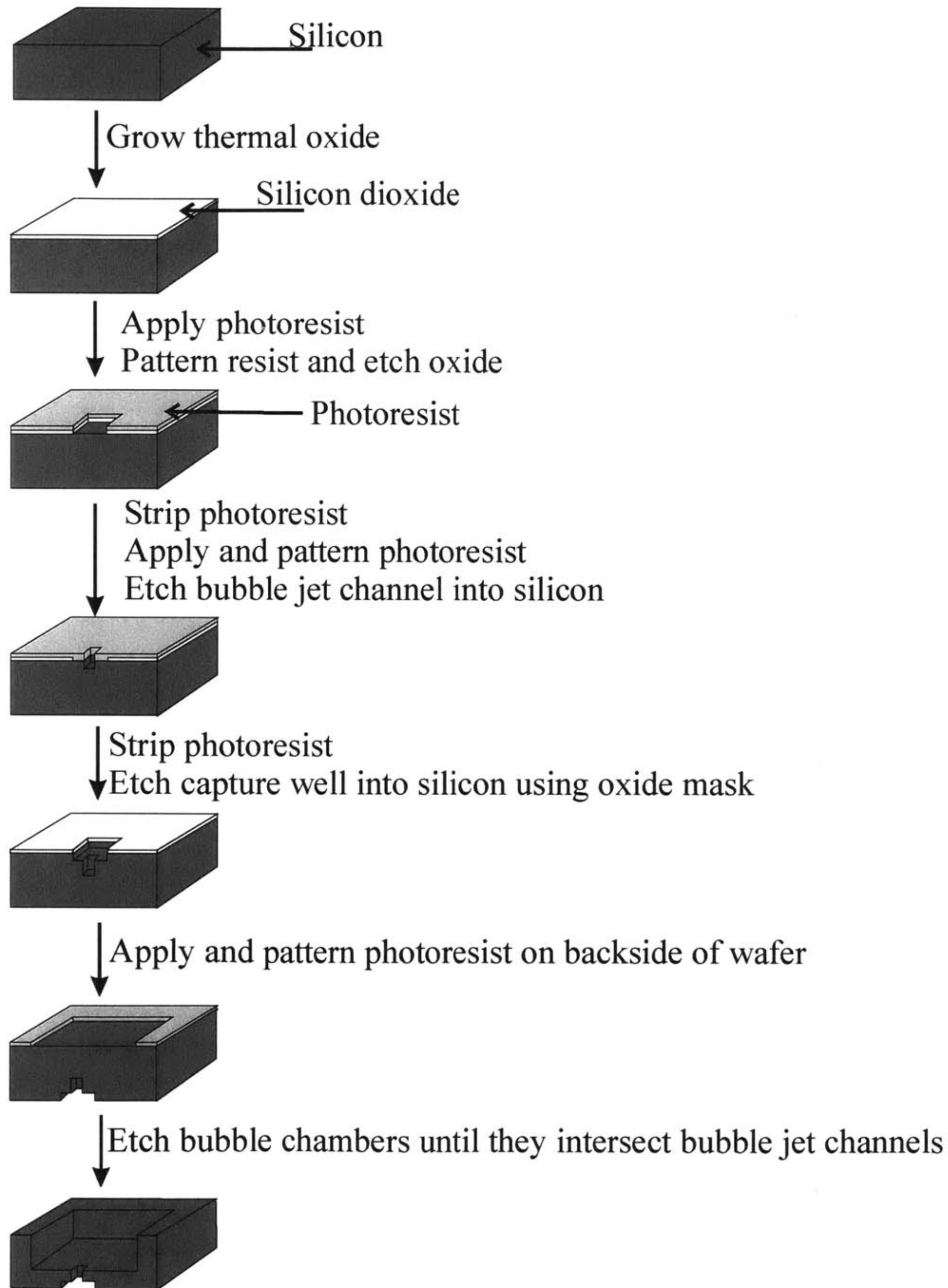

Figure 4-4 Silicon bioparticle manipulation layer fabrication process.

First, 1000Å of thermal oxide is grown on the silicon wafer in a tube furnace. Next, the top side of the wafer is patterned with standard photolithography to define the capture wells and the exposed oxide is etched using a buffered oxide etch. The resist is stripped and the top side of the wafer is patterned again using standard photolithography to define the narrow channel. Next, the silicon is etched using a deep RIE 80-100μm to create the bubble jet channel. At this point the resist is stripped and the oxide mask is used to etch the capture wells about 20μm, also using a deep RIE etch. The back side of the wafer is then patterned with thick photoresist (10μm) to define the bubble chambers, then the wafer is etched about 300-350μm until the chambers intersect the narrow channels defined from the front side of the wafer. A detailed process flow is in Appendix B. An SEM of the finished cell well is shown in Figure 4-5.

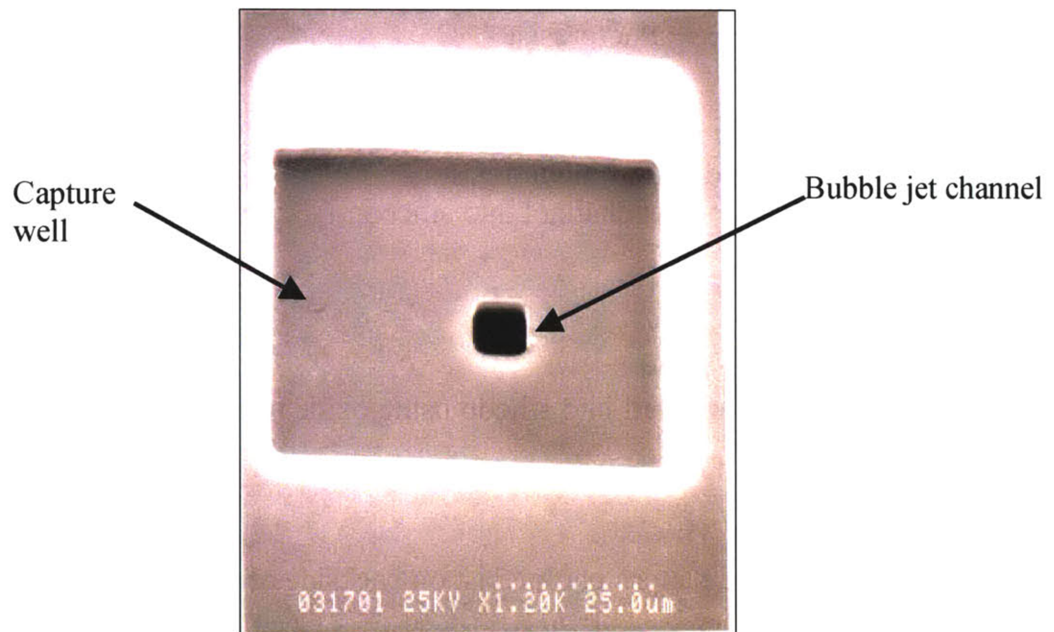

Figure 4-5 SEM of capture well and bubble jet channel on silicon layer.

4.3 Device Assembly

The microbubble actuator was manufactured by bonding the bottom quartz resistor heater to the top silicon bioparticle manipulation wafer. To do this, both the silicon and quartz wafers are first diced into chips using a diesaw. The quartz resistor

chips are drilled with the inlet, outlet, and back flow fluidic ports using a diamond drill bit 750μm in diameter. Next, the chips are coated with 1μm of CYTOP^{TM} as described above, then immediately afterwards, are bonded to the silicon device chips using an aluminum jig on top of a hotplate at 160°C. The chips are optically aligned and bonded in the jig with a 10kg weight on top for 2 hours, then cooled for another hour before removal from the jig[66]. The detailed process flow is in Appendix C.

5 EXPERIMENTAL METHODS

This chapter will describe the experimental methods used to test the resistive heaters and the full microbubble bioparticle actuator. Both the first generation line heaters and the second generation folded heaters were tested in order to characterize the dependence of bubble formation on nucleation cavities and surface coatings. Two different testing methods were used, one for all of the line heaters, and then a more sophisticated method was developed for the later testing of the folded heaters. The prototype of the actuator was also tested as a proof-of-concept system, and the method used will be described.

5.1 Sample Preparation for Resistor Testing

5.1.1 Calibration

The resistivity of the thin film platinum in the heaters increases with increasing temperature. This relationship was used in order to calculate the temperature of the resistive heater from the known voltage and current. The platinum resistors were calibrated in order to determine the temperature/resistance characteristic. The apparatus used to calibrate the resistors is shown in Figure 5-1.

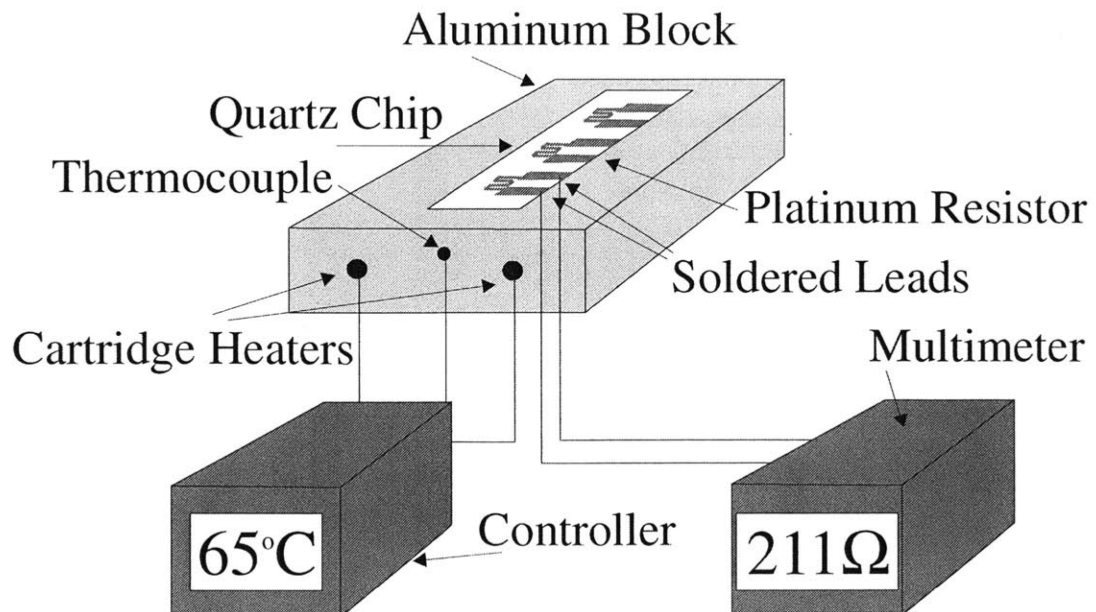

Figure 5-1 Apparatus used to calibrate resistors.

An aluminum block was machined with three cylindrical holes running the length of the block. A thermocouple was inserted into the center hole, and cartridge heaters were placed in the side holes. A depression was machined on top of the block into which a quartz chip with platinum resistive heaters could be positioned. All the leads from the heaters and thermocouple were connected to a temperature controller. The controller could be set to bring the aluminum block to a specified temperature using the cartridge heaters, and the thermocouple measured the actual temperature of the block. Wires were soldered onto the leads of one of the resistors and these were connected to a multimeter that measured the resistance across the heater. Some data was taken using a 4-point measurement, but there was no difference from the 2-point measurement, so for convenience the 2-oint measurement was used.

To calibrate the resistor, the room temperature resistance was first measured. After this, the block was slowly heated, and temperature and resistance measurements were collected at intervals. The data was normalized to the room temperature resistance and then plotted (Figure 5-2). A line was fit to the data, and the resulting equation was used to calibrate the temperature to the normalized resistance of the heater. This line is in close agreement with previous work [67]. For the resistors tested, Equation 5-1 was used to relate temperature to normalized resistance.

$$T = 443.8\frac{R}{R_o} - 425.4 \tag{5-1}$$

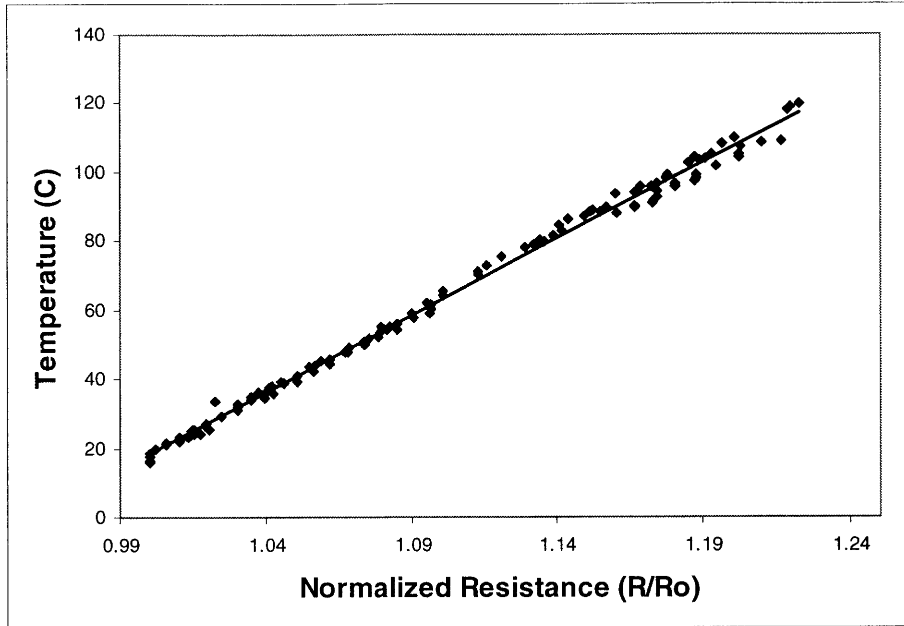

Figure 5-2 Plot of temperature versus normalized resistance used to calibrate resistors.

5.1.2 Water Preparation

Dissolved air in water can cause serious problems to bubble powered devices, since when a vapor bubble is formed this air can come out of solution into the bubble, and remain as a residual bubble once the heat is turned off. Residual air bubbles take a long time (more than an hour) to dissipate and can clog a microfluidic system. As the temperature of water is increased, the solubility of air in water decreases. This principle was used in order to remove dissolved air from the water. For the purposes of testing, deionized water was boiled in a beaker on a hotplate prior to being used for bubble formation. By boiling the water, much of the dissolved air was removed from the fluid, greatly decreasing bubble collapse time. This will be discussed further in the next chapter.

5.2 First Generation Testing

The line resistors were tested using a probe station and a semiconductor parameter analyzer to ramp up the voltage while measuring the current in the resistor. As the current flowing through the resistors increases, they heat up due to ohmic heating. Additionally, as characterized above, the resistance of the resistors increases with temperature. Consequently, the I-V curves were not straight lines, since the resistance is

not constant with temperature, and the inverse slope of the curve is equal to the resistance. As the resistor gets hotter, the slope of the I-V curve changes more quickly. A discontinuity is observed on the I-V curve when a bubble formed, and this is used to identify the time of bubble formation. An example of a typical I-V curve generated using this method is shown in Figure 5-3. The resistance of the heater at each time step is computed from the I-V curve, then the average resistor temperature associated with each resistance is calculated using the heater calibration. The plot of heater temperature as a function of the ramped voltage that was generated using the data in the I-V curve is shown in Figure 5-4.

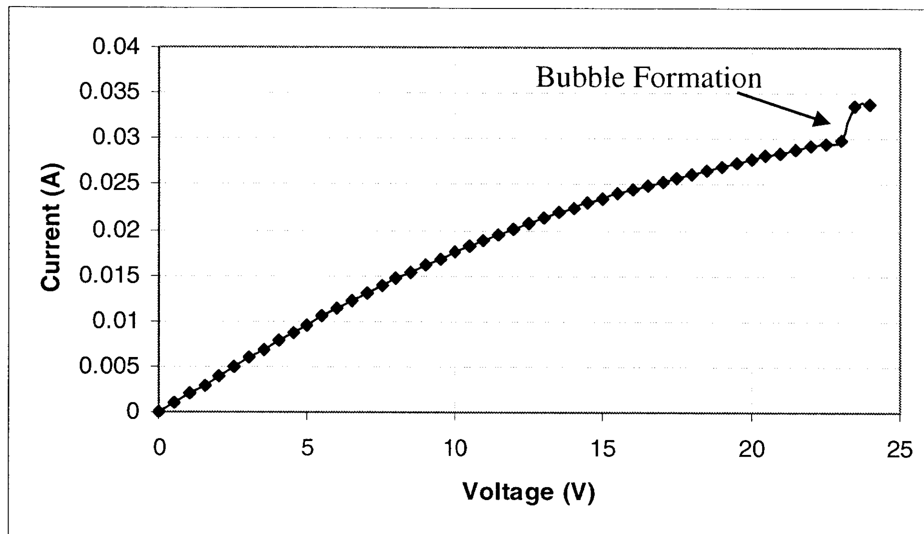

Figure 5-3 A typical I-V curve generating in the testing of a line heater with ramped voltage and measured current. The discontinuity is the point of bubble formation.

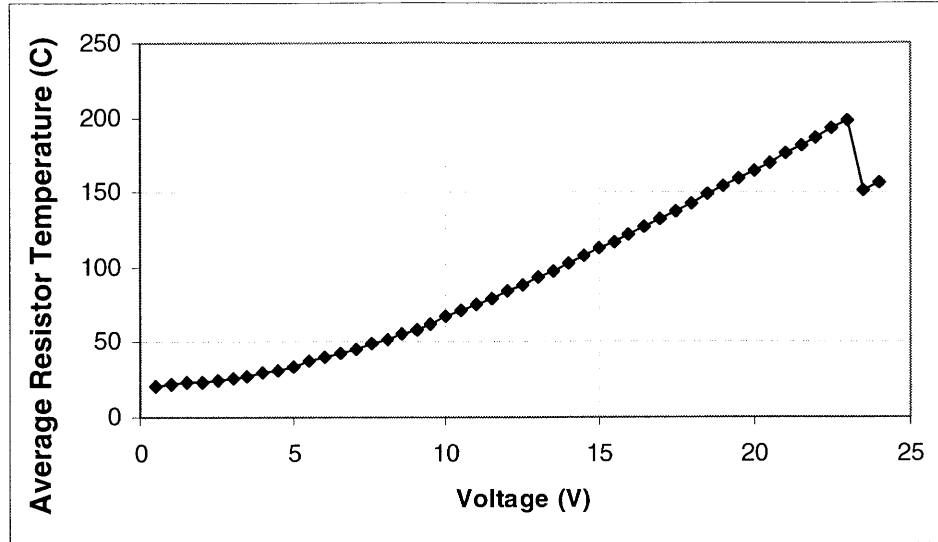

Figure 5-4 The heater temperature curve generated using the I-V curve shown in Figure 5-3.

Line resistor wafers were fabricated with and without bubble nucleation cavities and then some of them were coated with CYTOP™ or silanized, using the method described in the previous chapter. The cavities are approximately 6μm square and 20μm deep. Testing was carried out using a thin layer of deionized water that had been degassed just prior to testing by the method described above. A glass cover slip was placed over several drops of this water during testing, in order to prevent evaporation. The platinum resistors had resistances ranging from 70-300 ohms. Voltage was ramped up in one half volt increments, every 8 milliseconds until a bubble was formed, and then immediately turned off. Maximum voltages ranged from 3-15 volts. For some measurements the bubble formation was video taped so that the maximum bubble diameter, and bubble dissipation time could be measured.

An experiment was run to determine the effect of having cavities in resistive heaters, as well as the effect of the different surface treatments. To this end, resistor wafers were prepared six different ways: bare quartz with no cavities, bare quartz with cavities, silanized quartz with no cavities, silanized quartz with cavities, CYTOP™ -coated quartz with no cavities, and CYTOP™ -coated quartz with cavities. Testing was carried out as described above. One measurement of each of twenty-four resistors was taken on each wafer, using the same de-gassed water for all of the testing on each wafer.

Statistical analysis of this data was performed using ANOVA, to confirm that the changes in bubble formation temperature were statistically significant.

For biological applications, it is essential that aqueous fluid, preferably saline, be used in the full device, imposing a requirement that the resistor surface be passivated to prevent the electrolytic breakdown of water. Therefore, because CYTOP™ passivates the resistor surface while silanization does not, we explored more vigorously during the first generation testing, the repeatability among chips and across trials for CYTOP™ – coated surfaces with etched cavities. For this testing, folded resistors were used that were 16μm wide and ranged in length from 500-200μm. The cavities in these heaters were 6μm wide and 4μm deep. 44 apparent bubble formation temperature measurements were collected from 44 resistors on each of five different trials, in order to determine the repeatability of apparent bubble formation temperature for CYTOP™ –coated resistors. Bubble collapse time and maximum bubble diameter was also measured for one of these trials. The second generation testing explores further the bubble formation repeatability and collapse time for silanized resistive heaters.

5.3 Second Generation Testing Method

5.3.1 Test Apparatus

The folded resistors were tested using a probe station and a National Instruments data acquisition card (DAC) that was controlled by a LABVIEW program. The program was designed to apply a voltage pulse for a defined period of time, and measure the resulting current through the resistor. As before, from these measurements, the average resistor temperature could be calculated from the temperature/resistance calibration.

The schematic of the test apparatus used is shown in Figure 5-5. The DAC supplies a 5 volt digital pulse for a specified time (usually 10-50 milliseconds) to the MOSFET, which turns on the system. When on, a constant voltage is supplied by the voltage source to the resistive heater. The DAC measures V1, V2, and V3 during the pulse time, and this data may be used to calculate the current through the heater. Knowing the voltage and current yields the resistance, which is then used to calculate the temperature of the heater at each time step. The DAC was programmed to take 4000 measurements per second, allowing a 0.25 millisecond time step between measurements.

This testing method has many advantages over the first generation testing method. First, the LABVIEW program is capable of delivering a voltage pulse, where the parameter analyzer could only ramp the voltage. In the old testing method, the smallest possible time step was approximately 8 milliseconds, instead of the current 0.25 milliseconds that allows much better resolution. Using the new testing method, it is possible to deliver a voltage pulse of a magnitude and duration determined by the user, to achieve more precise measurements.

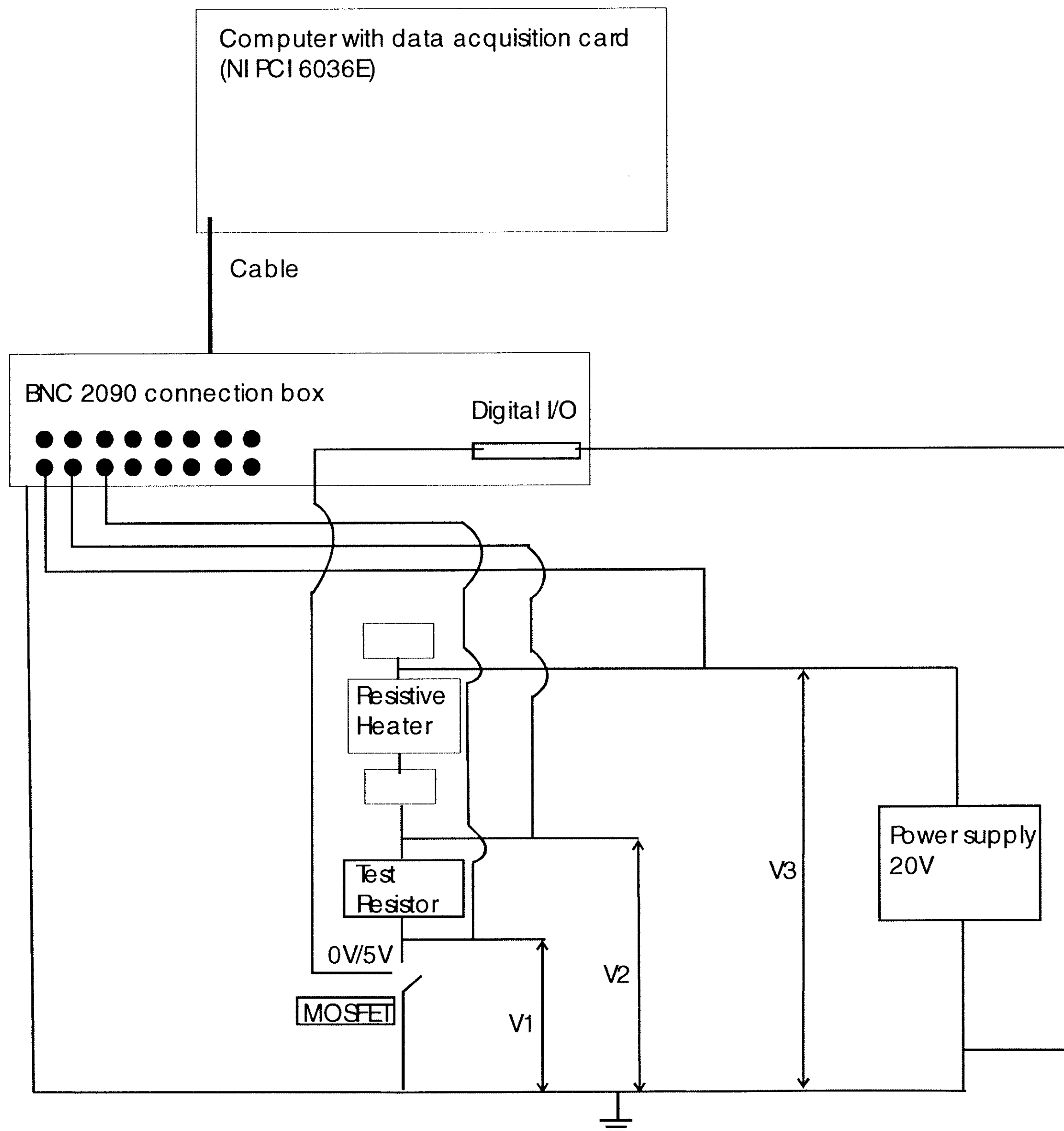

Figure 5-5 Schematic of test apparatus for second generation testing.

In addition, the bubble formation was video taped using a camcorder attached to the probe stand that was output to a computer. The video data could be investigated frame by frame for measurements of the bubble diameter.

5.3.2 *Repeatability of Resistor Heating*

In order to confirm that the test apparatus behaves repeatably, a silanized folded resistor was heated many times with identical voltage pulses, lower than needed to form bubbles. The 650μm long, 16μm wide folded resistor received a 4 volt pulse that was 50 milliseconds long. Ten trials were completed, and the heater temperature was plotted as a function of time for each run. The standard deviation of heater temperature for each time step between runs was also calculated.

5.3.3 *Bubble Formation Temperature*

Testing was performed in order to determine how cavity position and depth affects the apparent bubble formation temperature. The folded resistors tested were silanized using the method described previously, and have cavities either in the central region or at the edge of the heated region. Additionally, resistors with cavity depths of either 5μm or 15μm were tested. Silanized folded resistors without cavities were tested, as well as untreated, unetched resistors that were used as a control. The resistors tested are shown in Figure 5-6. All of the resistors tested are the same size. The lines are 13μm wide and 650μm long, with cavities that are 5μm square. The resistors tested are described in Table 5-1.

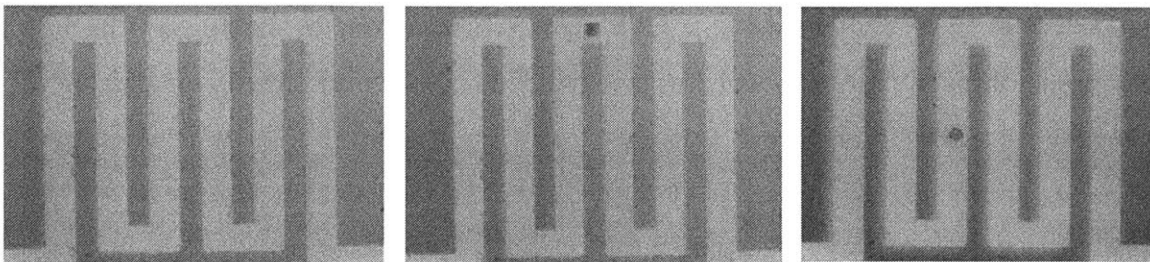

Figure 5-6 The three resistor configurations tested. On the left is a resistor with no cavity. In the center is a resistor with a cavity on the edge of the heated field. On the right is a resistor with a cavity in the center of the heated field.

Test #	**1**	**2**	**3**	**4**	**5**	**6**
Cavity Location	NA	NA	Center	Center	Edge	Edge
Cavity Depth	0	0	5μm	15μm	5μm	15μm
Surface Treatment	None	Silanized	Silanized	Silanized	Silanized	Silanized

Table 5-1 Resistor characteristics for bubble formation temperature testing.

For each folded resistor tested, freshly boiled DI water was used under a glass cover slip. Twenty measurements were taken for each resistor, and ten resistors were tested on each chip, so each test listed in the table below is comprised of 200 measurements. The same water was never used for two resistors to avoid excessive dissolved air uptake.

For each test set, the same voltage pulse was applied. The LABVIEW program was used to apply a voltage pulse to the resistor while measuring the resulting current and calculating the temperature of the heater for each time point. The etched samples received an applied voltage of 6.6V for 50ms, and the unetched samples received an applied voltage of 8.2V for 50ms. All of the measured data was saved so that the apparent bubble formation temperature could later be determined from a discontinuity in the temperature versus time plot. An example of a typical heating curve with the discontinuity where a bubble was formed is shown in Figure 5-7.

Each point on this plot is the average heater temperature at the given time. Hence, the actual heater temperature at any given point on the heater may be higher or lower than the measured average heater temperature and can be estimated using the finite difference heat transfer model presented in Chapter 2. The average heater temperature for each time step is computed by the LABVIEW program from the measured voltage and current through the heater which is converted to resistance and finally temperature using the resistor calibration.

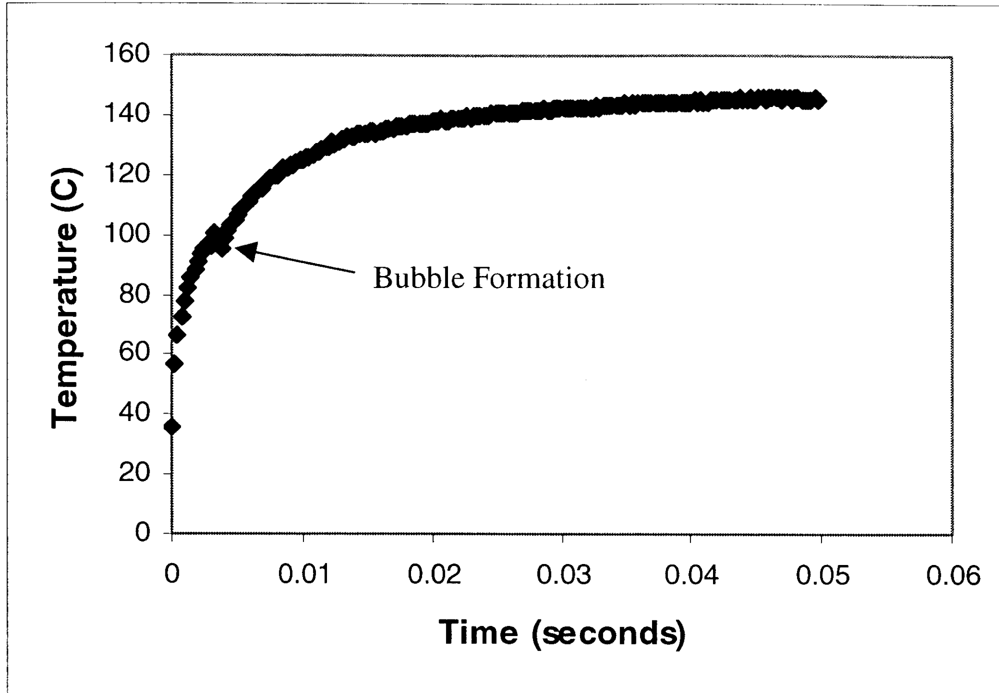

Figure 5-7 Heating curve for a folded resistor tested using the LABVIEW program. The discontinuity represents the point of bubble formation.

During testing, each resistor was video taped in order to record the maximum bubble size and the location of bubble formation. This bubble diameter was measured from the captured video frame with a ruler. The bubble collapse time was measured as well, using a stopwatch.

As a comparison, a resistor with a shallower cavity was also tested. The resistor was 16μm wide, and 650μm long with a centrally located 6μm square cavity that was 4μm deep. Twenty successive measurements were taken using a 7 volt pulse that was 50ms long.

5.3.4 Energy Dependence of Bubble Size

Further testing was performed on a single silanized folded resistor with a central 15μm deep cavity. For this testing, voltage pulses of varying magnitude and time were applied in order to explore the effect of total energy supplied to the heater on maximum bubble size and bubble collapse time. The resistor was tested as described above, with new freshly boiled deionized water for each different voltage magnitude. Three voltage levels were applied to the heater: V=7V, V=8V, and V=9.5V. For each voltage level,

four different pulse times were used in order to make four different total energies applied to the heater. The testing parameters are shown in Table 5-2. Each test is comprised of ten runs, during which the maximum bubble size and bubble collapse time are measured as described above. The energy was calculated by multiplying the voltage across the resistor by the current through it for each time step, and then multiplying by the time step and summing for every time step.

Test #	**1**	**2**	**3**	**4**	**5**	**6**	**7**	**8**	**9**	**10**	**11**	**12**
Voltage (V)	7	8	9.5	7	8	9.5	7	8	9.5	7	8	9.5
Time (msec)	10	7.5	5.5	20	15	11	40	30	22	80	60	44
Total Energy (mJ)	5	5	5	10	10	10	20	20	20	40	40	40

Table 5-2 Testing parameters for bubble diameter/collapse time testing

5.3.5 Bubble Dynamics

Because the majority of the testing was completed using relatively short pulse times (t<100ms), the dynamics of bubble growth were also investigated for longer times. For this experiment, a silanized folded heater with a 4µm deep, 6µm square cavity was tested with voltage pulses of various times. The heater was 16µm wide and 1270µm long. The parameters for the tests are shown in Table 5-3. During each test, the bubble formation was captured by video, and the bubble diameter was measured in each frame, in order to monitor bubble size as a function of heating time and temperature. By monitoring the bubble growth, we were also able to observe the direction of bubble growth and the interactions between multiple bubbles growing together on the heater. Plots were generated of the heater temperature as a function of time, as well as the bubble diameter as a function of time.

Test #	**Voltage Applied**	**Pulse Time**
1	9.5	40 ms
2	9.5	80 ms
3	9.5	160 ms

4	9.5	320 ms
5	9.5	640 ms
6	9.5	1280 ms
7	9.5	2000 ms

Table 5-3 Test parameters for bubble dynamics testing.

5.3.6 Cycling

Testing was carried out in order to determine whether the bubble formation on a heater became more repeatable after bubbles had been formed on the heater several times in a row, or the heater has been 'cycled'. Initial testing was carried out on a silanized folded heater with a central cavity 6μm in diameter and 4μm deep. The heater was 16μm wide and 1270μm long. A 9.5 volt pulse, 50 milliseconds long, was applied to the heater and a bubble was formed. Once the bubble had collapsed completely, an identical pulse was applied to the heater. This was completed a total of 14 times, using the same preboiled deionized water. This data was compared to the data collected using the heaters with 5μm and 15μm deep central cavities described in Section 5.3.3.

5.4 Full Device Testing

To test the full device, it was first vacuum-filled with 0.05% Triton X-100 surfactant solution [68]. To vacuum-fill the device, it is submerged in a beaker of the solution, which is then placed in a bell jar that is evacuated by a vacuum pump for several minutes. It is then slowly vented to atmospheric pressure. At this point the chip is placed in the flow chamber for testing. A surfactant solution is used in order to prevent bioparticles from sticking to the device surfaces. A solution of 10μm diameter polystyrene beads flows over the top of the device, using a syringe pump (KD Scientific KDS200, New Hope, PA). Electrical contact is made using probes on a probe station, and bubbles are formed in the bubble chamber using the first generation testing method described above. The operation of the device is captured using a video camera fed into a computer, as with the bubble testing described above.

6 RESULTS

6.1 General Effect of Cavities on Bubble Formation (Using the First Generation Testing Method)

For the line resistors with patterned 6μm square nucleation sites, bubbles formed exclusively in the cavities on almost every trial with the two hydrophobic surface preparations, but almost never formed exclusively in cavities on the bare quartz. Figure 6-1 shows bubble formation in a microcavity for a hydrophobic preparation. Specifically, bubbles formed only in cavities for wafers with hydrophobic surface treatments in 47 out of 48 measurements, whereas bubbles formed only in cavities for uncoated wafers in 1 out of 24 measurements.

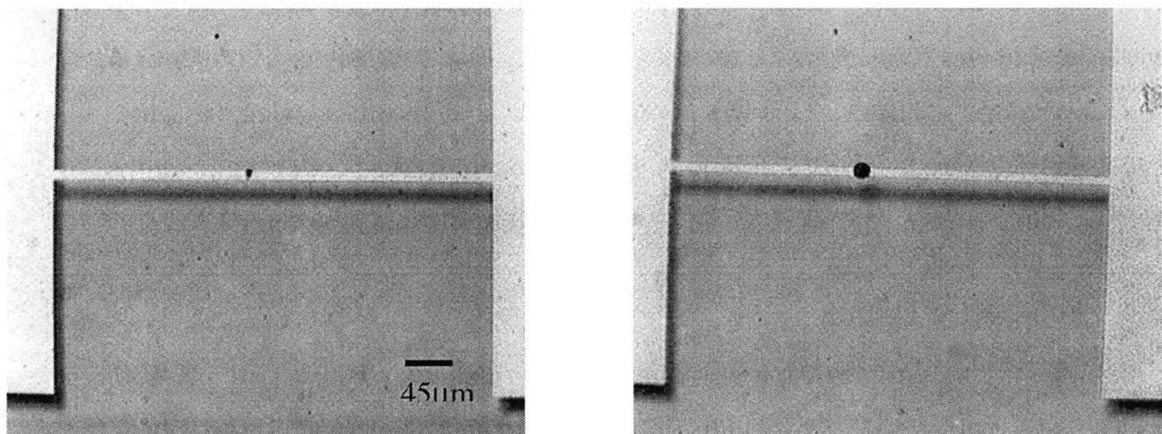

Figure 6-1 A CYTOP-coated platinum line heater with a cavity. Left: Resistor submerged in water with no voltage applied. The microcavity appears as a dark spot. Right: After a voltage is applied, a bubble forms in the microcavity.

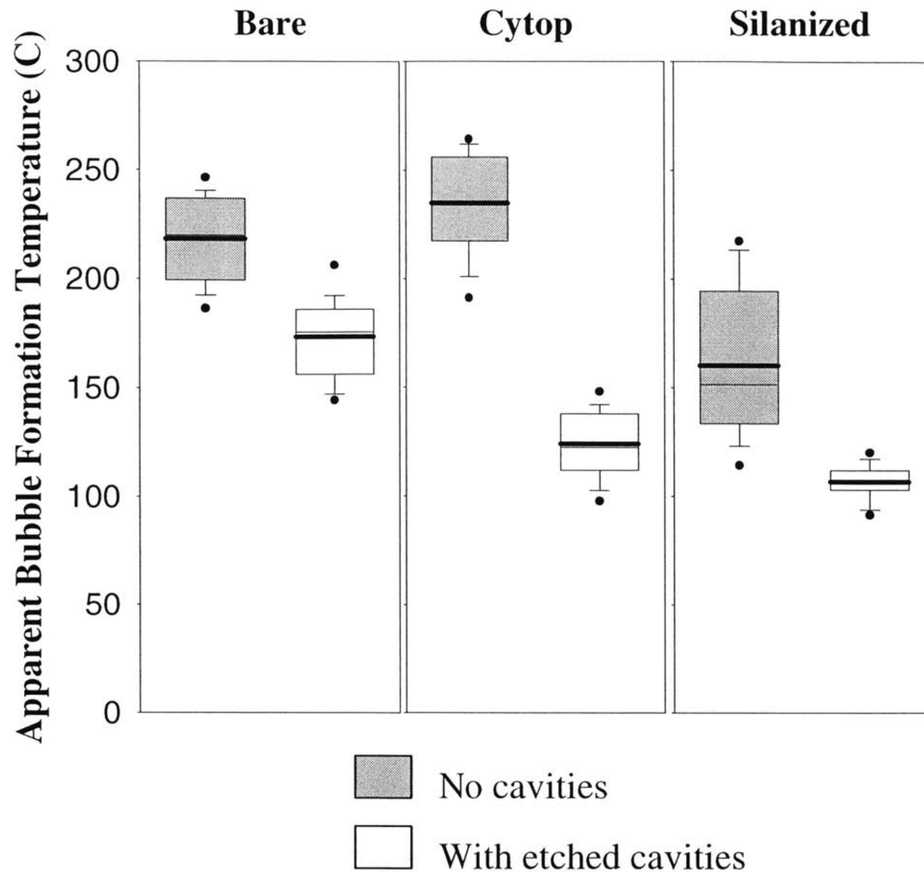

Figure 6-2 Resistor temperatures at bubble formation for the six conditions: bare resistor wafers with and without etched cavities, CYTOP™ -coated wafers with and without etched cavities, and silanized resistor wafers with and without cavities. The boxes represent the 25th through 75th percentiles of data. The lines span the 5th through 25th and 75th through 95th percentiles of the data and the points represent outlying data. Lines in the boxes represent mean (thick line) and median (thin line) data. P<0.001 between all data sets shown.

The apparent bubble formation temperature depends on both the presence of cavities and on the surface properties, as shown in Figure 6-2. There are two trends that can be observed. First, irrespective of surface treatment, apparent bubble formation temperature is lower for resistors with cavities than without cavities ($P=1.88 \times 10^{-10}$ for uncoated wafers, $P=1.73 \times 10^{-23}$ for CYTOP™-coated wafers, $P=1.86 \times 10^{-9}$ for silanized wafers). Second, for the wafers with cavities, those that have hydrophobic surface coatings had the lowest apparent temperature of bubble formation.

For the repeatability testing of the CYTOP™-coated wafers, the average resistor temperature at bubble formation for 44 independent resistors in five trials was 136°C, and the standard deviation was 22°C. This data is shown in Figure 6-3.

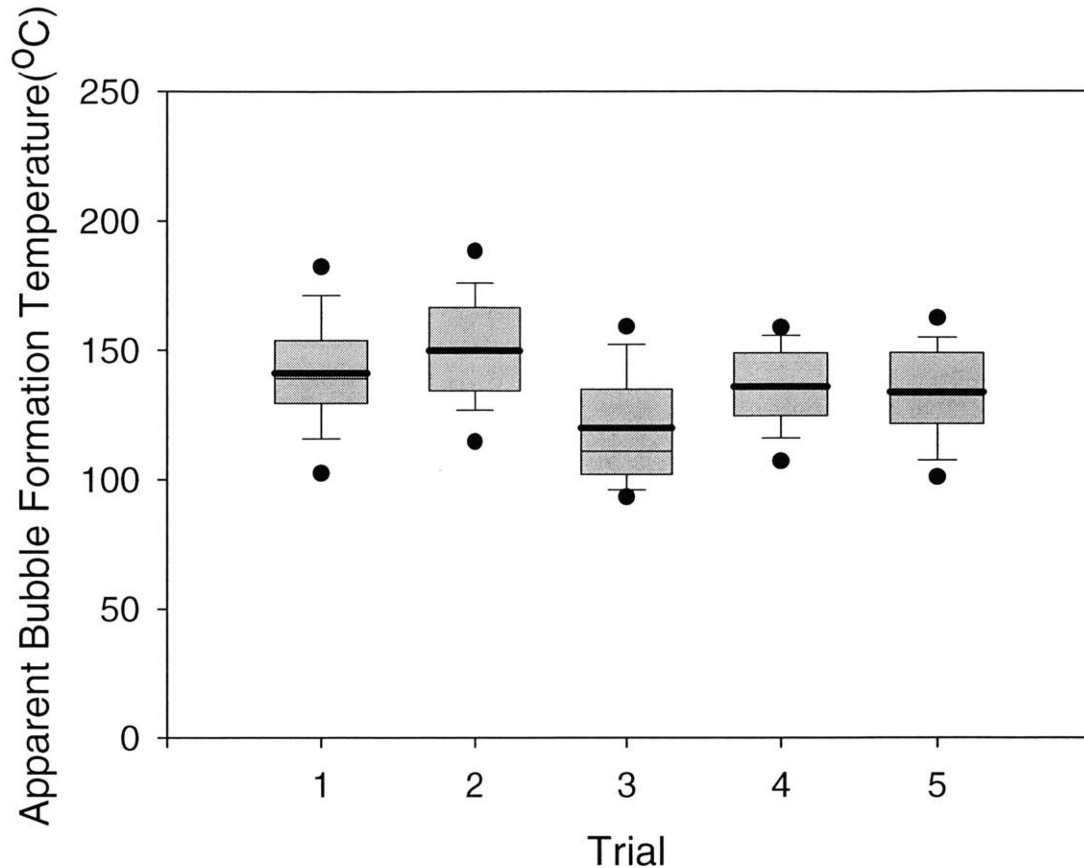

Figure 6-3 Repeatability of resistor temperature at bubble formation. Forty four CYTOP^{TM}-coated resistors, each with one cavity, were used for each of 5 independent trials. The boxes represent the 25th through 75th percentiles of data. The lines span the 5th through 25th and 75th through 95th percentiles of the data and the points represent outlying data. Lines in the boxes represent mean (thick line) and median (thin line) data.

With regards to bubble dissipation, all bubbles formed by the experimental protocol on CYTOP^{TM}-coated wafers dissipated in less than 20 seconds. Bubbles with larger initial diameters dissipated more slowly than smaller bubbles (Figure 6-4).

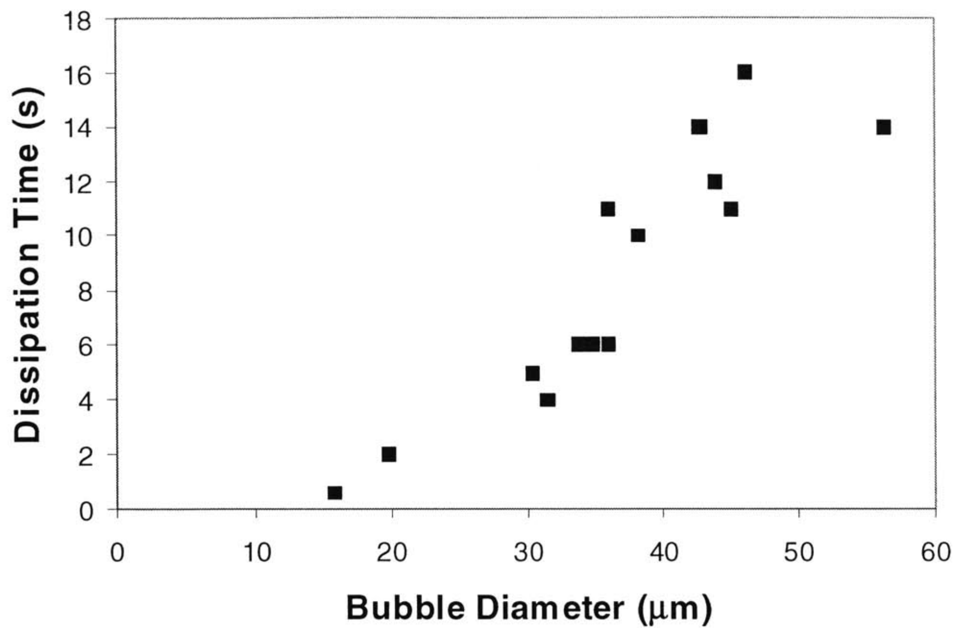

Figure 6-4 Bubble collapse time as a function of maximum bubble size for CYTOP™-coated resistors. The dissipation time increases as the initial bubble diameter increases.

6.2 Second Generation Resistor Testing

6.2.1 Repeatability of Resistor Heating

A folded resistive heater was heated to a level below bubble formation ten times in order to explore the repeatability of resistor heating. The plot of heater temperature as a function of time resulting from this testing is shown in Figure 6-5. The average percentage standard deviation between runs was computed to be 0.34%

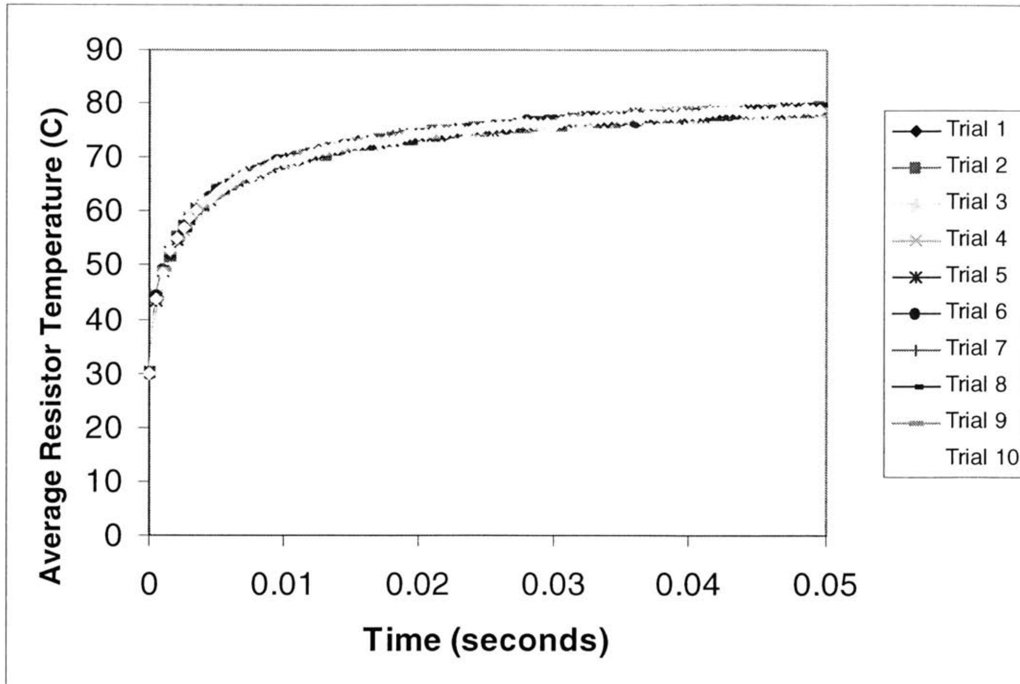

Figure 6-5 Plot of average heater temperature versus time for a 4 volt, 50ms pulse.

6.2.2 Bubble Formation Location

Figure 6-6 shows a folded resistive heater with a central cavity before and after bubble formation. For tests 3 and 4 (the 5μm and 15μm deep centrally located cavities), bubbles formed exclusively in the cavities for every measurement(100% of the trials), as shown in the figure. For the resistors with 5μm deep cavities at the edge of the heated field (Test 5), single bubbles formed in the cavities 65% of the time. For the resistors with 15μm deep cavities at the edge of the heated field (Test 6), single bubbles formed in the cavities 43% of the time. However, these percentages could be different since the frame rate is 30 frames per second, and the captured frames possibly miss whether the bubble forms in the cavity some of the time. In Tests 1 and 2 (no cavities, bare wafer and silanized wafer), The bubbles formed in random locations, generally in the central portion of the resistor. For the silanized resistors with no cavities (Test 2), multiple bubbles formed on the resistor 37% of the time.

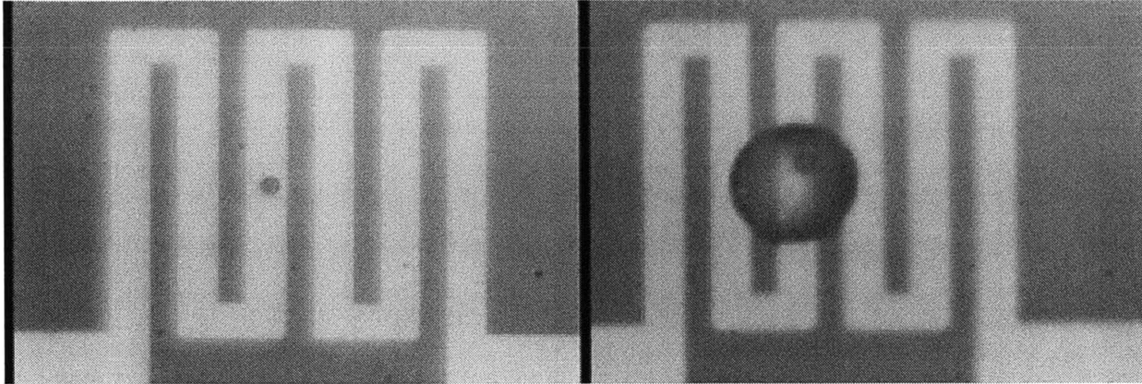

Figure 6-6 Folded heater with etched cavity. Left: Resistor submerged in water with no voltage applied. Right: After a voltage is applied, a bubble forms in the microcavity.

6.2.3 Bubble Formation Temperature

The average apparent bubble formation temperature and standard deviation for each set of tests is shown in Table 6-1. This data has also been plotted on a box plot (Figure 6-7).

Test	Average Apparent Bubble Formation Temperature (C)	Standard Deviation (C)	Percent of Trials where Bubble Forms in Cavity
1. Unetched, unsilanized	158.0	10.1	No cavities
2. Unetched, silanized	116.3	14.9	No cavities
3. 5μm depth, central cavities	106.7	9.0	100%
4. 15μm depth, central cavities	96.3	6.2	100%
5. 5μm depth, edge cavities	119.1	11.3	65%
6. 15μm depth, edge cavities	112.8	8.2	43%

Table 6-1 Average apparent bubble formation temperature and standard deviation for each test set.

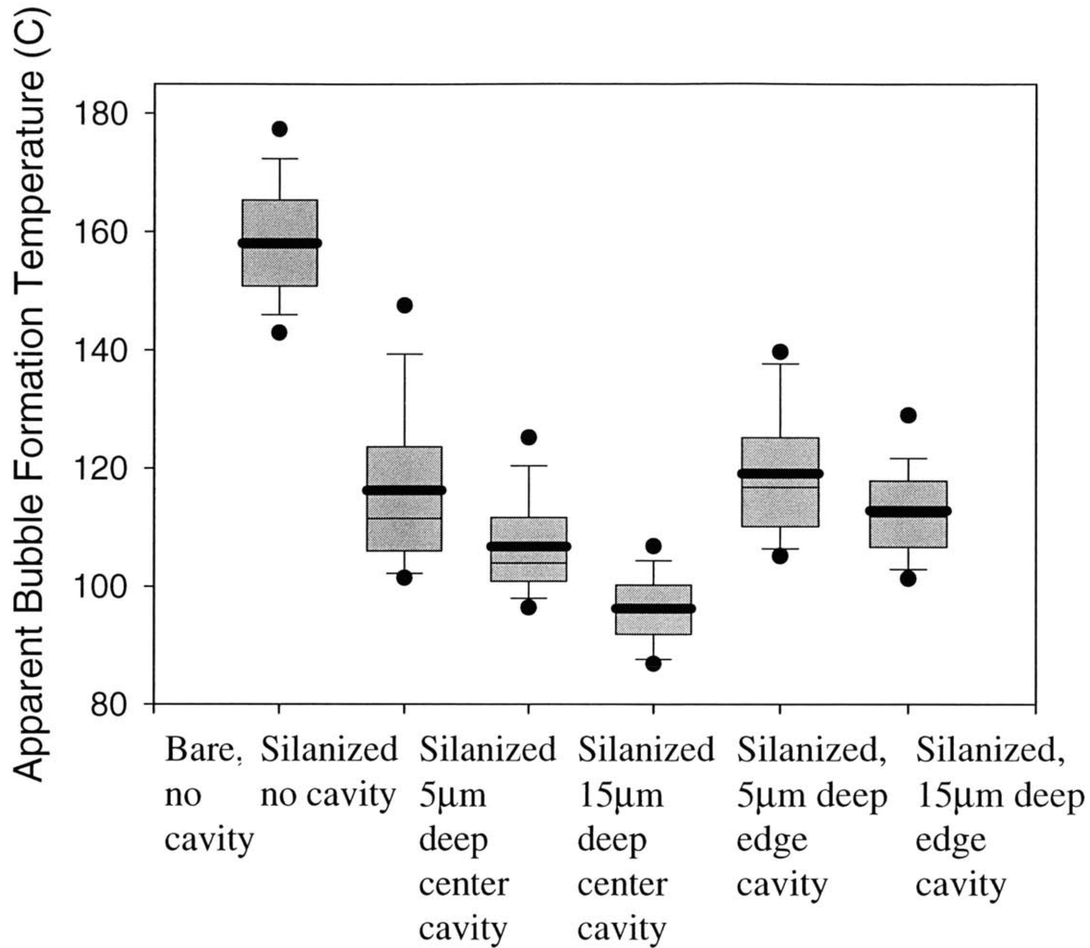

Figure 6-7 Apparent bubble formation temperatures for silanized folded resistors. Each test is comprised of 200 data points from 10 identical resistors. The lines span the 5th through 25th and 75th through 95th percentiles of the data and the points represent outlying data. Lines in the boxes represent mean (thick line) and median (thin line) data.

The results of the testing of the resistor with the 6μm wide 4μm deep central cavity are shown compared with the results from above of the resistors with 5μm wide, 5μm and 15μm deep cavities in Figure 6-8. The apparent bubble formation temperature decreases as the cavity depth increases, and the standard deviation of the data decreases as well as cavity depth increases.

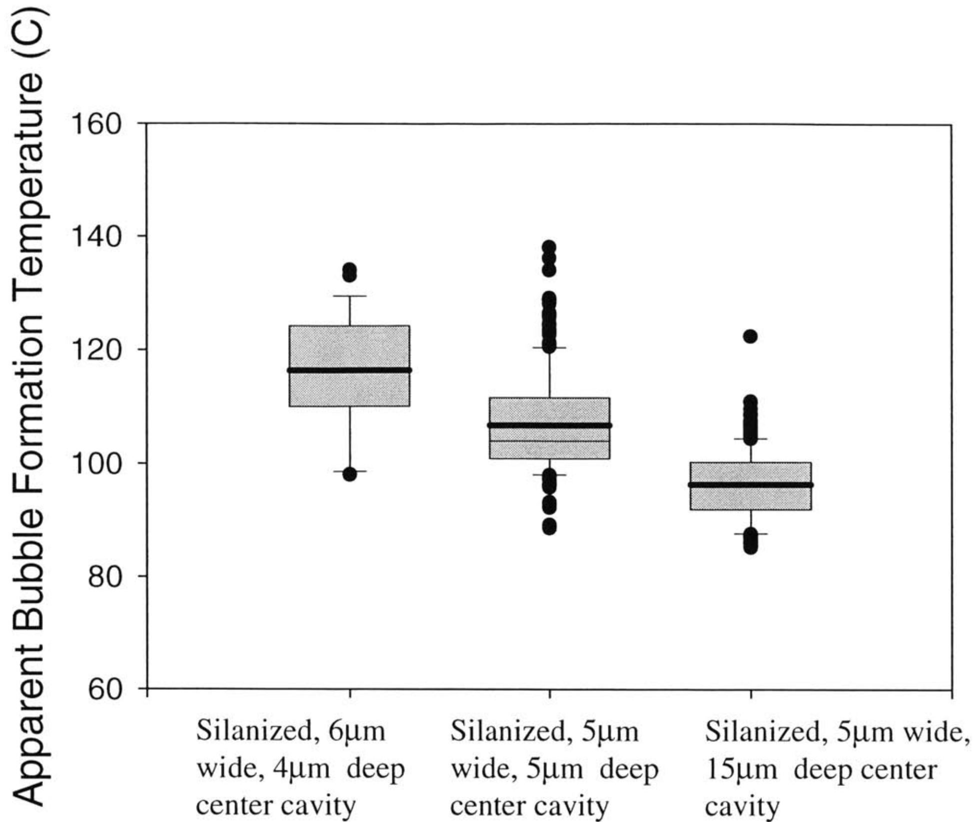

Figure 6-8 Apparent bubble formation temperatures for silanized folded resistors with central cavities. The results from the resistor with a 6μm wide, 4μm deep cavity are comprised of 20 data points, the other two tests are comprised of 200 data points. The lines span the 5th through 25th and 75th through 95th percentiles of the data and the points represent outlying data. Lines in the boxes represent mean (thick line) and median (thin line) data.

6.2.4 Bubble Collapse Time

For the bubble formation temperature testing and the bubble formation energy testing of the resistors with 15μm deep cavities, the maximum bubble diameter was plotted as a function of bubble dissipation time (Figure 6-9). A second-order polynomial curve was fit to the data, since theory predicts that bubble collapse time is proportional to the square of the bubble diameter. The uncertainty in the measurement of the bubble diameter is ∀2μm due to the fact that it was manually measured with a ruler and 1mm≅1μm. The uncertainty in the time measurement is ∀1 second due to the fact that it was measured with a stopwatch.

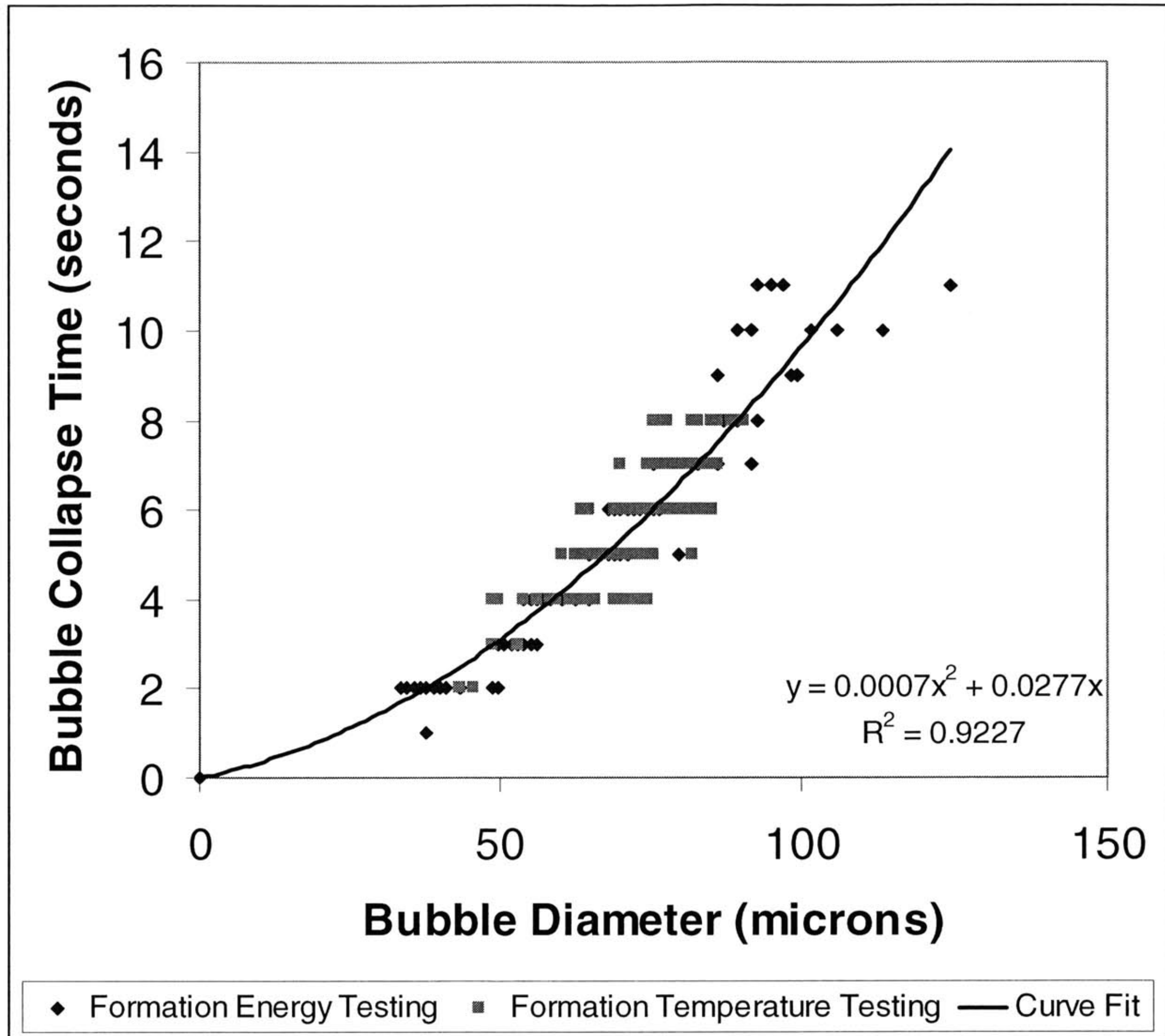

Figure 6-9 Plot of bubble collapse time versus initial bubble diameter for the testing of the folded resistors with 5μm wide, 15μm deep cavities. Bubble collapse time data collected during the bubble formation temperature testing and the bubble energy testing are both plotted.

6.2.5 Energy Dependence of Bubble Size

The results of the testing performed by applying voltage pulses of varying magnitudes and times to a silanized folded heater and then measuring the resulting bubble size are shown in Table 6-2.

Test #	1	2	3	4	5	6	7	8	9	10	11	12
Voltage (V)	7	8	9.5	7	8	9.5	7	8	9.5	7	8	9.5

Time (msec)	10	7.5	5.5	20	15	11	40	30	22	80	60	44
Total Energy (mJ)	5	5	5	10	10	10	20	20	20	40	40	40
Average Diameter Bubble (μm)	37	36	37	54	54	48	74	71	59	90	98	71
Standard Deviation	1.4	1.3	0.9	2.1	1.0	4.0	3.2	2.5	4.7	12	11	3.5

Table 6-2 Results of bubble size/energy testing.

These results are shown in Figure 6-10. Two trends can be observed. First, we can see a dependence of bubble size on the energy applied to the heater, for the most part regardless of the voltage level and pulse time. Data from the highest voltage (9.5 volts) and the two highest energy levels, however, have bubble diameters somewhat smaller that the other tests with the same energy levels, but the trend remains the same. Second, we can see that the range of resultant bubble diameters increases with increasing pulse time. Lines have been fit to the data from each voltage level.

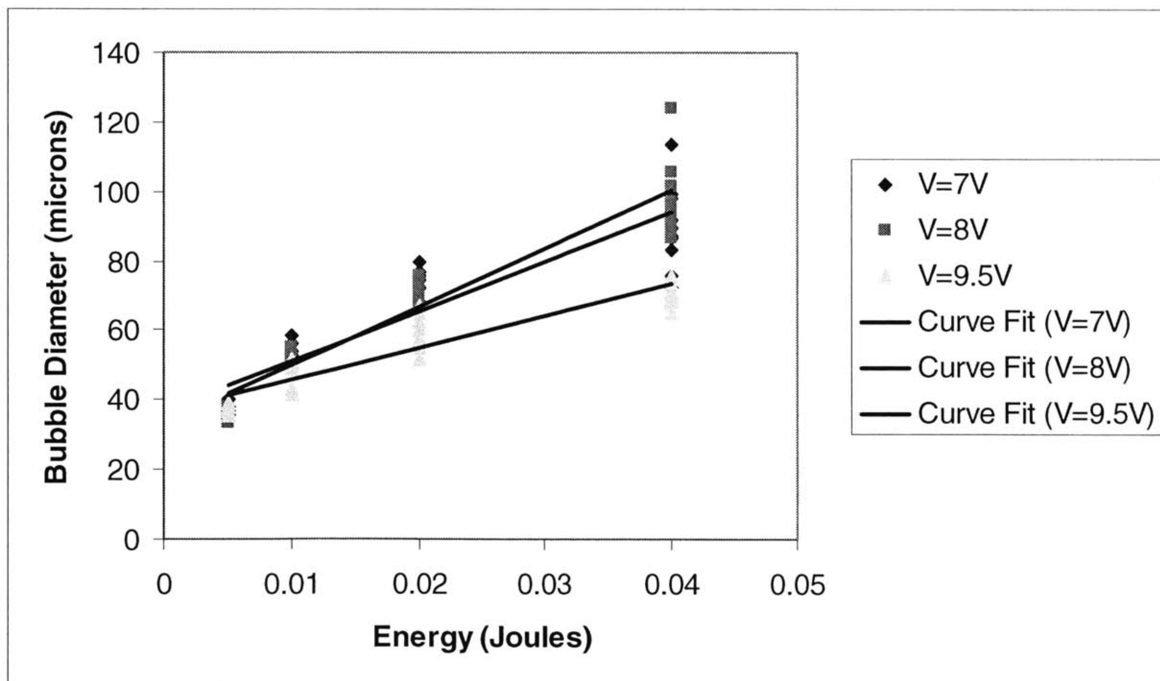

Figure 6-10 Plot of bubble diameter versus total energy applied to the heater.

6.2.6 *Bubble Dynamics*

The results of the testing with long pulse times are shown in the following figures. For pulse times of t=40ms (Figure 6-11) and t=80ms (Figure 6-12), no bubble diameter plots were generated because not enough data points could be collected for these shorter heating times. For pulse times of t=160ms (Figure 6-13), t=320ms (Figure 6-14), t=640ms (Figure 6-15), t=1280ms (Figure 6-16), and t=2000ms (Figure 6-17) plots of the temperature versus time and the bubble diameter versus time are displayed. There is a sharp drop in heater temperature at the point of bubble formation, and then the heater temperature increases as the bubble grows larger. The sharp increases in bubble size are caused either by the merging of two bubbles, or by a sharp change in bubble size when the bubble edge jumps from one heated section of the resistor to another.

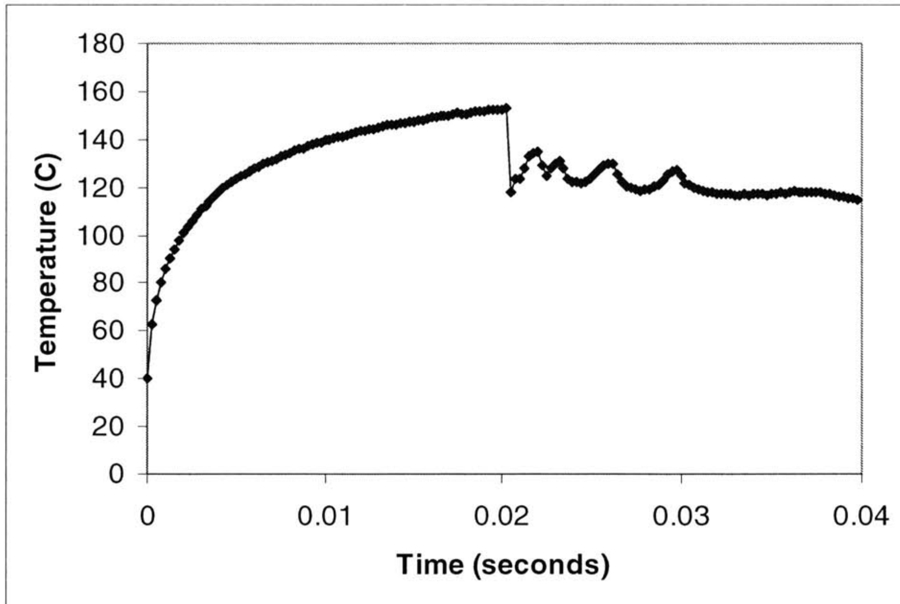

Figure 6-11 Plot of heater temperature versus time for a 40ms voltage pulse.

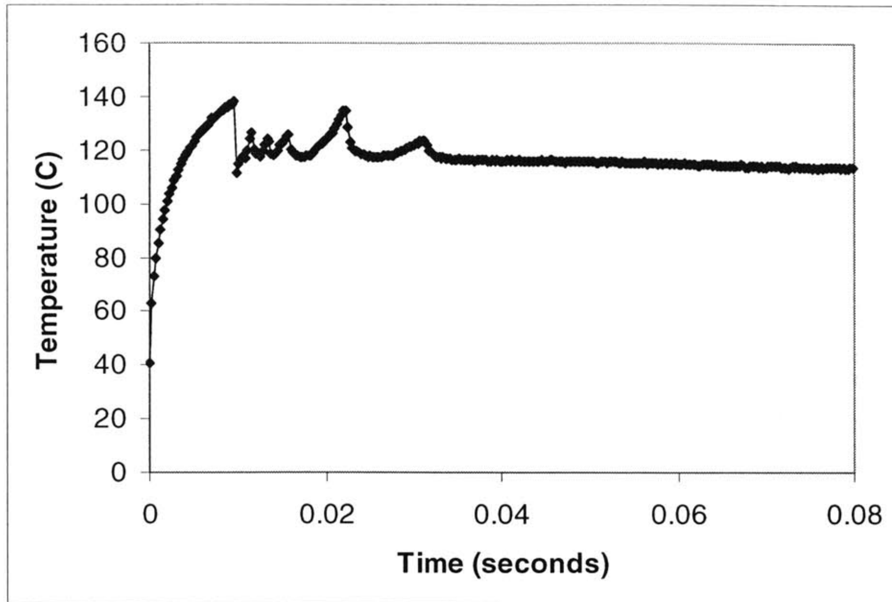

Figure 6-12 Plot of heater temperature versus time for an 80ms voltage pulse.

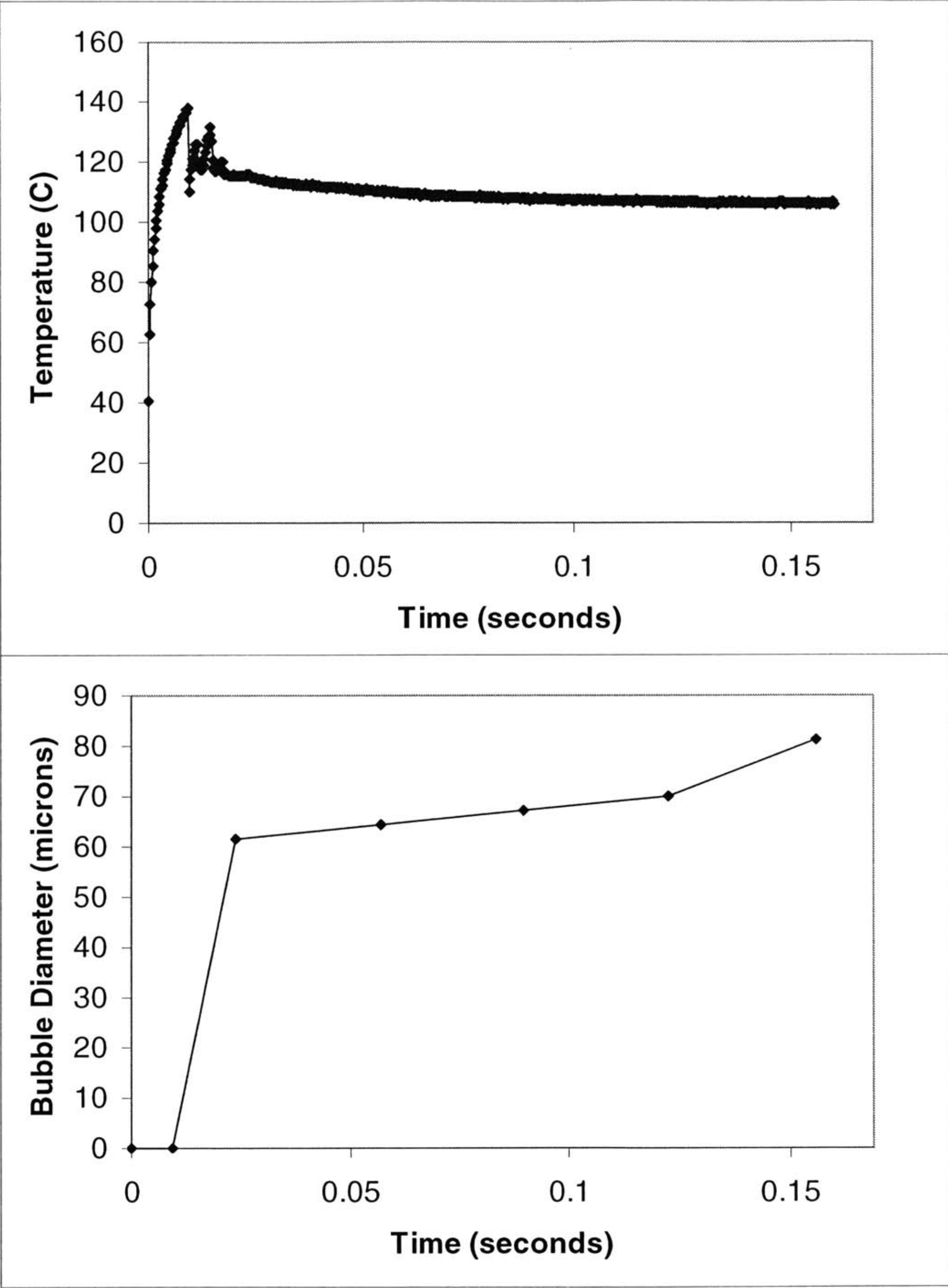

Figure 6-13 Above is a plot of heater temperature versus time for a 160ms voltage pulse, and below is the corresponding bubble diameter versus time plot.

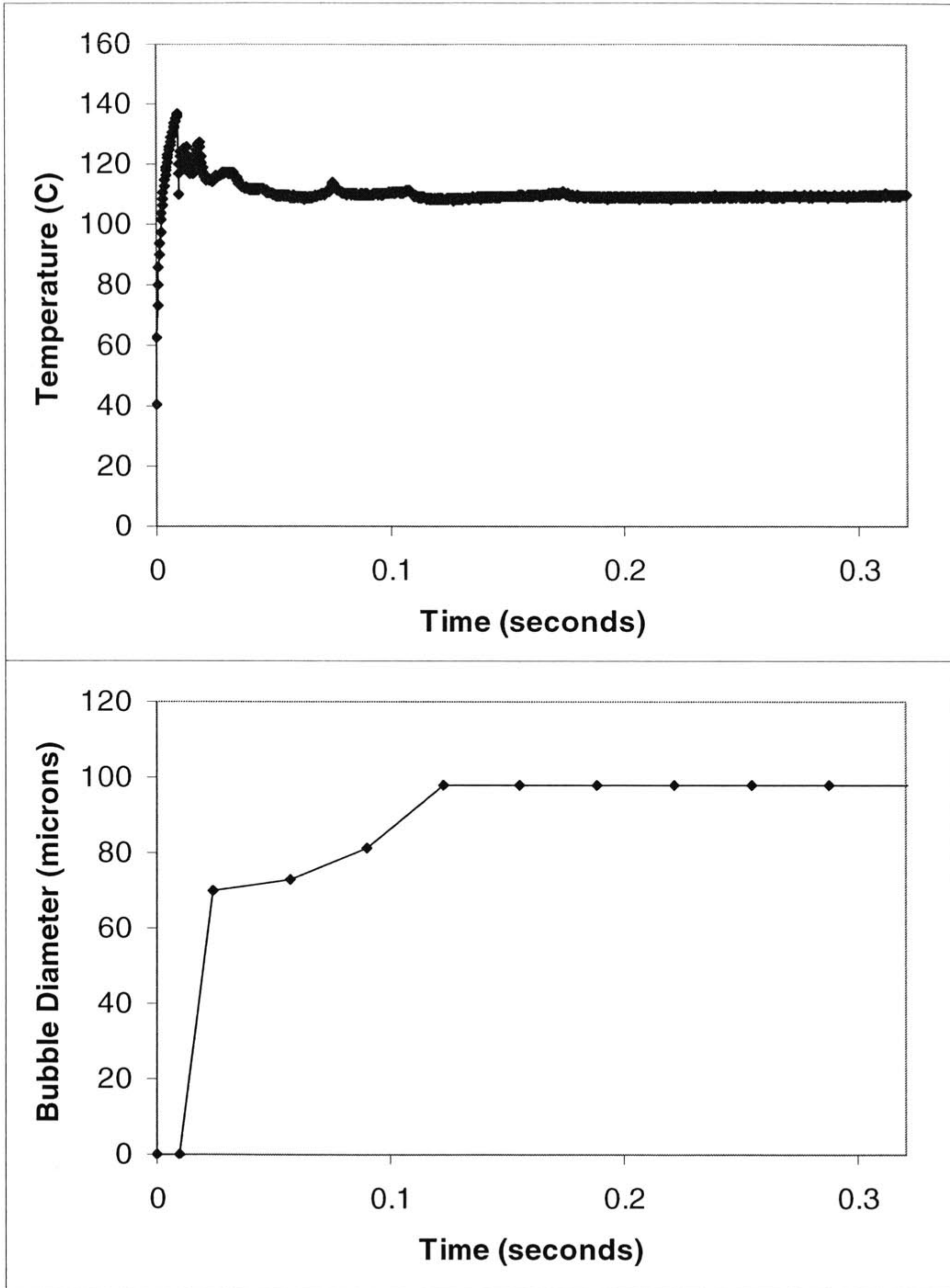

Figure 6-14 Above is a plot of heater temperature versus time for a 320ms voltage pulse, and below is the corresponding bubble diameter versus time plot.

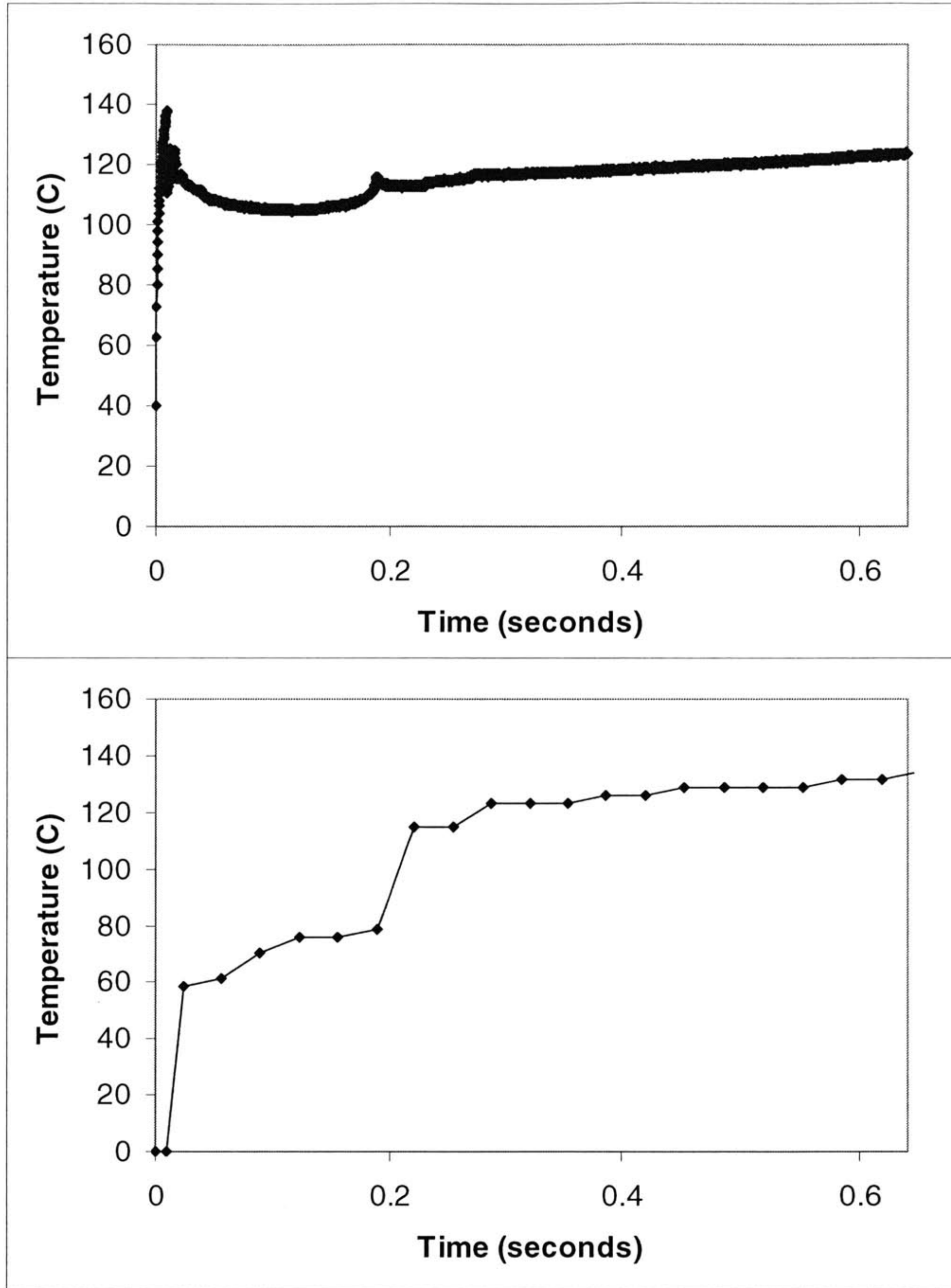

Figure 6-15 Above is a plot of heater temperature versus time for a 640ms voltage pulse, and below is the corresponding bubble diameter versus time plot.

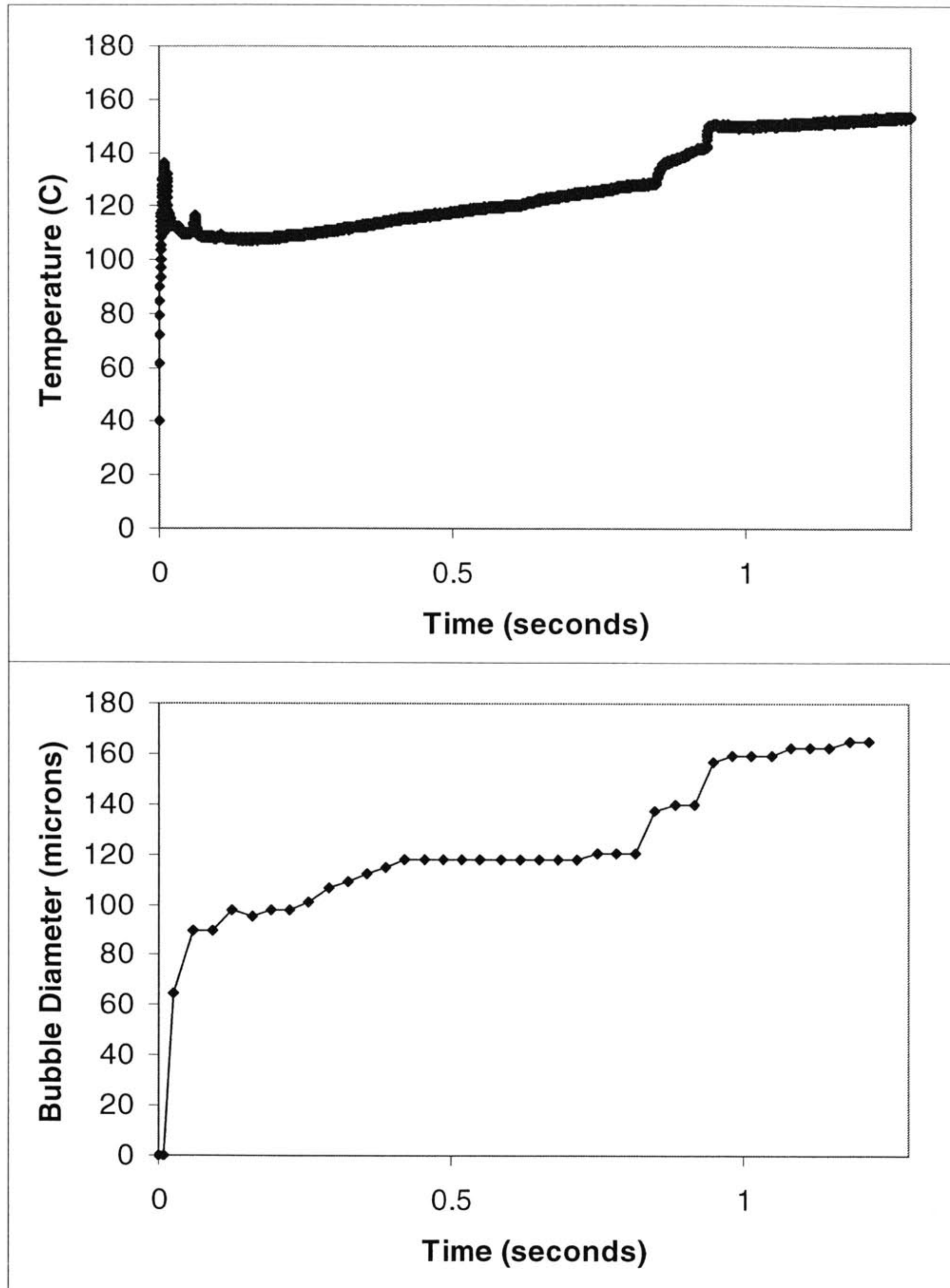

Figure 6-16 Above is a plot of heater temperature versus time for a 1280ms voltage pulse, and below is the corresponding bubble diameter versus time plot.

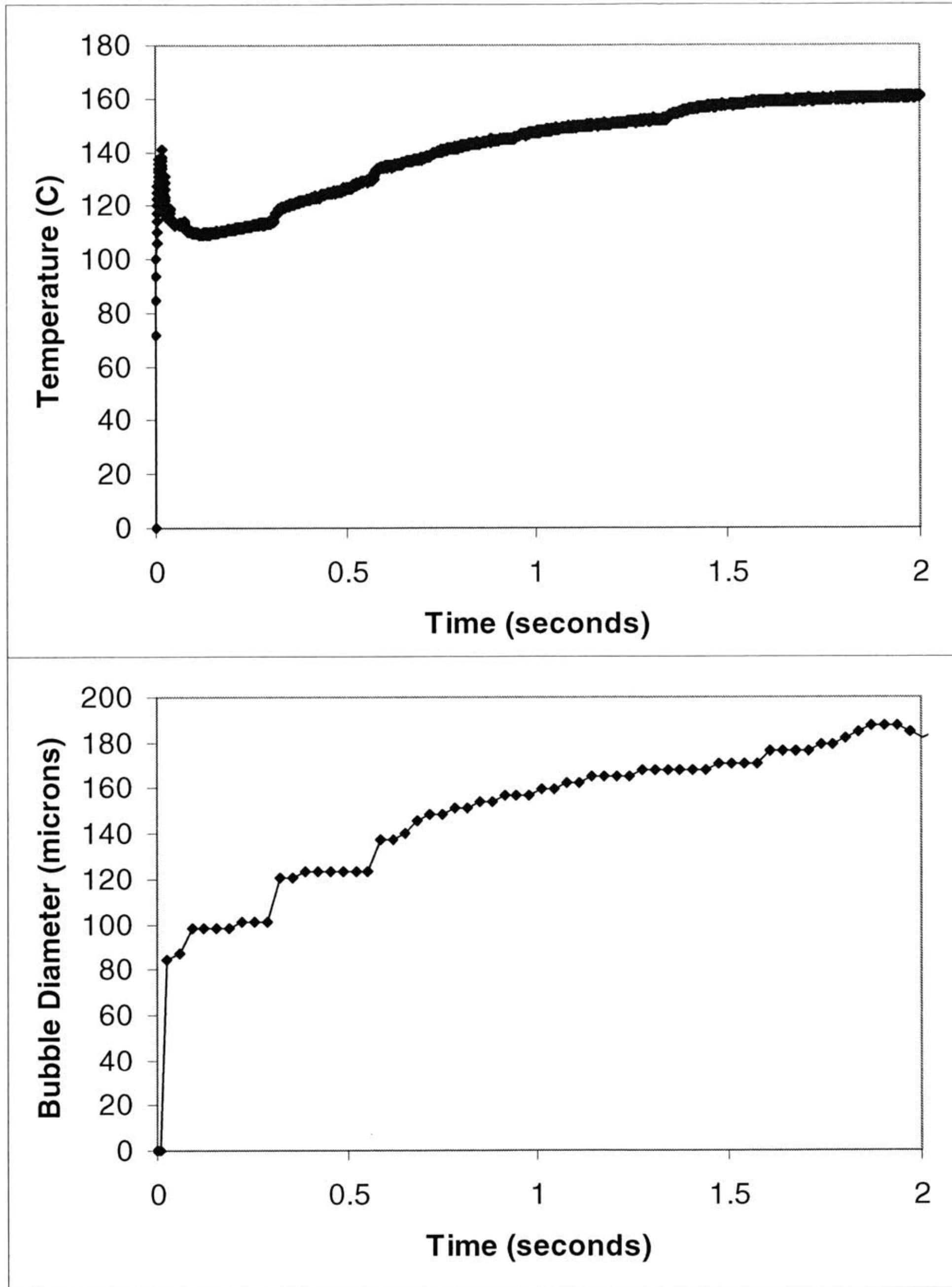

Figure 6-17 Above is a plot of heater temperature versus time for a 2000ms voltage pulse, and below is the corresponding bubble diameter versus time plot.

The captured video frames from the t=2000ms voltage pulse are shown in Figure 6-18. Initially a bubble is formed in the central cavity, and a second smaller bubble is formed above the large bubble. The bubbles grow towards each other until they coalesce at t=90ms. The bubble continues to grow symmetrically (t=189ms), but at t=321, it can be seen that the bubble has abruptly grown more to the left. This continues, and two

small bubbles at the bottom left corner of the frame start to grow larger as well. At t=750ms, these small bubbles merge, and both bubbles continue to grow. The main bubble grows towards the smaller bubble until they merge at t=1542ms. A new smaller bubble then forms in the lower left corner and the main bubble merges with that at t=1905ms. The heater is turned off at t=2000ms, and the start of bubble collapse can be observed in the final two frames. Each jump in the plot of bubble diameter is accompanied by a jump in the temperature of the heater.

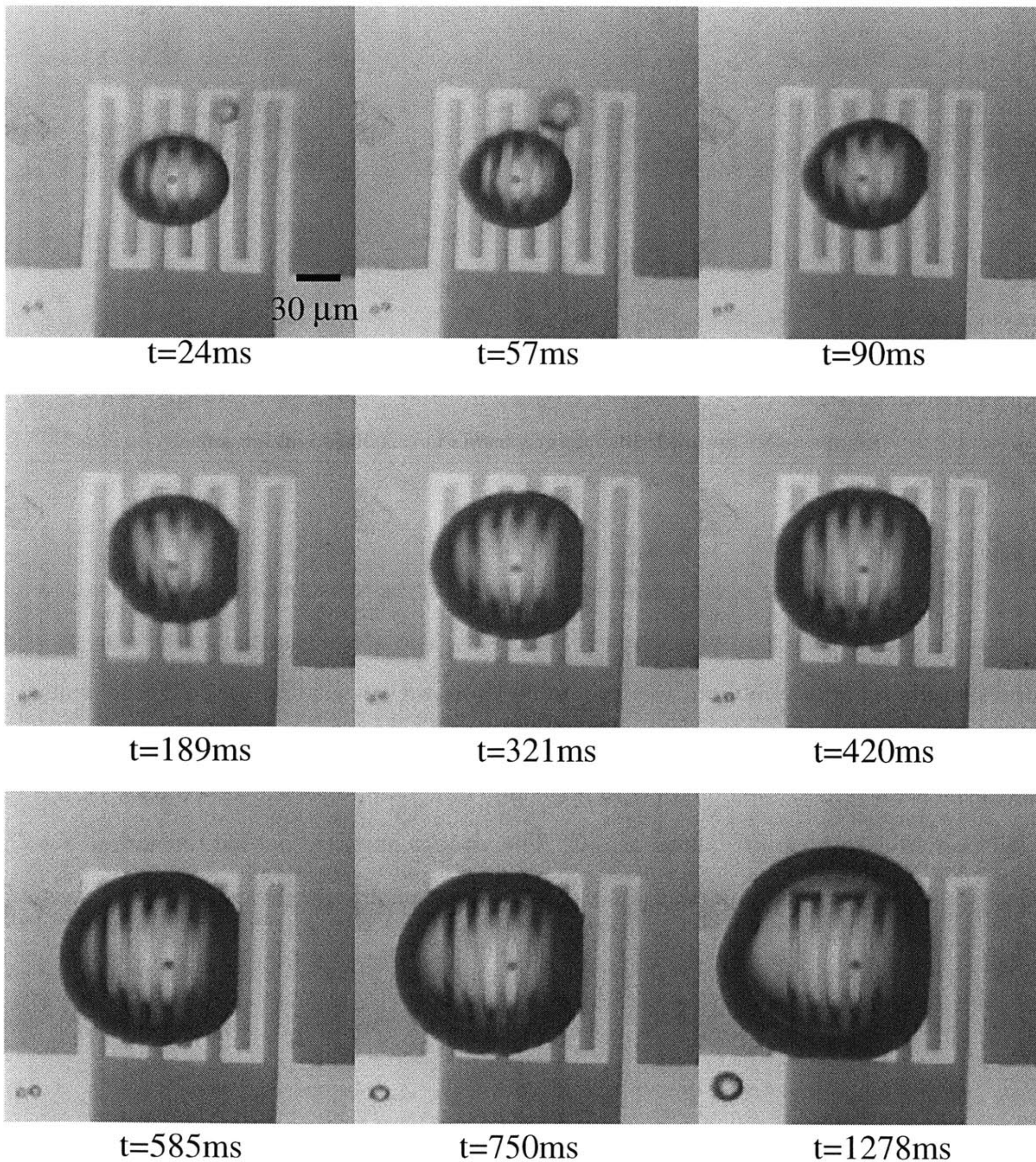

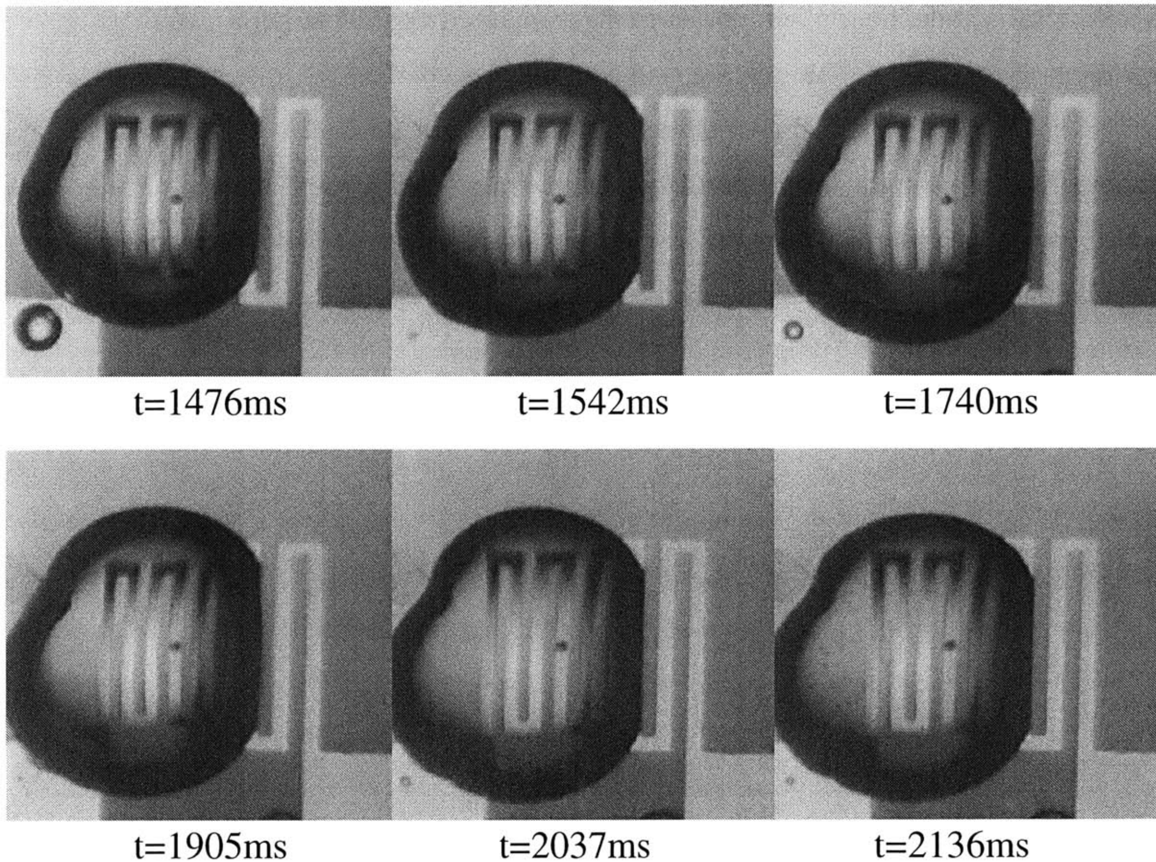

Figure 6-18 Captured video frames from the t=2000ms voltage pulse.

6.2.7 Cycling

The results of the cycling testing completed on the resistor with a central cavity 6μm wide and 4μm deep are shown in Figure 6-19. The discontinuities in the curves represent the point of bubble formation. In the plots we can see that the first eight runs have much more widely varying apparent bubble formation temperatures than the final six runs. The average apparent bubble formation temperature for the first 8 tests is 141.8°C with a standard deviation of 8°C. The average apparent bubble formation temperature for the second 6 tests is 132.2°C with a standard deviation of 3.7°C.

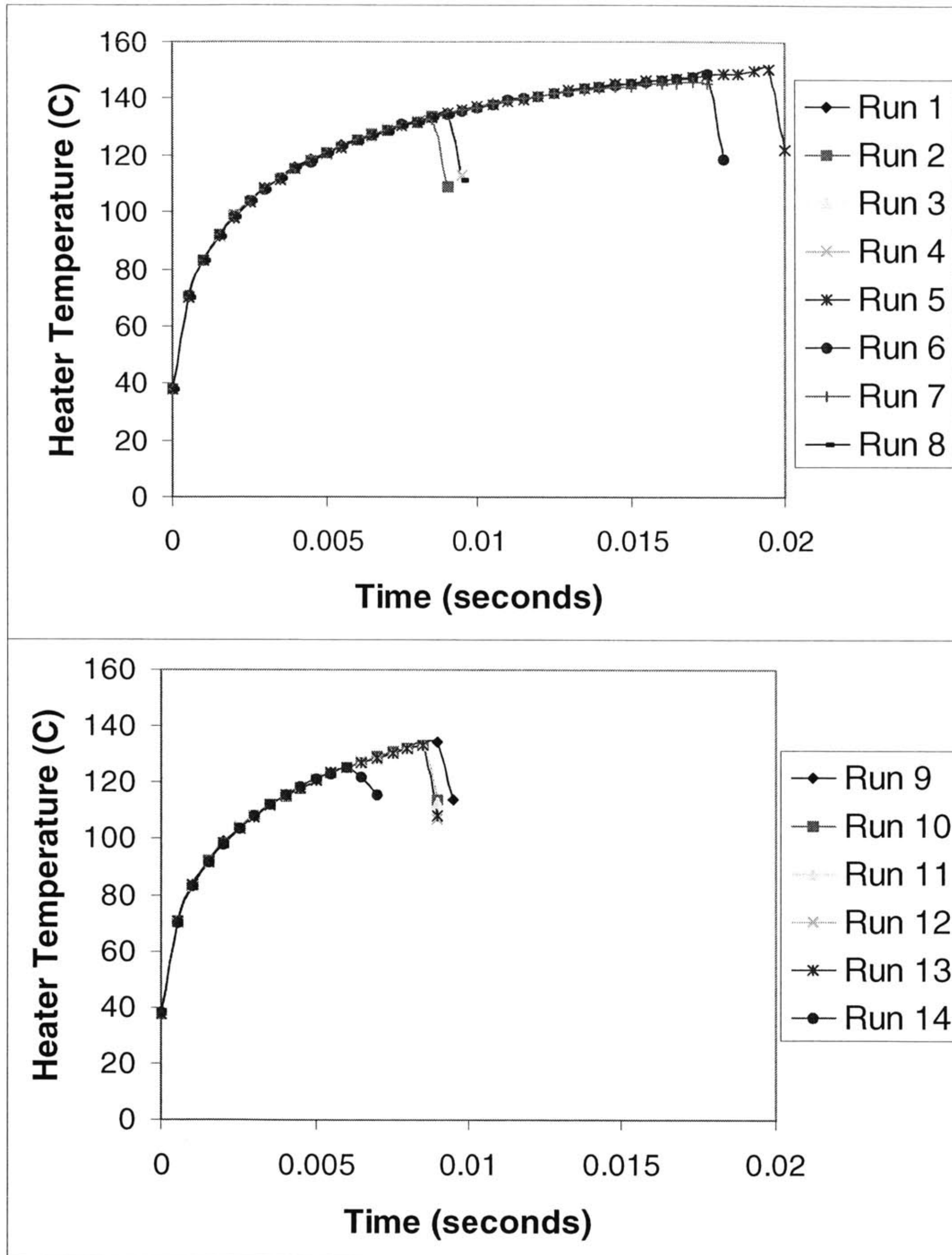

Figure 6-19 Plots of the heater temperature versus time for the cycling experiment on a folded heater with a central 6μm wide, 4μm deep cavity. The top plot shows the first 8 runs, and the bottom plot shows the final 6 runs. The discontinuities in the curves represent the points of bubble formation, and no data is shown a point after the discontinuity.

The results of the cycling testing completed on a silanized folded resistor with a 5μm diameter, 15μm deep central cavity are shown in Figure 6-20. In the plots nearly all of the bubble formation points occur around 96°C, so the individual discontinuities are

closer together. The average apparent bubble formation temperature for the first 10 tests is 96.9°C with a standard deviation of 3.5°C. The average apparent bubble formation temperature for the second 10 tests is 96.9°C with a standard deviation of 3.4°C.

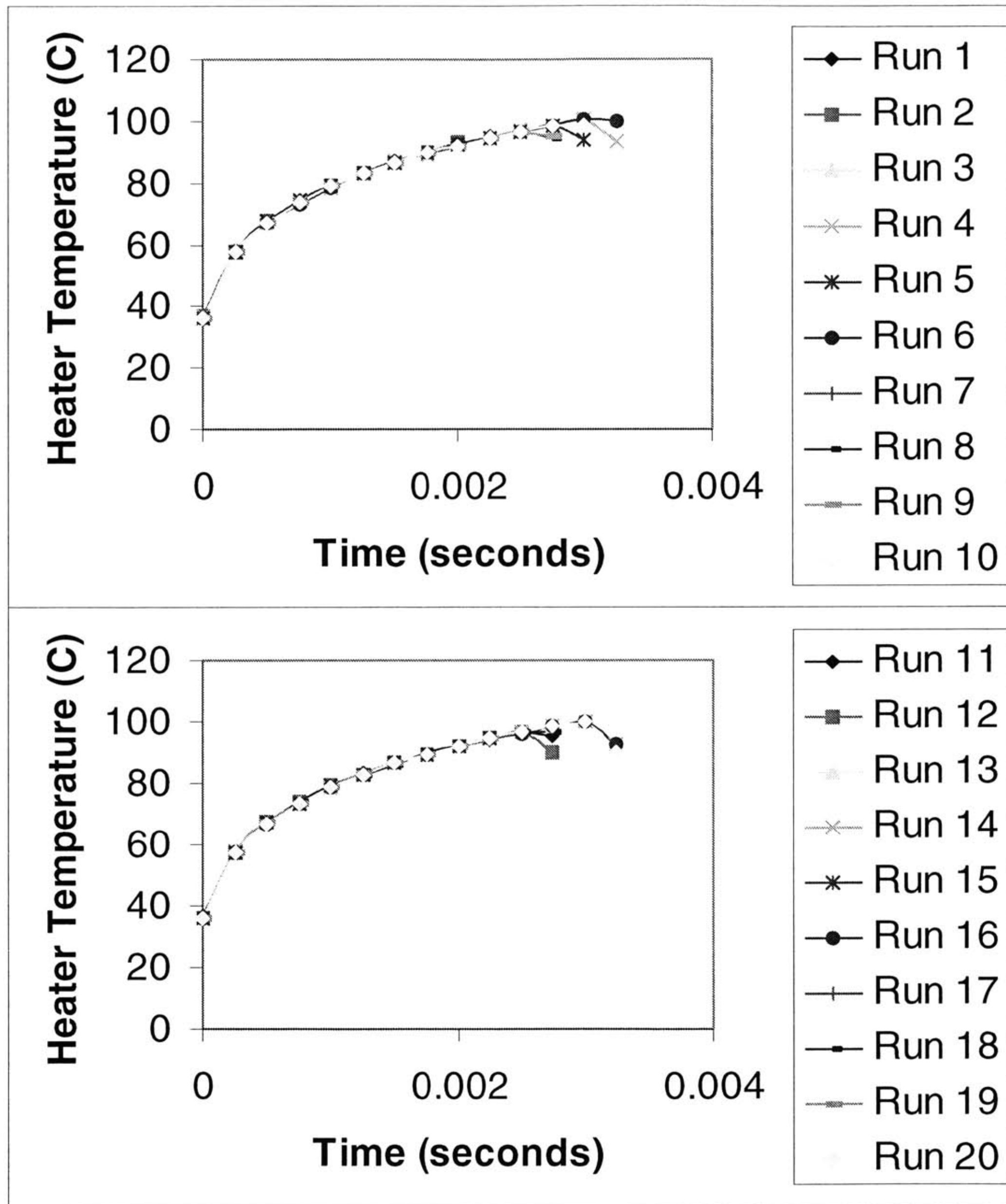

Figure 6-20 Plots of the heater temperature versus time for the cycling experiment on a folded heater with a central 5μm wide, 15μm deep cavity. The top plot shows the first 10 runs, and the bottom plot shows the final 10 runs. The discontinuities in the curves represent the points of bubble formation, and no data is shown a point after the discontinuity.

6.3 Comparison of First Generation and Second Generation Results

The most striking aspect of the second generation bubble formation temperature data when compared with the first generation results is the disparity in apparent bubble formation temperatures for equivalent tests. This difference can be explained by the fact that the data from the first generation testing was taken using line resistors, as opposed to the folded resistors used in the second generation testing. The biggest difference between the two heaters is the temperature variation. Because the temperature data collected during testing is the average temperature of the heater, we can use the results of the finite difference models shown in Chapter 2 to determine the difference between the average heater temperature and the temperature at a given point along the heater. It was found that for the line heater, the center of the heater (where bubbles usually form) is 8% hotter than the average heater temperature. Alternately, for the coiled heater, the center of the heater is 44% hotter than the average heater temperature. When we use these correction factors on the data in Table 6-3, we can see that the data from the unetched first generation testing is comparable to the data from the unetched second generation experiments.

Test	1st Generation Data	Corrected 1st Generation Data	2nd Generation Data	Corrected 2nd Generation Data
Unetched, unsilanized	220°C	238°C	158°C	228°C
Unetched, silanized	150°C	162°C	116°C	167°C
Etched, silanized (5μm wide, 5μm deep)			107°C	154°C
Etched, silanized (5μm wide,15μm deep)			96°C	138°C
Etched, silanized (6μm wide, 20 μm deep)	110°C	119°C		

Table 6-3 Apparent bubble formation temperature data from first and second generation testing, and the same data corrected for the location of bubble formation on each heater geometry.

Figure 6-21 illustrates that the results from the first and second generation testing of uncoated resistors with no cavities look very different before being corrected by the heat transfer model, but are very similar after the correction. The same is illustrated in Figure 6-22 for the silanized folded and line resistors with no cavities.

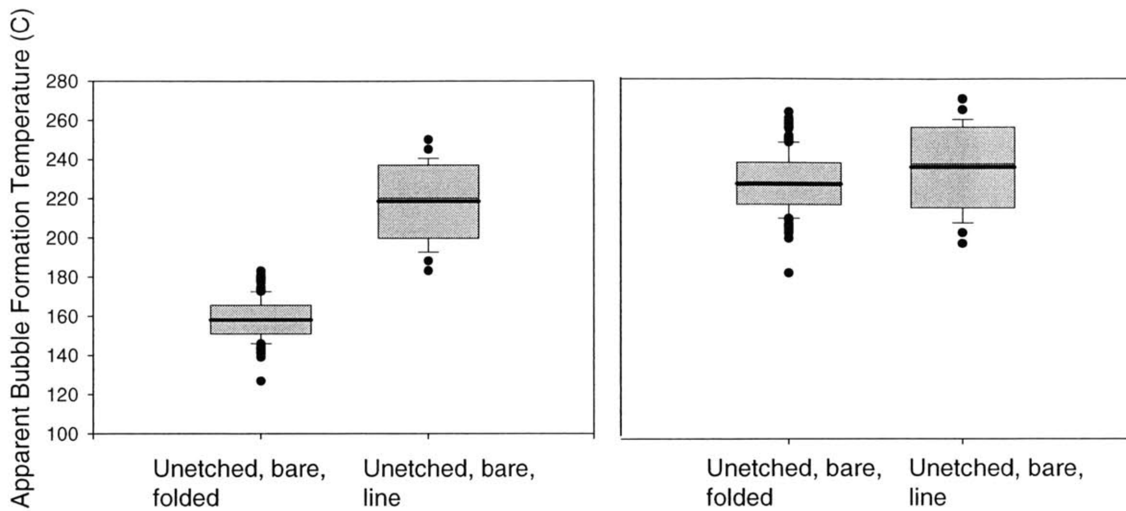

Figure 6-21 The plot on the left compares the apparent bubble formation temperatures of uncoated folded resistors with uncoated line resistors with no cavities. The plot on the right is of the same data after it has been corrected using the heat transfer model.

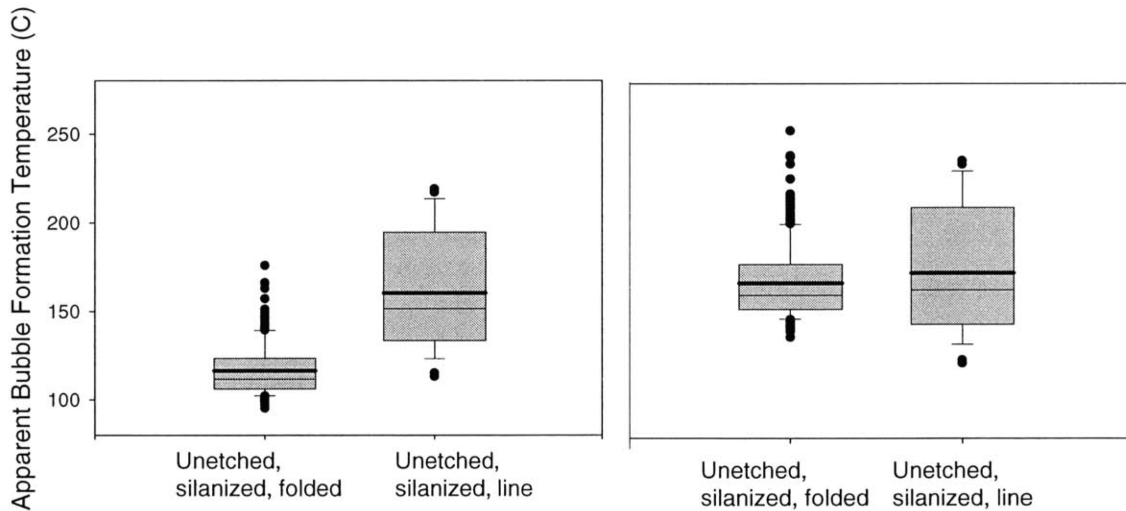

Figure 6-22 The plot on the left compares the apparent bubble formation temperatures of silanized folded resistors with silanized line resistors with no cavities. The plot on the right is of the same data after it has been corrected using the heat transfer model.

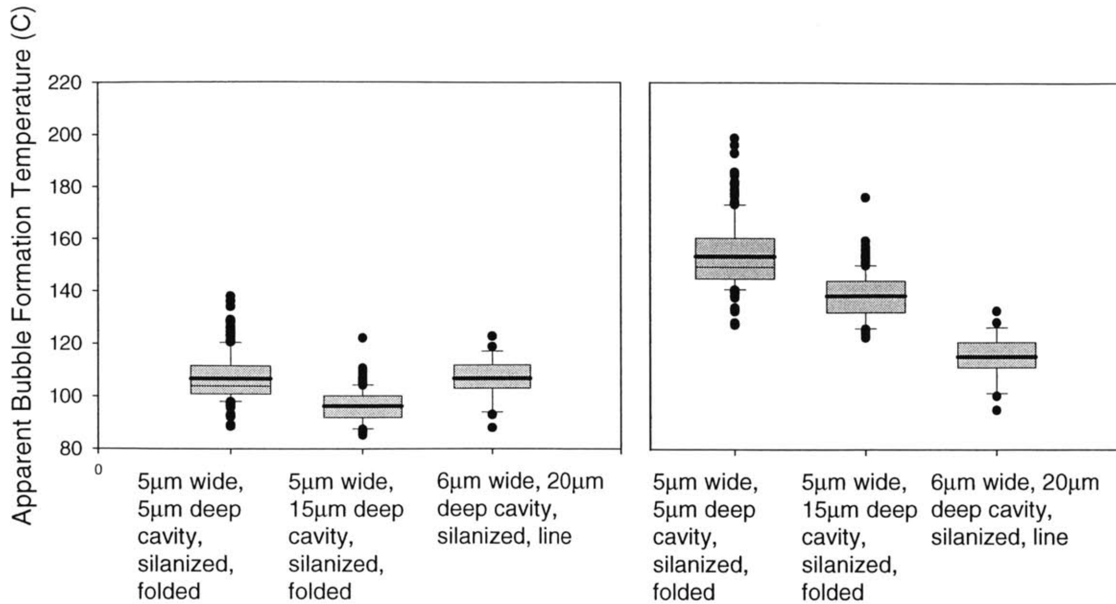

Figure 6-23 The plot on the left compares the apparent bubble formation temperatures of silanized folded resistors with silanized line resistors with cavities of different dimensions. The plot on the right is of the same data after it has been corrected using the heat transfer model.

Figure 6-23 shows the raw data and the corrected data for the silanized folded and line resistors with cavities. Because the cavity dimensions are quite different for the resistors tested, it is difficult to compare the apparent bubble formation temperatures. The data from the etched resistors is closest for the etched, silanized folded resistor with a 5µm square 15µm deep cavity when compared with the etched, silanized line resistor with a 6µm square 20µm deep cavity.

With the use of the model to make comparisons between data taken from the line heater and the folded heater, we can now observe the data for each different cavity size tested. This data is shown in Figure 6-24. As the cavities get deeper, the corrected bubble formation temperature decreases as well.

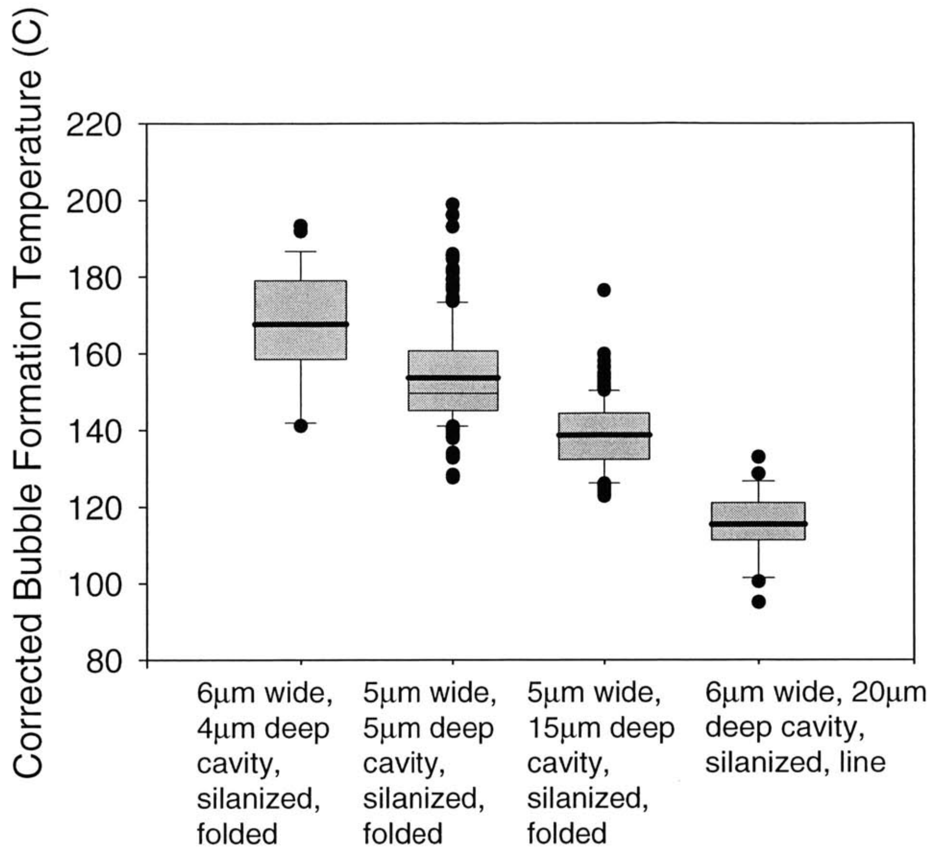

Figure 6-24 Plot of apparent bubble formation temperature corrected using the heat transfer model for each cavity geometry tested.

6.4 Complete Device

The microbubble bioparticle actuator, built with a single cell capture well and bubble chamber, functioned in accordance with the design depicted in Figure 1-3. Specifically, observing the silicon chip surface through a sequence of video frames (Figure 6-25) with a polystyrene bead as the bioparticle, one can visualize the bead being drawn into the well, remaining trapped there against a bulk flow, then being released from the well by a bubble formed in the chamber below and entrained in the flow and carried away.

During testing, it became clear that the bead entrainment in the bulk flow was dependent on a combination of the bulk flow rate and the actuating bubble size. For a given bubble size, if the bulk flow rate was too low, the bead would be ejected from the capture well, then drawn back inside. When the bulk flow rate was increased, the bead was ejected from the well and carried by the flow out of the chamber. Release flow rates

were 20-25 ml/hour (V≈600-750μm/s) for a bubble formed with the voltage ramped up to 14v (as described in the first generation testing method).

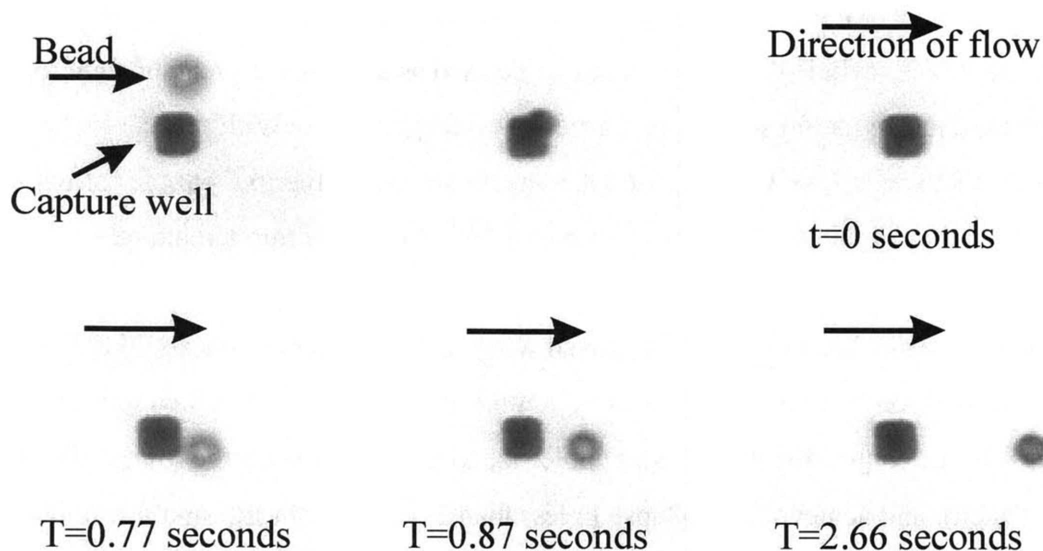

Figure 6-25 Sequential photos of device operation during bead capture, holding, and ejection. In the first two frames a backflow pulls a 10μm bead into the capture well. At t=0.00 seconds, a bead is trapped in the well and held against a flow of 20ml/hour. When the resistor is heated, the bead is rapidly ejected from the well (t=0.77 and t=0.87 seconds). In the final frame, the bead is entrained in the flow and carried out of the chamber.

7 DISCUSSION AND CONCLUSIONS

7.1 Overview

Our objective was essentially twofold: To establish a mechanism for bubble formation that is sufficiently deterministic to be used as an actuation scheme, and to demonstrate the actuation scheme in a proof-of-concept device. With respect to the first goal, our data suggest we were able to take largely stochastic thermal bubble formation, and control the conditions sufficiently to turn bubble formation into a relatively deterministic process at the macroscopic scale. With etched cavities, hydrophobic surface treatments, and the use of de-gassed water as the test liquid, we could precisely locate the position at which bubbles form, control the temperature at which they form to within 5-10°C, control the maximum bubble size to within 1μm (for the lowest energy levels tested), and achieve full collapse in less than 2 seconds (for the smallest bubble sizes tested). As for the second goal, we demonstrated a working bioparticle acuator using the controllable microbubble technology.

7.2 Discussion of First Generation Results

The first generation testing served to help us identify several of the important factors in controlling bubble formation and collapse. Many of these phenomena were explored in more detail during the second generation testing, where the measurement and control techniques were more sophisticated.

On unpatterned line resistors, several bubbles would spontaneously nucleate at the same time at random locations on the heaters, at temperatures of 200-250°C. The addition of a hydrophobic layer (either CYTOP^{TM} or silanization) over resistors with etched cavities resulted in bubble formation exclusively in the cavities. While uncoated wafers with cavities almost never formed bubbles exclusively in the cavities approximately, the surface coatings resulted in 98% bubble nucleation in cavities. We believe that the hydrophobic layer made it possible for the cavities to trap more air to act as a seed for bubble nucleation.

As the bubbles nucleated in cavities for the two treated wafers, it makes sense that they formed at lower temperatures, since the bubble formation temperature is inversely proportional to the size of the cavity in which the bubble forms. The higher apparent

bubble formation temperature for the CYTOP^{TM}-coated wafers in comparison with silanized wafers can be explained by the greater thermal resistance of the CYTOP^{TM}. Since the CYTOP^{TM} layer is 1μm thick, considerably thicker than the effect of silanization (which is a monolayer), it follows that this added thermal resistance would require a higher resistor temperature (and hence a higher apparent bubble formation temperature) to achieve the same temperature at the site of bubble formation as occurs for silanized wafers with no added thermal resistance. Thermal modeling suggests that the temperature drop across the CYTOP^{TM} layer could be 10-20°C at bubble formation, which is consistent with our finding that the apparent bubble formation temperature (the resistor temperature) is about 15°C higher for CYTOP^{TM}-coated versus silanized.

The final decision to use CYTOP^{TM} as the surface treatment for the resistors in the proof-of-concept device was based upon several factors. The bubble formation temperature was actually more repeatable for the silanized resistors than for the CYTOP^{TM}-coated resistors, but silanization does not passivate the resistor surface, making the use of ionic solutions difficult since water could undergo electrolytic breakdown in operation. Since we plan to use this device for bioparticles and cells, the use of deionized water will not be practical. Also CYTOP^{TM} provides a good bond between the quartz and silicon wafers, simplifying the fabrication of the finished device, and the bubble position is nearly as controllable with CYTOP^{TM} as with silanization.

7.3 Discussion of Second Generation Results

7.3.1 Bubble Formation Location

In the first generation testing of the line heaters, we observed that the presence of an etched cavity in the heater resulted in bubble formation exclusively in that cavity. For these line heaters, the cavity was always located in the center of the heater, which is also the hottest portion of the heater as shown by the finite difference model. In testing the folded heaters, we looked at the effect of cavity placement, in addition to the effect of the presence of a cavity. For this testing we compared heaters with centrally-located cavities to heaters with cavities located at the edge of the heated field, knowing from the modeling that the temperature variation across the folded heaters is significant (the center is more than 50% hotter than the edge).

As expected from previous testing, the folded resistors with cavities in the center formed bubbles in the cavities in 100% of the trials, regardless of the cavity depth. However, the heaters with peripherally-located cavities only formed bubbles in the cavities about 50% of the time, and when bubbles were not formed in a cavity, the bubble always formed in the center of the heated field.

There is some uncertainty in the percentage of bubbles that formed in the cavities for the edge cavity resistor testing due to the frame rate of the video capture. When a bubble forms in and edge cavity, it usually shifts to the center of the heated field within one frame. Consequently, it is possible that some of the bubbles that look as if they formed in the center of the heated field, actually formed in an edge cavity, but then shifted to the center too quickly for the video to capture. The tendency of the bubbles to be attracted to the hottest part of the heater is caused by the Marangoni effect [69]. When a bubble is in a heated field with a temperature gradient, a gradient in surface tension results along the surface of the bubble that drives the bubble towards the hottest part of the field until it can reach equilibrium. This effect was observed often in the movement of the bubbles from the edge of the heater towards the central portion.

The apparent bubble formation temperature data for resistors with edge cavities presented in the previous chapter was separated into four groups. Resistors with a 5μm deep edge cavity where the bubble formed in the central region, those where the bubble formed in the edge cavity, resistors with 15μm deep edge cavities where the bubble formed in the central region, and those where the bubbles formed in the edge cavity. Using the results of the finite difference heat transfer model developed in Chapter 2, the bubble formation temperature data was corrected based on the position of bubble formation (edge cavity or central region). The results of this analysis are shown in Figure 7-1.

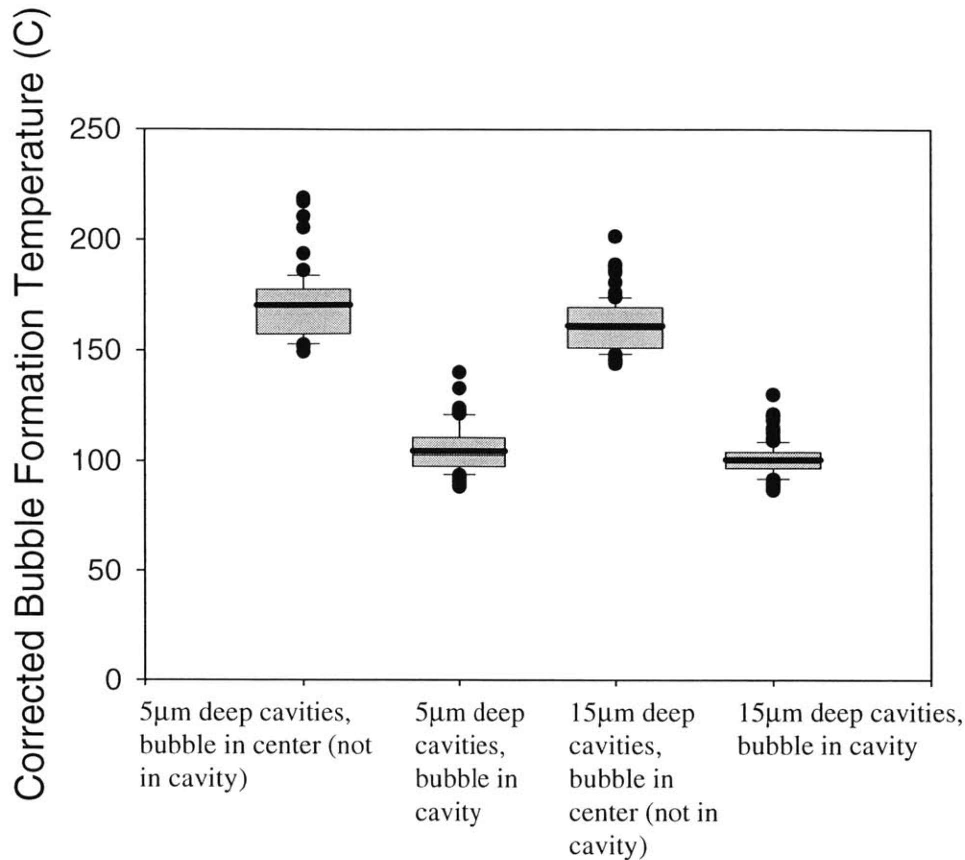

Figure 7-1 Corrected apparent bubble formation temperature data for resistors with edge cavities. The data has been divided based upon the apparent position of bubble formation.

Upon initial inspection, this data looks to be promising, however, when compared to the corrected data for resistors with central cavities and no cavities (Table 7-1), there are significant differences in apparent bubble formation temperature when the bubble forms in a central cavity. The bubble formation temperature is very similar between trials of resistors with no cavities, and those where the bubbles do not form in the cavities. However, the corrected bubble formation temperature is significantly lower for bubbles forming in edge cavities than for bubbles forming in central cavities. Furthermore, there is virtually no apparent difference between the uncorrected bubble formation temperature when a bubble forms in an edge cavity, and when it does not form in a cavity. First, it is inconclusive as to how often the bubbles actually form in the edge cavities, since the frame capture rate is not significantly fast to capture all of the dynamics. Second, there is no significant difference between the average heater temperature at bubble formation for either of these two cases.

Cavity Depth	Bubble Position	Corrected Average Apparent Bubble Formation Temperature	Uncorrected Average Apparent Bubble Formation Temperature
None	Center	167°C	116°C
5μm	Center (not in cavity)	170°C	118°C
5μm	Center (in cavity)	154°C	107°C
5μm	In edge cavity	104°C	118°C
15μm	Center (not in cavity)	161°C	112°C
15μm	Center (in cavity)	138°C	96°C
15μm	In edge cavity	100°C	114°C

Table 7-1 Comparison of apparent bubble formation temperatures for resistors with various cavity locations, and different bubble formation positions. Both the raw data, and the same data corrected using the heat transfer model are presented.

Because the purpose of this thesis was to determine methods in which to make the bubble formation process more controllable, we can conclude that micromachined cavities should be positioned in the center of the heated field for optimal results. By doing this, bubbles form in the cavities 100% of the time, hence, the location of bubble formation is fully controllable.

7.3.2 Bubble Formation Temperature

The goals with regard to controlling the bubble formation temperature were to make the temperature more repeatable, and to minimize it in order to ensure bubble positioning and to minimize the power requirements of the system and to make it more suitable for biological testing. Two factors were identified in order to accomplish this. First, cavities were etched into the heaters in order to act as bubble nucleation sites. Second, hydrophobic surface coatings were used to make the gas-trapping properties of the cavities more effective.

In this phase of testing we tested resistors with cavities 5μm in diameter and either 5μm or 15μm deep. We hypothesized that the deeper cavities would result in a lower bubble formation temperature because the cavities would capture a larger amount

of gas to use as a seed for bubble nucleation. This hypothesis was confirmed by the results of the testing, as the corrected average bubble formation temperature was 16°C lower for the deeper cavity. This hypothesis was also supported by the results from the silanized resistor in the first generation testing that had a cavity 6μm wide and 20μm deep (1μm wider and 5μm deeper than the deep cavities in the folded resistors). In this case, the corrected average apparent bubble formation temperature was 19°C lower than the 15μm deep cavity in the second generation testing. It must be mentioned that because the cavity was both wider and deeper, it is unclear which of these variations contributed more to the lower apparent formation temperature.

The results of the testing of the resistor with the shallower, wider cavity (6μm wide, 4μm deep) agrees with the hypothesis that shallower cavities result in a higher apparent bubble formation temperature. It is important to note that the wider cavity opening does not necessarily contribute to a lower apparent bubble formation temperature in this case. A wider, shallower cavity is less likely to trap a significant quantity of gas to act as a seed for nucleation, and hence, the aspect ratio of the cavities may have an important effect on the apparent bubble formation temperature.

Previous literature on bubble formation has not explicitly addressed the relationship between the depth of a nucleation site and the bubble formation temperature. The width of the cavity has been addressed, but the only mention of the depth is that it ought to be deeper than the cavity is wide to trap a significant amount of gas [60, 70]. We have shown in this thesis, that cavity depth does, in fact, have a significant effect on the apparent bubble formation temperature. Further study would be needed to determine whether there is a limit on how deep a cavity can be before the bubble formation temperature begins to increase. The data suggest that the aspect ratio of the nucleation site also has a significant effect on bubble formation temperature, and further work would help to elucidate this point further.

With regard to cavity depth, there is a trade-off that must be addressed. We have shown that deeper cavities result in a reduced apparent bubble nucleation temperature, however, the processing required to etch a deep cavity in quartz is time-consuming and expensive. For future bubble actuation applications, the user must decide whether the 10-30°C bubble formation temperature reduction warrants the additional time and expense of

fabricating deeper cavities. Alternately, perhaps a different substrate material could be chosen that is easier to etch. Additionally, the data suggest that the aspect ratio of the cavity (width:depth) should be maintained 1:1 or deeper since the cavities with the 3:2 aspect ratio had a significantly higher apparent bubble formation temperature, and less reliable bubble position.

In the first generation testing, two hydrophobic surface coatings were investigated: silanization and CYTOP™. In that phase of the testing, we were also trying to find the optimal coating for the full bioparticle actuator, so for the reasons previously described, CYTOP™ was explored in more detail. For the second generation testing, we were pursuing the more general goal of controlling bubble formation. For this we explored silanized resistors and avoided confounding effects of CYTOP™ coatings that intrinsically bring an additional and variable thermal resistance. The long-term stability of silanization has not been thoroughly investigated, however, our testing has demonstrated no noticeable degradation in the hydrophobic quality after one year. Should the silanization degrade, it is possible to flow the silanizing agent through the device and silanize the surface in-situ.

Another important result of the bubble formation temperature testing is the fact that a discontinuity on the heating curve signifies bubble formation. This fact can be used in future bubble powered devices, for monitoring or control purposes. Being able to electronically determine whether or not a bubble has formed on the heater, frees the designer from the need to visually monitor the bubble formation.

7.3.3 Bubble Dynamics

The results of the long-pulse testing of the resistive heaters are not immediately applicable to the design of bubble-powered devices because most devices would require a short bubble formation time and a minimized power input, however, the results are interesting nonetheless. There are two main findings that should be addressed.

First, it is apparent from the data that bubbles are attracted to each other. Even when there was a large amount of space between the main bubble on the heater and a small peripheral bubble, the large bubble would grow asymmetrically in the direction of the smaller bubble until they were close enough to merge. This kind of bubble behavior

is probably caused by flow fields that exist around each bubble and interact so as to attract them to each other.

The second piece of useful information taken from the results is that the heater temperature increases as the bubble diameter increases. It is possible to observe abrupt changes in the bubble size on the heater temperature curve as abrupt rises in the heater temperature. Perhaps in the future, this phenomenon could be used to more accurately monitor and control the size of the bubble on the heater without need for visual interfacing. The temperature rise of the heater due to the growth of the bubble is probably due to the increased thermal resistance of the vapor/gas mixture filling the bubble compared to the higher conductivity of the fluid surrounding the bubble.

7.3.4 Dependence of Bubble Diameter on Energy

We found that the maximum bubble size increased as the total energy applied to the heater was increased. We also found that as the time of the voltage pulse applied to the heater increases, the variability of the maximum bubble size increases as well. A shorter pulse of greater magnitude yields a more repeatable bubble size than a pulse applying the same energy to the heater over a longer period of time. Both of these results could be used in order to choose the proper operating parameters for future bubble-powered devices, although further study should be undertaken in order to concretize these results.

It makes sense that the amount of energy applied to the heater should control bubble size. It is important to remember, however, that the energy applied to the heater is not the same as the energy applied to the bubble formation process. The bubble takes up only a fraction of the full heated surface, so most of the energy is being used to heat the quartz substrate and the surrounding water. Only a fraction of the total energy is going to changing water into vapor.

As the heating time increases, it makes sense that the range in resultant bubble sizes increases because for each bubble formed the properties of the formation and growth must vary somewhat, as boiling is a stochastic process. Any variations will be more pronounced if the bubble is grown for a longer time, giving differences in the temperature field more of a chance to propagate and manifest itself as greater variation in bubble diameter. Given this result, future bubble devices where the bubble diameter is

critical should use shorter voltage pulses to achieve greater repeatability of maximum bubble diameter.

7.3.5 Bubble Collapse

As mentioned earlier, several groups have reported difficulties with residual bubbles in both thermal and electrochemical bubble devices [18, 19, 23, 34]. When bubbles are thermally generated in water, dissolved gas diffuses into the vapor bubbles, resulting in air bubbles left behind when the heater is turned off. When we first began working with vapor bubbles, we experienced similar problems, but then found a protocol whereby residual bubbles could be avoided. The bubble dissipation time was decreased largely due to the identification of factors that allow dissolved air to diffuse into the bubbles. Since water vapor will condense back into the liquid form after heat is removed, it was determined that air in the vapor bubbles was slowing down the collapse time. We found that boiling water before using it to test the resistive heaters reduced the amount of dissolved air since the solubility of air in water decreases with increased temperature.

The estimates of bubble collapse time shown in Chapter 2 calculate the bounds for the bubble collapse. At one end, if the bubble is composed of pure water vapor, the heat transfer-controlled collapse time is of the same order of magnitude as the heating time, about 50ms. If the bubble is composed purely of air, then the diffusion-controlled bubble collapse time is greater than 90 minutes. Obviously, our data fall within these two bounds, with collapse times on the order of seconds. Both regimes have collapse time as a function of the square of the bubble diameter, which agrees with our experimental data.

For the heat transfer-controlled collapse, the time is on the order of 10^{-2} seconds, whereas for the diffusion-controlled collapse, it is of the order 10^{3} seconds. At about 10^{0}-10^{1} seconds our collapse regime is at about the midpoint of the two outer bounds. This does not necessarily mean that there is half diffusion and half heat transfer collapse occurring, however. There is probably significantly less air than vapor present in the bubble. As the bubble collapses by phase change at the interface, the dissolved air begins to build up at this interface making it more difficult for the water vapor to reach the edge. The water vapor most likely needs to diffuse through the layer of dissolved air in order to reach the water/gas interface and condense. In this way, a small quantity of dissolved air can significantly slow down the bubble collapse process.

Previous researchers were unable to solve the dissolved gas problem, and were also unable to accurately control the maximum bubble size in order to limit the bubble collapse time. From our bubble collapse results, we can see that smaller bubbles collapse more quickly. We also have shown that it is possible to control the bubble size by controlling the total energy applied to the heater. Hence, by degassing the water by boiling, and limiting the vapor bubbles' maximum size, we have succeeded in reproducibly creating vapor bubbles that take as little as 1-2 seconds to collapse completely.

7.3.6 Cycling

We have defined cycling as the repeated formation of a bubble on a heater, using the same water. It was thought that by forming a bubble several times in a row, that the cavity would trap more vapor or gas and hence be 'activated,' or able to nucleate a bubble more easily. Our results in the cycling testing for the heater with a wider, shallower cavity (6μm wide, 4μm deep) supported this hypothesis, in that as more cycles had been completed on a heater, the formation temperature became more repeatable. The initial runs had a higher average temperature of apparent bubble formation, and were significantly less repeatable. The final runs had a lower average temperature and were more repeatable.

Alternately, in the testing of the resistor with a narrower, deeper cavity (5μm wide, 15μm deep), there was a negligible difference between the first half of the testing and the second half. The apparent bubble formation temperature was very repeatable from the start.

The most likely explanation of this phenomenon is that the shallower, wider cavity was less able to trap a sufficient quantity of gas in the beginning, but that subsequent testing helped to fill the cavity with more vapor. On the other hand, the narrower, deeper cavity was able to trap an adequate nucleation seed from the beginning, and did not need cycling to make the cavity more active. This data suggests that in designing future bubble actuated devices, the aspect ratio of the cavities may determine whether cycling is necessary in order to achieve more repeatable bubble formation.

7.4 Future Work

7.4.1 Concluding Recommendations for Controllable Bubble Formation

In the design of future bubble-powered devices, many design guidelines have been presented in this thesis. We have presented methods by which the location of bubble formation may be predetermined, the nucleation temperature may be minimized, the time of formation may be detected, the maximum bubble size may be controlled, and the bubble collapse time can be kept below 10-20 seconds.

In designing bubble-powered devices, the location of bubble formation may be controlled by etching cavities in the heaters. The designer must decide whether she prefers the lowest possible bubble formation temperature by etching deeper cavities, at the cost of a longer, more expensive fabrication process. For many applications, shallower microcavities could probably provide a sufficiently reliable bubble formation testing. For very shallow cavities, cycling may be useful to achieve repeatable bubble formation.

Two different hydrophobic surface treatments have been presented. Depending on the application, the designer can choose which coating will be most compatible with the system. The CYTOP™ is good in that it passivates the heater surface and can be used to bond the quartz chip to silicon. However, it adds additional thermal resistance and increases the power requirement of the system. Alternately, the silanized heaters have more repeatable apparent bubble formation temperatures, and silanization is a monolayer, and hence adds no significant thermal resistance to the system. However, the silanization does not passivate the surface, so if an ionic solution was the working fluid, electrochemical reactions could occur.

The size of the bubble may be controlled by adjusting the total energy applied to the heater. This should be more rigorously examined and modeled in future work in cases where precise bubble sizes are required.

Many of the issues that hindered previous bubble-powered devices have been addressed and improved. A set of guidelines for the design of future devices has been presented. More detailed attention could be given to some of the bubble formation and collapse properties in the future, however, the guidelines presented in this work can be used to design a robust bubble-powered system.

7.4.2 Microbubble Bioparticle Actuator

The proof-of concept device was able to successfully capture, hold, and release polystyrene beads. There are several steps that are necessary in order to use the device for single cell analysis. First, more testing should be done to determine the relationship between the actuating bubble size and the release flow rate. It would be helpful to know the threshold bubble size necessary to successfully release a bioparticle for a given bulk flow rate, or vice versa. Future devices could be designed using the proper energy pulse to form a bubble with the desired diameter and collapse time. Second, we must test the device using biological cells in solution and confirm that cells are not adversely affected by the device. A small array of devices should then be fabricated and used with live cells. Issues for this step would include effective single-cell capture and electrical control of the heaters. At this point the optical system that would be necessary for scanning the cell array should be implemented for the small array. The final step would be to create an array of several thousand cell actuators on a chip, so a large array of single cells could be observed and sorted.

7.4.3 Microbubbles

The resistors and testing system used for observing microbubble formation open up the opportunity for a more in-depth study of the physics of bubble nucleation. Microfabrication has not been widely used in this area, but we have shown that the ability to machine bubble nucleation sites and precisely position bubble formation can make observing bubble formation more straight-forward. It is possible to determine the exact size and shape of nucleation sites, as well as modify surface chemistries and measure the heater temperature. The detection of the heater temperature could be made more precise by building a separate heat-sensing element, not linked to the resistive heater. In this way it would be possible to position the temperature sensor at the bubble nucleation site in order to measure the precise bubble-formation location instead of the average heater temperature at bubble formation.

In addition to the application of microbubble actuation demonstrated in this thesis, there are many other possible uses for controllable microbubble actuation. Simple microfluidic valves and pumps are crucial for the creation of effective lab-on-a-chip systems, which must be able to actuate small volumes of fluid efficiently. This actuation

mechanism could also be useful for drug delivery devices, though more work should be done to fully characterize the repeatability of bubble size for volume-sensitive delivery applications.

For applications where the fluid to be actuated should not be boiled, a working fluid could be used in a chamber bounded by a membrane. In this way, bubble formation in the working fluid would deflect the membrane in order to move the necessary fluid. This could be useful in non-biological applications, such as fuel-injection, where boiling the fuel would not be advisable.

7.5 Concluding Remarks

In conclusion, we have demonstrated that, using resistive heaters with micromachined nucleation sites, bubbles can be formed in precise locations, caharacterized by formation temperatures that are reduced and repeatable to within 5-10°C, with maximum diameters that are repeatable, and then can collapse completely within seconds of formation. This technology and method for yielding a rather deterministic bubble formation process is on the critical path for using bubbles as a robust actuation scheme. The fabrication technology involves materials that are biocompatible and processes that are scalable. In a proof-of-concept device, we demonstrated that bubble actuation could be used to actuate cell-sized particles. A device has been demonstrated which uses this technology to actuate single bioparticles.

8 APPENDIX

8.1 Appendix A: Quartz Process

Start with 4 inch quartz wafers:

[ICL]

1. RCA clean
2. lpcvd 2μm polysilicon deposition

   Tube6b

   2 successive 1μm depositions (100 minutes each)

[TRL]

3. HMDS
4. Spin resist

   Standard OCG 825 resist

   500rpm 9s

   750rpm 6s

   2500rpm 30s

5. Prebake 30 min 90°C
6. EV1 expose 2.3 sec
7. Develop in OCG934 1:1

   30-40 sec

8. Postbake 30min 120°C
9. STS1 etch MIT37 1min

[ICL]

10. AME5000 oxide etch recipe: 'Nagle chf3 only'

    5-10 10min etches

    15 minutes rest time between etches

    Do each wafer in one block of machine time

[TRL]

11. acid hood- piranha clean 10min
12. STS1 SF6_14 etch 1 min
13. HMDS

14. Spin resist

    AZ5214E IR resist

    500rpm 9s

    750rpm 6s

    2500rpm 30s

15. Prebake 30min
16. KS2 expose 20s
17. Convection oven 105°C

    25 min, in boat

18. Flood exposure 100sec, KS2
19. Develop AZ422 90sec

[Gold contaminated from step 19 forward]

20. Evaporate 100A Titanium, 1000A platinum on top of resist

    E-beam in TRL

21. Lift off using acetone, photowet-R
22. Anneal 1 hour at 600°C TRL tube B1
23. Dice into chipsusing diesaw

8.2 Appendix B: Silicon Process

Start with 4 inch silicon double side polished (DSP) wafers:

Front:

[ICL]

24. RCA Clean
25. Grow 1μm thermal oxide

    TubeA3

    recipe#224

    (1000degree (C),

        Dry O2 10min

        Wet H20 2h20min

[TRL]

26. HMDS
27. Resist coat

    standard resist OCG825

    500rpm 6s

    750rpm 6s

    2500rpm 30s

28. Prebake 30min
29. Pattern oxide using mask 1 (large well)

    EV1 2.3 sec

30. Develop 30-40s (OCG 934 1:1)
31. Postbake 30 min
32. Wet oxide etch (1 μm)

    Acidhood- BOE

    10 min

33. Piranha clean 10 min- acidhood
34. HMDS
35. Resist coat

    Thick resist AZP4620

1750rpm till coated

3500rpm 60s

5000rpm 10s

36. Prebake 45-60min
37. Pattern resist using mask 2 (small well)

    EV1 15sec

38. Develop 90s (AZ440)
39. STS1 etch silicon (small well)

    120μm etch

    Recipe: MIT37

40. Piranha clean
41. STS1 etch silicon (large well)

    20μm etch

    Recipe: MIT37

42. Strip oxide

    BOE

    10min

Back:

[TRL]

43. HMDS
44. Resist coat

    thick resist(AZP4620) 10μm

    1750rpm till coated

    1000rpm 60s

    5000rpm 10s

45. Prebake 60 min
46. Expose using mask 3 (large well)

    EV1 20-22 sec

47. Develop 2.5min (AZ440)
48. Postbake 90°C 5 min

49. Attach wafer to quartz handle wafer

    Use photoresist and jig

50. Postbake 90°C 25 min

51. STS etch large well through wafer to intersect 20μm into small channel

    Recipe: MIT37

52. Separate wafer from handle wafer in acetone

    Soak overnight

53. Dice using diesaw

8.3 Appendix C: Device Assembly Process

[EML]

1. Hotplate 90C 30min quartz chips
2. Spin cytop on quartz chips

   2000 rpm 30sec
3. Hotplate bake 90C 30min
4. Align silicon chips to quartz wafer

   Use jig
5. Hotplate 160C 2 hours with weights (10Kg)
6. Cool 2 hours on plate with weights

8.4 Appendix D: MATLAB Code for Finite Difference Model- Line Heater

```
clear all
close all

% Define geometry and properties

k=10.4;      %conduction coefficient, W/K-m
Q=0.25;   %Total power, W
L=200e-6; %length of resistor, m
L2=40e-6; %length in y-direction, m
L1=115e-6; %length in x-direction, m
w=10e-6;    %width of resistor, m
A=L*w;    %heated area, m^2
To=290;      %Ambient temperature, K
deltax=5e-6;   %x element size, m
deltay=5e-6;   %y element size, m
Qv=Q/(A*1000e-10);   %Volumetric power, W/m^3



% Use finite element method.
N=216;       %assign number of nodes
G=zeros(N); %start to build the G matrix
G(1,1)=-1.5;
G(1,2)=.5;
G(1,24)=0.5;

for i=2:1:23;
    G(i,i-1)=.5;
    G(i,i)=-3;
    G(i,i+1)=.5;
    G(i,i+24)=1;
 end

G(24,23)=.5;
G(24,24)=-2;
G(24,48)=0.5;

G(25,1)=0.5;
G(25,25)=-2;
G(25,26)=1;
G(25,49)=0.5;

for i=26:1:47;
    G(i,i-24)=1;
    G(i,i-1)=1;
    G(i,i)=-4;
    G(i,i+1)=1;
    G(i,i+24)=1;
 end

for i=48:24:168;
    G(i,i-24)=0.5;
    G(i,i-1)=1;
    G(i,i)=-3;
```

```
    G(i,i+24)=.5;
    G(i+1,i-23)=0.5;
    G(i+1,i+1)=-2;
    G(i+1,i+2)=1;
    G(i+1,i+25)=0.5;
 end

    i=192;
    G(i,i-24)=0.5;
    G(i,i-1)=1;
    G(i,i)=-3;
    G(i,i+24)=0.5;
    G(i+1,i-23)=0.5;
    G(i+1,i+1)=-1.5;
    G(i+1,i+2)=.5;



for i=50:1:71;
    G(i,i-24)=1;
    G(i,i-1)=1;
    G(i,i)=-4;
    G(i,i+1)=1;
    G(i,i+24)=1;
 end

 for i=74:1:95;
    G(i,i-24)=1;
    G(i,i-1)=1;
    G(i,i)=-4;
    G(i,i+1)=1;
    G(i,i+24)=1;
 end

 for i=98:1:119
    G(i,i-24)=1;
    G(i,i-1)=1;
    G(i,i)=-4;
    G(i,i+1)=1;
    G(i,i+24)=1;
 end

 for i=122:1:143;
    G(i,i-24)=1;
    G(i,i-1)=1;
    G(i,i)=-4;
    G(i,i+1)=1;
    G(i,i+24)=1;
 end

 for i=146:1:167;
    G(i,i-24)=1;
    G(i,i-1)=1;
    G(i,i)=-4;
    G(i,i+1)=1;
    G(i,i+24)=1;
 end
```

```
 for i=170:1:191;
    G(i,i-24)=1;
    G(i,i-1)=1;
    G(i,i)=-4;
    G(i,i+1)=1;
    G(i,i+24)=1;
 end

 for i=194:1:215;
    G(i,i-1)=.5;
    G(i,i)=-3;
    G(i,i+1)=.5;
    G(i,i-24)=1;
 end

G(216,192)=0.5;
G(216,215)=.5;
G(216,216)=-2;

P=zeros(N,1);
P(1,1)=-0.5*To*k;
for i=2:1:23;
    P(i,1)=-1*To*k;
end
P(24,1)=-1*To*k;

P(193,1)=-0.5*To*k;
for i=194:1:215;
    P(i,1)=-1*To*k;
end
P(216,1)=-1*To*k;

for i=48:24:192;
    P(i,1)=-1*To*k;
 end

 P(73,1)=P(73,1)-0.25*deltax*deltay*Qv;
 P(121,1)=P(121,1)-0.25*deltax*deltay*Qv;

P(93,1)=P(93,1)-0.25*deltax*deltay*Qv;
P(141,1)=P(141,1)-0.25*deltax*deltay*Qv;


P(97,1)=P(97,1)-0.5*deltax*deltay*Qv;
P(117,1)=P(117,1)-0.5*deltax*deltay*Qv;


for i=74:1:92;
   P(i,1)=P(i,1)-0.5*deltax*deltay*Qv;
   end

 for i=122:1:140;
   P(i,1)=P(i,1)-0.5*deltax*deltay*Qv;
end
```

```
for i=98:1:116;
   P(i,1)=P(i,1)-deltax*deltay*Qv;
end



%Calculation
%T=inv(G)*P*(1/k);
T=G\P*(1/k);

for y=1:1:9;
   for x=1:1:24;
      Z(y,x)=T(x+24*(y-1));
   end
end

x=[0:(L1/23):L1];
y=[0:(L2/8):L2];
%x=[L1:(L1/14):0];
%y=[L2:(L2/26):0];
mesh(x,y,Z);

sum=0;
for i=97:1:117
    sum=sum+T(i);
end

Tav=sum/21;
Tcenter=T(97)
Tmidpoint=T(107)
Tedge=T(117)

centerdiff=(Tcenter-Tav)/Tav
midpointdiff=(Tmidpoint-Tav)/Tav
edgediff=(Tedge-Tav)/Tav
```

8.5 Appendix E: MATLAB Code for Finite Difference Model- Folded Heater

```
clear all
close all

% Define geometry and properties

k=10.4;        %conduction coefficient, W/K-m
Q=0.25;    %Total power, W
L=650e-6; %length of resistor, m
L2=130e-6; %length in y-direction, m
L1=70e-6; %length in x-direction, m
w=10e-6;     %width of resistor, m
A=L*w;    %heated area, m^2
To=290;        %Ambient temperature, K
deltax=5e-6;   %x element size, m
deltay=5e-6;   %y element size, m
Qv=Q/(A*1000e-10);   %Volumetric power, W/m^3



% Use finite element method.
N=405;        %assign number of nodes
G=zeros(N); %start to build the G matrix
G(1,1)=-1.5;
G(1,2)=.5;
G(1,16)=0.5;

for i=2:1:14;
    G(i,i-1)=.5;
    G(i,i)=-3;
    G(i,i+1)=.5;
    G(i,i+15)=1;
 end

G(15,14)=.5;
G(15,15)=-2;
G(15,30)=0.5;

G(16,1)=0.5;
G(16,16)=-2;
G(16,17)=1;
G(16,31)=0.5;

for i=17:1:29;
    G(i,i-15)=1;
    G(i,i-1)=1;
    G(i,i)=-4;
    G(i,i+1)=1;
    G(i,i+15)=1;
 end

for i=30:15:375;
    G(i,i-15)=0.5;
    G(i,i-1)=1;
    G(i,i)=-3;
```

```
    G(i,i+15)=.5;
    G(i+1,i-14)=0.5;
    G(i+1,i+1)=-2;
    G(i+1,i+2)=1;
    G(i+1,i+16)=0.5;
 end

    i=390;
    G(i,i-15)=0.5;
    G(i,i-1)=1;
    G(i,i)=-3;
    G(i,i+15)=0.5;
    G(i+1,i-14)=0.5;
    G(i+1,i+1)=-1.5;
    G(i+1,i+2)=.5;



for i=32:1:44;
    G(i,i-15)=1;
    G(i,i-1)=1;
    G(i,i)=-4;
    G(i,i+1)=1;
    G(i,i+15)=1;
 end

 for i=47:1:59;
    G(i,i-15)=1;
    G(i,i-1)=1;
    G(i,i)=-4;
    G(i,i+1)=1;
    G(i,i+15)=1;
 end

 for i=62:1:74
    G(i,i-15)=1;
    G(i,i-1)=1;
    G(i,i)=-4;
    G(i,i+1)=1;
    G(i,i+15)=1;
 end

 for i=77:1:89;
    G(i,i-15)=1;
    G(i,i-1)=1;
    G(i,i)=-4;
    G(i,i+1)=1;
    G(i,i+15)=1;
 end

 for i=92:1:104;
    G(i,i-15)=1;
    G(i,i-1)=1;
    G(i,i)=-4;
    G(i,i+1)=1;
    G(i,i+15)=1;
 end
```

```
for i=107:1:119;
   G(i,i-15)=1;
   G(i,i-1)=1;
   G(i,i)=-4;
   G(i,i+1)=1;
   G(i,i+15)=1;
end

for i=122:1:134;
   G(i,i-15)=1;
   G(i,i-1)=1;
   G(i,i)=-4;
   G(i,i+1)=1;
   G(i,i+15)=1;
end

for i=137:1:149;
   G(i,i-15)=1;
   G(i,i-1)=1;
   G(i,i)=-4;
   G(i,i+1)=1;
   G(i,i+15)=1;
end

for i=152:1:164;
   G(i,i-15)=1;
   G(i,i-1)=1;
   G(i,i)=-4;
   G(i,i+1)=1;
   G(i,i+15)=1;
end

for i=167:1:179;
   G(i,i-15)=1;
   G(i,i-1)=1;
   G(i,i)=-4;
   G(i,i+1)=1;
   G(i,i+15)=1;
end

for i=182:1:194;
   G(i,i-15)=1;
   G(i,i-1)=1;
   G(i,i)=-4;
   G(i,i+1)=1;
   G(i,i+15)=1;
end

for i=197:1:209;
   G(i,i-15)=1;
   G(i,i-1)=1;
   G(i,i)=-4;
   G(i,i+1)=1;
   G(i,i+15)=1;
end
```

```
for i=212:1:224;
   G(i,i-15)=1;
   G(i,i-1)=1;
   G(i,i)=-4;
   G(i,i+1)=1;
   G(i,i+15)=1;
end

for i=227:1:239;
   G(i,i-15)=1;
   G(i,i-1)=1;
   G(i,i)=-4;
   G(i,i+1)=1;
   G(i,i+15)=1;
end

for i=242:1:254;
   G(i,i-15)=1;
   G(i,i-1)=1;
   G(i,i)=-4;
   G(i,i+1)=1;
   G(i,i+15)=1;
end

for i=257:1:269;
   G(i,i-15)=1;
   G(i,i-1)=1;
   G(i,i)=-4;
   G(i,i+1)=1;
   G(i,i+15)=1;
end

for i=272:1:284;
   G(i,i-15)=1;
   G(i,i-1)=1;
   G(i,i)=-4;
   G(i,i+1)=1;
   G(i,i+15)=1;
end

for i=287:1:299;
   G(i,i-15)=1;
   G(i,i-1)=1;
   G(i,i)=-4;
   G(i,i+1)=1;
   G(i,i+15)=1;
end

for i=302:1:314;
   G(i,i-15)=1;
   G(i,i-1)=1;
   G(i,i)=-4;
   G(i,i+1)=1;
   G(i,i+15)=1;
end

for i=317:1:329;
```

```
    G(i,i-15)=1;
    G(i,i-1)=1;
    G(i,i)=-4;
    G(i,i+1)=1;
    G(i,i+15)=1;
 end

 for i=332:1:344;
    G(i,i-15)=1;
    G(i,i-1)=1;
    G(i,i)=-4;
    G(i,i+1)=1;
    G(i,i+15)=1;
 end

 for i=347:1:359;
    G(i,i-15)=1;
    G(i,i-1)=1;
    G(i,i)=-4;
    G(i,i+1)=1;
    G(i,i+15)=1;
 end

 for i=362:1:374;
    G(i,i-15)=1;
    G(i,i-1)=1;
    G(i,i)=-4;
    G(i,i+1)=1;
    G(i,i+15)=1;
 end

 for i=377:1:389;
    G(i,i-15)=1;
    G(i,i-1)=1;
    G(i,i)=-4;
    G(i,i+1)=1;
    G(i,i+15)=1;
 end

 for i=392:1:404;
    G(i,i-1)=.5;
    G(i,i)=-3;
    G(i,i+1)=.5;
    G(i,i-15)=1;
 end

G(405,390)=0.5;
G(405,404)=.5;
G(405,405)=-2;

P=zeros(N,1);
P(1,1)=-0.5*To*k;
for i=2:1:14;
    P(i,1)=-1*To*k;
end
P(15,1)=-1*To*k;
```

```
P(391,1)=-0.5*To*k;
for i=392:1:404;
    P(i,1)=-1*To*k;
end
P(405,1)=-1*To*k;

for i=30:15:390;
    P(i,1)=-1*To*k;
 end

 P(316,1)=P(316,1)-0.25*deltax*deltay*Qv;
 P(346,1)=P(346,1)-0.25*deltax*deltay*Qv;
P(47,1)=P(47,1)-0.25*deltax*deltay*Qv;
P(349,1)=P(349,1)-0.25*deltax*deltay*Qv;
P(351,1)=P(351,1)-0.25*deltax*deltay*Qv;
P(53,1)=P(53,1)-0.25*deltax*deltay*Qv;
P(357,1)=P(357,1)-0.25*deltax*deltay*Qv;
P(55,1)=P(55,1)-0.25*deltax*deltay*Qv;
P(57,1)=P(57,1)-0.25*deltax*deltay*Qv;
P(331,1)=P(331,1)-0.5*deltax*deltay*Qv;
P(347,1)=P(347,1)-0.5*deltax*deltay*Qv;
P(348,1)=P(348,1)-0.5*deltax*deltay*Qv;
P(80,1)=P(80,1)-0.5*deltax*deltay*Qv;
P(352,1)=P(352,1)-0.5*deltax*deltay*Qv;
P(324,1)=P(324,1)-0.5*deltax*deltay*Qv;
P(56,1)=P(56,1)-0.5*deltax*deltay*Qv;

for i=62:15:302;
   P(i,1)=P(i,1)-0.5*deltax*deltay*Qv;
   end

 for i=94:15:334;
   P(i,1)=P(i,1)-0.5*deltax*deltay*Qv;
end

for i=96:15:336;
   P(i,1)=P(i,1)-0.5*deltax*deltay*Qv;
end

for i=68:15:308;
   P(i,1)=P(i,1)-0.5*deltax*deltay*Qv;
end

for i=353:1:356;
   P(i,1)=P(i,1)-0.5*deltax*deltay*Qv;
end

for i=70:15:310;
   P(i,1)=P(i,1)-0.5*deltax*deltay*Qv;
end

for i=72:15:342;
   P(i,1)=P(i,1)-0.5*deltax*deltay*Qv;
end

for i=48:1:52;
   P(i,1)=P(i,1)-0.5*deltax*deltay*Qv;
```

```
   end

P(332,1)=P(332,1)-deltax*deltay*Qv;

for i=63:15:333;
   P(i,1)=P(i,1)-deltax*deltay*Qv;
end

for i=64:1:66;
   P(i,1)=P(i,1)-deltax*deltay*Qv;
end

for i=67:15:337;
   P(i,1)=P(i,1)-deltax*deltay*Qv;
end

for i=338:1:340;
   P(i,1)=P(i,1)-deltax*deltay*Qv;
end

for i=71:15:341;
   P(i,1)=P(i,1)-deltax*deltay*Qv;
end

P(79,1)=P(79,1)-0.75*deltax*deltay*Qv;

P(317,1)=P(317,1)-0.75*deltax*deltay*Qv;

P(81,1)=P(81,1)-0.75*deltax*deltay*Qv;

P(323,1)=P(323,1)-0.75*deltax*deltay*Qv;

P(325,1)=P(325,1)-0.75*deltax*deltay*Qv;



%Calculation
%T=inv(G)*P*(1/k);
T=G\P*(1/k);

for y=1:1:27;
   for x=1:1:15;
      Z(y,x)=T(x+15*(y-1));
   end
end

x=[0:(L1/14):L1];
y=[0:(L2/26):L2];
%x=[L1:(L1/14):0];
%y=[L2:(L2/26):0];
mesh(x,y,Z);

sum=0;
for i=62:15:333
    sum=sum+T(i);
end
sum=sum+T(332)+T(331);
```

```
for i=67:15:337
    sum=sum+T(i);
end

for i=71:15:341
    sum=sum+T(i);
end

for i=63:1:66
    sum=sum+T(i);
end


for i=338:1:340
    sum=sum+T(i);
end

Tav=sum/65;
Tcenter=T(198);
Ttop=T(331);
Tbottom=T(65);
Tedge=T(206);

centerdiff=(Tcenter-Tav)/Tav;
topdiff=(Ttop-Tav)/Tav;
bottomdiff=(Tbottom-Tav)/Tav;
edgediff=(Tedge-Tav)/Tav;
```

9 BIBLIOGRAPHY

1. Voldman, J., M.L. Gray, and M.A. Schmidt, *Microfabrication in Biology and Medicine.* Annual Review of Biomedical Engineering, 1999. **1**: p. 401-425.
2. Voldman, J., et al., *A Microfabrication-Based Dynamic Array Cytometer.* Analytical Chemistry, 2002. **74**: p. 3984-3990.
3. Shoji, S. and M. Esashi, *Microflow Devices and Systems.* Journal of Micromechanics and Microengineering, 1994. **4**: p. 157-171.
4. Ho, C.-M. and Y.-C. Tai, *Micro-Electro-Mechanical-Systems (MEMS) and Fluid Flows.* Annual Review of Fluid Mechanics, 1998. **30**: p. 579-612.
5. Gravesen, P., J. Branebjerg, and O.S. Jensen, *Microfluidics- A Review.* Journal of Micromechanics and Microengineering, 1993. **3**: p. 168-182.
6. Elwenspoek, M., et al., *Towards Integrated Microliquid Handling Systems.* Journal of Micromechancs and Microengineering, 1994. **4**: p. 227-245.
7. Grosjean, C. and Y.-C. Tai. *A Thermopneumatic Peristaltic Micropump.* in *Transducers.* 1999.
8. Zengerle, R., et al. *Performance Simulation of Microminiaturized Membrane Pumps.* in *Transducers '93.* 1993.
9. Zengerle, R., et al., *A Bidirectional Silicon Micropump.* Sensors and Actuators A, 1995. **A50**: p. 81-86.
10. Koch, M., et al., *A Novel Micromachined Pump Based on Thick-Film Piezoelectric Actuation.* Sensors and Actuators A, 1998. **70**: p. 98-103.
11. Jerman, H. *Electrically-Activated, Micromachined Diaphragm Valves.* in *IEEE Solid State Sensor and Actuator Workshop.* 1990.
12. Miller, R.A., et al. *Electromagnetic MEMS Scanning Mirrors for Holographic Data Storage.* in *Solid State Sensor and Actuator Workshop.* 1996.
13. Yanagisawa, K., H. Kuwano, and A. Tago. *An Electromagnetically Driven Microvalve.* in *Transducers '93.* 1993.
14. Liu, R.H., Q. Yu, and D.J. Beebe, *Fabrication and Characterization of Hydrogel-Based Microvalves.* Journal of Microelectromechanical Systems, 2002. **11**(1): p. 45-53.
15. Huang, D. and E.S. Kim, *Micromachined Accoustic-Wave Liquid Ejector.* Journal of Microelectromechanical Systems, 2001. **10**(3): p. 442-449.
16. Manz, A., et al., *Electroosmotic Pumping and Electrophoretic Separations for Miniaturized Chemical Analysis Systems.* Journal of Micromechanics and Microengineering, 1994. **4**.
17. Stanczyk, T., et al., *A Microfabricated Electrochemical Actuator for Large Displacements.* Journal of Microelectromechanical Systems, 2000. **9**(3): p. 314-320.
18. Geng, X., et al., *Bubble-Based Micropump for Electrically Conducting Liquids.* Journal of Micromechanics and Microengineering, 2001. **11**: p. 270-276.
19. Tsai, J.H. and L. Lin. *Nozzle-Diffuser Based Micro Bubble Pump.* in *Solid-State Sensor and Actuator Workshop- Late News.* 2000. Hilton Head, S.C.
20. Choi, B.K., et al. *Electrolytic and Thermal Bubble Generation Using AC Inductive Powering.* in *Transducers '99, Proceedings of the 10th International Conference on Solid-State Sensors and Actuators.* 1999. Sendai, Japan.

21. Donald, D.K., *Thermal Optical Switches for Light*. 1998, Hewlett Packard Company: US Patent 5,732,168.
22. Evans, J., D. Liepmann, and A.P. Pisano. *Planar Laminar Mixer*. in *MEMS '97*. 1997.
23. Evans, J.D. and D. Liepmann. *The Bubble Spring and Channel (BSAC) Valve: An Actuated, Bistable Mechanical Valve for In-Plane Fluid Control*. in *Transducers '99, Proceedings of the 10th International Conference on Solid-State Sensors and Actuators*. 1999. Sendai, Japan.
24. Lin, L., A. Pisano, and A. Lee. *Microbubble Powered Actuator*. in *Transducers '91*. 1991.
25. Lin, L., *Microscale Thermal Bubble Formation: Thermophysical Phenomena and Applications*. Microscale thermophysical Engineering, 1998. **2**: p. 71-85.
26. Tsai, J.-H. and L. Lin, *Transient Thermal Bubble Formation on Polysilicon Micro-Resistors*. Journal of Heat Transfer, 2002. **124**: p. 375-382.
27. Beatty, C.C. *A Chronology of Thermal Ink-Jet Strucures*. in *Solid-State Sensor and Actuator Workshop*. 1996. Hilton Head, S.C.
28. Asai, A., *Application of the Nucleation Theory to the Design of Bubble Jet Printers*. Japanese Journal of Applied Physics, 1989. **28**: p. 909-915.
29. Allen, R.R., J.D. Meyer, and W.R. Knight, *Thermodynamics and Hydrodynamics of Thermal Ink Jets*. Hewlett-Packard Journal, 1985. **36**: p. 21-27.
30. Nielsen, N.J., *History of Thinkjet Printhead Development*. Hewlett-Packard Journal, 1985. **36**: p. 4-10.
31. Okamoto, T., T. Suzuki, and N. Yamamoto, *Microarray Fabrication with Covalent Attachment of DNA Using Bubble Jet Technology*. Nature Biotechnology, 2000. **18**: p. 438-441.
32. Tseng, F.-G., C.-J. Kim, and C.-M. Ho, *A High-Resolution High-Frequency Monolithic Top-Shooting Microinjector Free of Satellite Drops- Part I: Concept, Design, and Model*. Journal of Microelectromechanical Systems, 2002. **11**(5): p. 427-436.
33. Tseng, F.-G., C.-J. Kim, and C.-M. Ho, *A High-Resolution High-Frequency Monolithic Top-Shooting Microinjector Free of Satellite Drops- Part II: Fabrication, Implementation, and Characterization*. Journal of Microelectromechanical Systems, 2002. **11**(5): p. 437-447.
34. Papavasiliou, A.P., D. Liepmann, and A.P. Pisano. *Electrolysis-Bubble Actuated Gate Valve*. in *Solid-State Sensor and Actuator Workshop*. 2000. Hilton Head, S.C.
35. Tsai, J.-H. and L. Lin, *Active Microfluidic Mixer and Gas Bubble Filter Driven by Thermal Bubble Micropump*. Sensors and Actuators A, 2002. **97-98**: p. 665-671.
36. Lin, L. and A. Pisano, *Bubble Forming on a Micro Line Heater*, in *ASME Microechanical Sensors, Actuators, and Systems*, D. Cho, et al., Editors. 1991. p. 147-163.
37. Martin, J.C. and D.E. Swartzendruber, *Time: A New Parameter for Kinetic Measurements in Flow Cytometry*. Science, 1980. **207**: p. 199-201.
38. Kamentsky, L.A. and M.R. Melamed, *Spectrophotometric Cell Sorter*. Science, 1967. **156**: p. 1364-1365.

39. Darzynkiewicz, Z., et al., *Laser-Scanning Cytometry: A New Instrumentation with Many Applications.* Experimental Cell Research, 1999. **249**: p. 1-12.
40. Beebe, D.J., G.A. Mensing, and G.M. Walker, *Physics and Applications of Microfluidics in Biology.* Annual Review of Biomedical Engineering, 2002. **4**: p. 261-286.
41. Jakeway, S.C., A.J. de Mello, and E.L. Russell, *Miniaturized Total Analysis Systems for Biological Analysis.* Fresenius Journal of Analytical Chemistry, 2000. **366**: p. 525-539.
42. Liu, C.-C. and Z. Jin, *Applications of Microfabrication and Micromachining Techniques to Biotechnology.* Trends in Biotechnology, 1997. **15**: p. 213-216.
43. Fu, A.Y., et al., *A Microfabricated Fluorescence-Activated Cell Sorter.* Nature Biotechnology, 1999. **17**: p. 1109-1111.
44. Kruger, J., et al., *Development of a Microfluidic Device for Fluorescence Activated Cell Sorting.* Journal of Micromechanics and Microengineering, 2002. **12**: p. 486-494.
45. Gawad, S., L. Schild, and P. Renaud, *Micromachined Impedance Spectroscopy Flow Cytometer for Cell Analysis and Particle Sizing.* Lab on a Chip, 2001. **1**: p. 76-82.
46. Sato, K., et al., *Individual and Mass Operation of Biological Cells using Micromechanical Silicon Devices.* Sensors and Actuators, 1990. **A21-A23**: p. 948-953.
47. Deutsch, M. and A. Weinreb, *Apparatus for High-Precision Sequential Optical Measurement of Living Cells.* Cytometry, 1994. **16**: p. 214-226.
48. Bousse, L., et al. *Silicon Micromachining in the Fabrication of biosensors Using Living Cells.* in *IEEE Solid-State Sensor and Actuator Workshop.* 1990. Hilton head, SC.
49. Bousse, L., et al., *Micromachined Multichannel Systems for the Measurement of Cellular Metabolism.* Sensors and Actuators B, 1994. **20**: p. 145-150.
50. Bousse, L. and W. Parce, *Applying Silicon Micromachining to Cellular Metabolism.* IEEE Engineering in Medicine and Biology, 1994. **13**(3): p. 396-401.
51. Bousse, L., *Whole Cell Biosensors.* Sensors and Actuators B, 1996. **34**: p. 270-275.
52. Yang, M., C.-W. Li, and J. Yang, *Cell Docking and On-Chip Monitoring of Cellular Reactions with a Controlled Concentration Gradient on a Microfluidic Device.* Analytical Chemistry, 2002. **74**: p. 3991-4001.
53. Pethig, R. *Application of A.C. Electrical Fields to the Manipulation and Characterisation of Cells.* in *Automation in Biotechnology.* 1990: Elsevier Science Publishers.
54. Pethig, R., *Dielectrohoresis: Using Inhomogeneous AC Electrical Fields to Separate and Manipulate Cells.* Critical Reviews in Biotechnology, 1996. **16**(4): p. 331-348.
55. Fuhr, G., et al., *Dielectrophoretic Field Cages: Technique for Cell, Virus and Macromolecule Handling.* Cell. Eng. inc. Molecular Eng., 1995. **1**: p. 47-57.
56. Fuhr, G. and S. Shirley, *Biological Applications of Microstructures*, in *Topics in Current Chemistry.* 1998, Springer Verlag: Berlin Heidelberg. p. 83-116.

57. Voldman, J., et al. *A Dielectrophoresis-Based Array Cytometer*. in *Transducers '01*. 2001. Munich, Germany.
58. Voldman, J., et al., *Holding Forces of Single-Particle Dielectrophoretic Traps.* Biophysical Journal, 2001. **80**(1): p. 531-541.
59. Tong, L.S. and Y.S. Tang, *Boiling Heat Transfer and Two-Phase Flow*. second edition ed. 1997, Washington, D.C.: Taylor and Francis.
60. Cole, R. and S. Van Stralen, *Boiling Phenomena*. Vol. 1. 1979: Hemisphere Publishing Corporation.
61. Mikic, B.B. and W.M. Rohsenow, *Bubble Growth Rates in Non-Uniform Temperature Field*, in *Progress in Heat and Mass Transfer*. 1969, Pergamon Press. p. 283-293.
62. Mills, A.F., *Heat and Mass Transfer*. 1995: Irwin.
63. Duffy, D.C., et al., *Rapid Prototyping of Microfluidic Switches in Poly(dimethyl siloxane) and their Actuation by Electro-osmotic Flow.* Journal of Micromechanics and Microengineering, 1999. **9**: p. 211-217.
64. Braff, R.A., *Microbubble Cell Actuator*, in *Mechanical Engineering*. 1999, Masachusetts Institute of Technology: Cambridge, MA.
65. Matsumoto, Y., K. Yoshida, and M. Ishida, *A Novel Deposition Technique for Fluorocarbon Films and its Applications for Bulk- and Surface-Micromachined Devices.* Sensors and Actuators A, 1998. **66**: p. 308-314.
66. Lu, H., M.A. Schmidt, and K.F. Jensen, *Photochemical Reactions and On-Line UV Detection in Microfabricated Reactors.* Lab on a Chip, 2001. **1**: p. 22-28.
67. Losey, M., *Novel Multiphase Chemical Reaction Systems Enabled by Microfabrication Technology*, in *Chemical Engineering Department*. 2001, MIT: Cambridge, MA.
68. Monahan, J., A.A. Gewirth, and R.G. Nuzzo, *A Method for Filling Complex Polymeric Microfluidic Devices and Arrays.* Analytical Chemistry, 2001. **73**: p. 3193-3197.
69. Takahashi, K., J.-G. Weng, and C.-L. Tien, *Marangoni Effect in Microbubble Systems.* Microscale Thermophysical Engineering, 1999. **3**: p. 169-182.
70. Cole, R., *Boiling Nucleation*, in *Advances in Heat Transfer*, J.P. Hartnett and T.F. Irvine, Editors. 1974, Academic Press.